

INVESTIGATING THE IMPACT OF MANMADE RESERVOIRS ON LARGE-SCALE
HYDROLOGY AND WATER RESOURCES USING HIGH-RESOLUTION MODELING

By

Sanghoon Shin

A DISSERTATION

Submitted to
Michigan State University
in partial fulfillment of the requirements
for the degree of

Civil Engineering – Doctor of Philosophy

2019

ABSTRACT

INVESTIGATING THE IMPACT OF MANMADE RESERVOIRS ON LARGE-SCALE HYDROLOGY AND WATER RESOURCES USING HIGH-RESOLUTION MODELING

By

Sanghoon Shin

Manmade reservoirs are important components of the terrestrial hydrologic system. Dam installments fragment river systems, and reservoir operations alter flow regimes. The total storage capacity of existing global reservoirs is large enough to hold one sixth of annual continental discharge to global oceans. Due to growing energy demands, hundreds of large dams are being built and planned around the world, especially in the developing countries. Therefore, there is an urgent need to develop a better understanding of the impact of the existing and new dams on hydrological, ecological, agricultural, and socio-economic systems. Owing to increasing computational power and needs to understand and simulate processes in small-scale, hydrological models are advancing towards hyper-resolution global hydrological models. One of benefits of the increased spatial resolution is that the dynamics of surface water inundation over natural river-floodplain systems and manmade reservoirs can be explicitly represented; however, existing global models are not capable of simulating the river-floodplain-reservoir inundation dynamics in an integrated manner. This dissertation addresses this important standing issue by developing a high-resolution, continental-scale model to simulate the spatial and temporal dynamics of reservoir storage and release, thus paving pathways toward hyper-resolution surface water modeling in continental- to global-scale hydrological and climate models. The newly developed model is applied to simulate reservoirs within the contiguous United States (CONUS) and the Mekong River Basin (MRB) in Southeast Asia. With respect to the model development, the following advances are made over the previous global reservoir modeling studies: (1) an

existing algorithm for reservoir operation is improved by conducting analytical analysis and numerical experiments and by introducing new calibration features for reservoir operation; (2) the spatial extent and its seasonal dynamics of reservoirs are explicitly simulated and reservoirs are treated as an integral part of river-floodplain routing, thus reservoir storage is no longer isolated from river and floodplain storages; and (3) a novel approach for processing and integrating high-resolution digital elevation models (DEMs) in river-floodplain-reservoir routing is introduced. The newly developed reservoir scheme is integrated within the river-floodplain routing scheme of a continental hydrological model, LEAF-Hydro-Flood, which is set for the CONUS, where abundant data are available for model validation. Then, the reservoir scheme is integrated into a global hydrodynamics model, CaMa-Flood, to investigate the historical impact of manmade reservoirs in the MRB that is experiencing an unprecedented boom in hydropower dam construction. Using the new scheme, the role of flood dynamics in modulating the hydrology of the MRB and the potential impact of flow regulation by the dams on the inundation dynamics are investigated. The significance of hydrologic effect of increasing dams is compared with that of climate variability. The fully coupled river-reservoir-floodplain storage simulation approach presented in this dissertation provides an advancement in hydrological modeling in terms of the representation of surface water dynamics, which is indispensable for better attribution of the observed changes in the water cycle, prediction of changes in water resources, and the understanding of the continually changing environmental and ecological systems.

ACKNOWLEDGEMENTS

I would like to express my gratitude to my advisor, Dr. Yadu Pokhrel, for guiding me to think big and critically, identify and focus on important issues, and properly organize and present the research results. I also thank to the committees, Drs. Shu-Guang Li, Mantha Phanikumar, and Lifeng Luo, for giving me many great and helpful advices.

My parents have sacrificed their lives and have always prayed for me; I will never be able to pay back to them. Jiyeong is the best supporter in my life; She is always happier than me for my accomplishments, and she gives me courage me when I am discouraged. I also thank to my brothers and sister who share many valuable memories with me.

I send many thanks to lab mates, Farshid, Suyog, Mateo, and Tamanna, who helped each other and discussed about various topics. I also thank to Eunsang for helping me settle in East Lansing.

This study was supported by NASA (Award#: 80NSSC17K0259), National Science Foundation (Award#: 1752729), and WaterCUBE project from Michigan State University (Award#: GR100096). Simulations were conducted using Cheyenne (doi:10.5065/D6RX99HX) provided by NCAR's Computational and Information Systems Laboratory, sponsored by the National Science Foundation.

Lastly, I dedicate this thesis to the Lord, who is always bigger than I thought.

TABLE OF CONTENTS

LIST OF TABLES	vii
LIST OF FIGURES	viii
Chapter 1. Introduction.....	1
1.1. Research Motivation.....	1
1.1.1. Manmade Reservoirs in Global Hydrology	1
1.1.2. High-resolution Modeling of Reservoir Dynamics at the Continental Scale	3
1.1.3. Application of a New High-resolution Reservoir Scheme: Mekong River Basin ..	7
1.2. Research Goal, Objectives, and Questions.....	9
1.3. Dissertation Outline.....	11
Chapter 2. High-resolution Modeling of Storage Dynamics at the Continental Scale.....	12
2.1. Introduction	12
2.2. Materials and Methods	13
2.2.1. The Hydrological Model LEAF-Hydro-Flood-Dam (LHFD)	13
2.2.2. Data and Preprocessing.....	20
2.3. Results and Discussion.....	34
2.4. Summary and Conclusion	39
Chapter 3. Development of an Improved Reservoir Operation Scheme	41
3.1. Introduction	41
3.2. Improvements on Reservoir Operation Scheme.....	42
3.2.1. The Improved Reservoir Operation Scheme.....	42
3.2.2. Analytical Comparison with the Existing Reservoir Operation Schemes	44
3.2.3. The Calibration of R	49
3.3. Experimental Settings.....	51
3.4. Results and Discussion.....	53
3.4.1. LHFD Model Validation for the CONUS.....	53
3.4.2. Improvements in Reservoir Release and Storage	55
3.4.3. The Role of R in Release and Storage Simulations	61
3.4.4. Stability of Reservoir Simulation over the CONUS	63
3.4.5. Flow Regime Change due to Reservoirs.....	65
3.5. Summary and Conclusion	68
Chapter 4. Sensitivity Analysis for the Effect of Upstream Flow Regulation on Flood Dynamics in the Lower Mekong River Basin and Tonle Sap Lake.....	70
4.1. Introduction	70
4.2. Materials and Methods	72
4.2.1. HiGW-MAT.....	72
4.2.2. CaMa-Flood	72
4.2.3. Simulation Settings	73
4.2.4. Terrestrial Water Storage (TWS) and its Estimation.....	76
4.2.5. Data... ..	78

4.3. Results and Discussion	79
4.3.1. Model Evaluation.....	79
4.3.2. Role of River-Floodplain Storage on TWS dynamics and Historical Variability	86
4.3.3. Potential Effects of Flow Regulation on Flood Dynamics in the LMRB	90
4.4. Summary and Conclusion	111
Chapter 5. Impact of Manmade Reservoirs on Mekong River Basin Hydrology over the Past Years.....	112
5.1. Introduction	112
5.2. Materials and Methods	115
5.2.1. CaMa-Flood and HiGW-MAT models	115
5.2.2. Dams and Reservoirs database.....	116
5.2.3. Observed Data for Model Validation.....	119
5.2.4. Incorporation of Reservoirs into CaMa-Flood.....	120
5.2.5. Reservoir Operation Scheme	123
5.2.6. Simulation Settings	128
5.3. Results and Discussion.....	130
5.3.1. River Discharge and Water Level.....	130
5.3.2. Flood Occurrence.....	136
5.3.3. Flooded Area and Surface Water Storage.....	143
5.4. Results and Discussion.....	150
Chapter 6. Summary and Conclusion	152
REFERENCES	154

LIST OF TABLES

Table 3-1 Summary of experimental settings	51
Table 3-2 The attributes of reservoirs selected for calibration (Source: GRanD database)	52
Table 3-3 Summary of performance measures for different simulations.....	57
Table 4-1 Geographic location of stations in MRB.....	74
Table 4-2 Comparison of flooded areas with Arias et al. (2012) for the major flood regions around Tonle Sap Lake indicated by thick black line in Figure 4-4a.....	85
Table 4-3 Changes in major flood characteristics (e.g., onset, magnitude, duration, and amount) compared to the baseline simulation at different stations analyzed in Figure 4-8.....	94
Table 4-4 A summary of the results of potential changes in flooded area around Tonle Sap Lake under different flow regulation scenarios from this study and those from Arias, Piman, et al. (2014).....	102
Table 4-5 Same as Table 4-3 but for dry year (1998).	109
Table 4-6 Same as Table 4-3 but for wet year (2000).	110
Table 5-1 Observation stations of the Mekong River Commission	120
Table 5-2 Simulation settings.....	129

LIST OF FIGURES

Figure 2-1 An example of the storage simulation problem by storage buffer effect (SBE) for Lake Mead.	19
Figure 2-2 Reservoirs locations and an example of imported surface extent.....	22
Figure 2-3 Comparison of drainage area at dam locations based on GRanD database and LHF model (a) before and (b) after the application of coordinates correction.....	23
Figure 2-4 Temporal disaggregation of USGS water use data to monthly time scale for Butte county in California.....	25
Figure 2-5 River and reservoir elevation parameterizations.....	27
Figure 2-6 Longitudinal bed profiles of Colorado river derived from 90 m HydroSHEDS void-filled (green), HydroSHEDS conditioned (blue), and MERIT (red) DEMs.	30
Figure 2-7 Simulated river-reservoir-floodplain storages averaged over 1985-2010 period	36
Figure 2-8 Same as in Figure 2-7 but for additional regions	38
Figure 3-1 Demonstration of the need to use $R = \min(1, \alpha c)$	47
Figure 3-2 Model validation for annual mean flow over the contiguous US.....	53
Figure 3-3 Validation of seasonal river discharge at the major gauging stations over the contiguous US (unit: $10^3 \text{ m}^3/\text{s}$).	54
Figure 3-4 Evaluation of simulated release and storage for the six selected reservoirs in the Columbia, Colorado, San Joaquin, Sacramento, and Missouri river basins.	56
Figure 3-5 Same as in Figure 3-4 but for additional reservoirs.....	58
Figure 3-6 Boxplot showing stability of simulated reservoir storages for 1,889 GRanD reservoirs estimated from frequency analysis for the occurrence of (a) overfilling and (b) underfilling.	65
Figure 3-7 Effect of reservoir operation on long-term average daily river discharge with the exceedance probability of (a) 90% (low flow; Q_{90}), (b) 50% (median flow; Q_{50}), and (c) 10% (high flow; Q_{10}), shown as relative change between Q_{DAM} (i.e., R_{cal}) and Q_{NAT} (i.e., NAT simulation).	67
Figure 4-1 Long-term (1981-2010) mean river discharge (m^3/s) simulated by CaMa-Flood at 10km spatial resolution over the entire Mekong River Basin (MRB).	80

Figure 4-2 Evaluation of simulated river discharge with observations obtained from the Mekong River Commission (MRC) at locations indicated by red circles in Figure 4-1.....	81
Figure 4-3 Simulated annual mean flood depth downscaled to 500m spatial resolution using high resolution SRTM topography data for (a) average year (mean of 1981-2010), (b) dry year (1998), and wet year (2000).....	82
Figure 4-4 Monthly flood occurrence and daily water surface elevation.	83
Figure 4-5 Role of river-floodplain storage on TWS dynamics over the MRB.....	87
Figure 4-6 Same as in Figure 4-5 but only for the Lower Mekong region.	88
Figure 4-7 Relationship between river-floodplain storage from CaMa-Flood (monthly) and climate variability (annual mean precipitation and temperature) over the Lower Mekong domain.....	89
Figure 4-8 Daily river discharge at Pakse (PA) station (location shown in Figure 4-1 and Table 4-1) simulated by HiGW-MAT model with and without considering the existing dams.	90
Figure 4-9 Potential changes in daily river discharge by flow regulation.	92
Figure 4-10 Same as in Figure 4-9 but for simulated water level.....	97
Figure 4-11 Flood occurrence and the effects of flow regulation on it.....	99
Figure 4-12 Flooded areas having different flood occurrence estimated from the baseline simulation results presented in Figure 4-11 and their changes under different flow regulation scenarios	101
Figure 4-13 Same as in Figure 4-11 but for dry (1998) and wet (2000) years.	105
Figure 4-14 Simulated flood occurrence in dry and wet years for different flow regulation scenarios.....	106
Figure 4-15 Same as in Figure 4-9 but for 1998 (dry year).....	107
Figure 4-16 Same as in Figure 4-9 but for 2000 (wet year).....	108
Figure 5-1 The spatial distribution of river discharge and commissioned dams (as of 2016) over the MRB.	118
Figure 5-2 Deviation at 3-arcsec grids from dam crest level to water level to achieve recorded storage capacity for (a) the MERIT and (b) HydroSHEDS DEMs.	121
Figure 5-3 Relationship between dam height in the database and adjusted dam height at 3-arcmin CaMa-Flood modeling grids based on the MERIT DEM.....	123

Figure 5-4 The profile of Lam Ta Khong P.S. dam.	126
Figure 5-5 Comparison of turbine design flow and 20% (Q_{20}), 30% (Q_{30}), and 40% (Q_{40}) stream flow exceedances for 12 reservoirs.....	126
Figure 5-6 Mean discharge and stream flow exceedances for 86 reservoirs.	127
Figure 5-7 Validation of simulated river discharge.	132
Figure 5-8 Validation of simulated water level.	133
Figure 5-9 Potential changes in river discharge by the existing 86 dams estimated from the ALL simulations.....	134
Figure 5-10 Potential changes in water level by the existing 86 dams estimated from the ALL simulations.....	135
Figure 5-11 Simulated flood occurrence in 3-arcsec (90 m) over the MRB.	137
Figure 5-12 Spatial validation of simulated inundation dynamics with 0.00100° resolution GSW flood occurrence data.	138
Figure 5-13 Spatial validation of simulated inundation dynamics with 0.00025° resolution GSW flood occurrence data.	139
Figure 5-14 Spatial validation of simulated inundation dynamics with the Sentinel-1 product.....	141
Figure 5-15 Historical flooded area and surface water storage dynamics over the MRB.	144
Figure 5-16 Historical flooded area and surface water storage dynamics over the MRB for 1979-2016.	145
Figure 5-17 The monthly GSW flooded area for 1984-2016.	146
Figure 5-18 The potential impacts of existing 86 dams on surface water dynamics estimated from the ALL simulations for selected periods and years.	148
Figure 5-19 The potential impacts of existing 86 dams on surface water dynamics estimated from the ALL simulations for the entire simulation period.	149

Chapter 1. Introduction

1.1. Research Motivation

1.1.1. Manmade Reservoirs in Global Hydrology

Water impoundment in reservoirs and flow regulation by dams have exerted a profound influence on the terrestrial water cycle (Lehner et al., 2011b). The total impoundment capacity of over 50,000 large and thousands of additional small dams built globally during the last century (Chao et al., 2008; Vörösmarty et al., 2003) has been estimated to be in between 7,000-10,000 km³ (Chao et al., 2008; Graf, 1999; Lehner et al., 2011b; Lehner & Döll, 2004; McCully, 2001; Renwick et al., 2005; Wisser et al., 2010), which represents about one-sixth of the annual continental discharge to global oceans (T. Oki & Kanae, 2006). There are growing evidences that the large dams have fragmented river systems globally (Dynesius & Nilsson, 1994; Graf, 1999; Nilsson et al., 2005; Postel et al., 1996) by changing the magnitude, timing, and duration of flows (Haddeland et al., 2006; Hanasaki et al., 2006; Y. Pokhrel, Hanasaki, Koirala, et al., 2012; Veldkamp et al., 2017; Zajac et al., 2017) and altering natural flow regimes (Poff et al., 1997). Studies have shown that the adverse effects of dams extend far beyond physical alteration of rivers and changes in downstream hydrology because the hydrologic alterations can have severe ecological and environmental consequences. Many dams have threatened the ecological integrity of terrestrial and river-floodplain ecosystems (Bunn & Arthington, 2002; Vörösmarty et al., 2010) by altering seasonal flood pulse (Arias, Cochrane, et al., 2014), impeding species movement (Stone, 2016), causing river channel incision (Ligon et al., 1995) and delta erosion (S. L. Yang et al., 2011), blocking sediment flux (Gupta et al., 2012; Syvitski et al., 2005; Vörösmarty et al., 1997; Wisser et al., 2010; Xue et al., 2011), and altering the transport of dissolved nutrients (Eiriksdottir et al., 2017).

Evidences suggest that some global mega deltas are sinking at an alarming rate owing to the reduction in sediment delivery by large dams (Bohannon, 2010; Schmidt, 2015; Syvitski et al., 2009), which has increased the vulnerability of coastal communities to flooding under climate change (Alex Smajgl et al., 2015). Large reservoirs also affect the terrestrial carbon cycle by changing nitrate removal (Shuai et al., 2017), carbon gases ebullition (Tušer et al., 2017), and greenhouse gas emissions, especially methane in tropical reservoirs (Fearnside & Pueyo, 2012; Kemenes et al., 2007). In the highly regulated river basins, reservoirs alter terrestrial water storage dynamics and storage in terminal lakes (Chaudhari et al., 2018; Felfelani et al., 2017; Y. Pokhrel et al., 2017; T. Zhou et al., 2016) and also affect groundwater systems (Zhao et al., 2012), which can have important implications on global sea level change (Chao et al., 2008; Y. Pokhrel, Hanasaki, Yeh, et al., 2012; Wada, Reager, et al., 2016). Further, surface energy budget is also impacted by reservoirs through water temperature cooling effect (Buccola et al., 2016), thermal stratification (S. Wang et al., 2012), and increase in evaporation from open water surfaces which has been linked to intensified extreme precipitation through regional climate feedback (Degu et al., 2011; Hossain, 2010; Hossain et al., 2010, 2012; Woldemichael et al., 2012)

The growing recognition and consensus about the impairment of river ecosystems by dams (Babbitt, 2002) has resulted in an increase in dam removal in the US and other regions with aging dams (Doyle et al., 2005; Null et al., 2014; Pohl, 2002). At the same time, there is an ongoing proliferation in large-scale dam construction to fulfill growing energy needs in the developing world; dozens of large dams are being built and hundreds of others are planned in the Amazon and Mekong River basins among other regions (Grumbine & Xu, 2011; Y. Pokhrel et al., 2018; Sabo et al., 2017; Stone, 2016; Timpe & Kaplan, 2017; Winemiller et al., 2016; Zarfl

et al., 2015). Therefore, there is an urgent need to develop a better understanding of the hydrological and ecological impacts of the existing as well as the planned dams. It is even more critical to understand how the impacts of large dams will interfere with the impacts of climate change, especially in regions that are likely to be heavily impacted by climate change such as the southwestern US (Cook et al., 2015; Rajagopalan et al., 2009), and the Amazon (Y. Pokhrel et al., 2014) and Mekong (Lauri et al., 2012) river basins. As discussed above, historical observations for pre- and post-dam periods can be used to examine the hydrological, geomorphic, and ecological changes caused by dams where such data exist (e.g., Räsänen et al., 2017; Timpe & Kaplan, 2017); however, the observed data alone is not sufficient to isolate the changes caused by natural climate variability and human activities. Models are indispensable tools that can be used for such isolation of natural and human-induced changes (Y. Pokhrel et al., 2017) as well as for future projections. Hence, continued efforts are indispensable to advance hydrological models for better attribution of the observed changes in the water cycle, prediction of changes in water resources, and understanding of Earth environmental system.

1.1.2. High-resolution Modeling of Reservoir Dynamics at the Continental Scale

Modeling reservoirs involves determination of storage and release by using the information on inflow, storage capacity, and downstream demands. Owing to the difficulty in representing individual operation rules in large-scale models, studies have used generic operation schemes to simulate reservoir operation within continental and global scale hydrological models. Early works simulated reservoir releases by using a rectangular weir equation or retarding flow velocity (Coe, 2000; Döll et al., 2003; Meigh et al., 1999). Pioneering works on grid-based, explicit simulation of reservoirs in global models were presented by Hanasaki et al. (2006) and Haddeland et al. (2006). A number of subsequent studies have improved and incorporated these

schemes into various other global hydrological models (GHMs) and land surface models (LSMs) (e.g., Adam et al., 2007; van Beek et al., 2011; Biemans et al., 2011; Pokhrel et al., 2015; Pokhrel, Hanasaki, Koirala, et al., 2012; Voisin et al., 2013; Wada et al., 2014), and other studies have modified them for reservoir-specific applications by including operation rules for the individual reservoirs (Mateo et al., 2014; Zhao et al., 2016). There are also more recent studies that have used slightly different approaches. For example, Solander et al. (2016) developed a generalized reservoir model by employing temperature as a primary factor to modulate seasonal changes in reservoir management, and Ehsani et al. (2016) developed a general reservoir operation scheme (GROS) using artificial neural networks.

The aforementioned studies have made great strides in simulating the effects of dams on river discharge over large global basins; however, significant standing issues still remain in terms of better simulating the spatio-temporal dynamics of reservoir storage and release and making the schemes compatible with hyper-resolution hydrological models (Benedict et al., 2017; Beven et al., 2015; Bierkens, 2015; Bierkens et al., 2015; McCabe et al., 2017; Wood et al., 2011). Here four issues are identified related to reservoir schemes to be used in hyper-resolution hydrological models. There are more issues related to reservoir modeling, but these are of primary interest of this study. **First**, most schemes have been developed for macro-scale hydrological models with a typical grid size of 50-100 km, in which the storage capacities of one or more reservoirs located within a grid cell are lumped into a single storage component. Such lumped treatment of multiple reservoirs poses a major challenge in incorporating the existing schemes in future models with an improved treatment of hydrological states and fluxes at relatively high spatial and temporal resolutions (Clark et al., 2017; Fatichi et al., 2016). **Second**, the existing schemes do not explicitly represent reservoir surface extent dynamics that is a critically important process to

simulate reservoir evaporation under climate change using coupled atmospheric-hydrological models and examine the potential climate impacts of large reservoirs such as those suggested by Degu et al. (2011).

Third, the existing reservoir schemes are not designed for an integrated simulation of river, reservoirs, and floodplain which is essential when applying the models in regions such as the Amazon, Mekong, and Mississippi river basins (e.g., Allison et al., 2012; Gran et al., 2009; Grumbine & Xu, 2011; Kesel et al., 1974; Timpe & Kaplan, 2017) where river-floodplain-reservoir dynamics needs to be simulated as a coupled process. Significant advancements are therefore necessary to make existing reservoir schemes suitable for examining the impacts of dam regulation on the seasonally inundated floodplains, wetlands, and other flood pulse-dependent ecosystems in the upstream and downstream of reservoirs. **Forth**, it is essential to employ an improved treatment of topography data, especially to better represent river and reservoir bed elevations consistent with the proposed hyper-resolution models (D. Yamazaki et al., 2017). The direct use of digital elevation models (DEMs)—assuming that they represent bear-earth elevations—is reasonable for modeling natural rivers and reservoirs that are built after the production of DEMs or will be built in the future (e.g., Gernaat et al., 2017). For existing reservoirs, however, the DEMs provide water surface elevation which can be tens to hundreds of meters above reservoir bed; the direct use of DEMs can thus cause numerical instability or yield unrealistic results (see Chapter 2.2.2).

The issues enumerated above have not yet been addressed even in recent studies. For example, Solander et al. (2016) intended to develop a generalized reservoir operation scheme for possible integration into global LSMs for long-term climate impact simulations, but they devised

the model with minimal complexity and without considering high resolution spatial and temporal dynamics of reservoir extent and release. Ehsani et al. (2016) developed a reservoir model which was designed to simulate flow regulation by multiple reservoirs in a basin, but the scheme aggregates reservoirs capacities into a large hypothetical reservoir, and hence does not explicitly simulate the spatial extent. Some recent enhancements in large-scale models employ relatively high-resolution grids (1-10 km) with reservoir modules (Voisin et al., 2017; Wada, de Graaf, et al., 2016), but the spatial representation of reservoirs in these studies is identical to that in the global models, i.e., the reservoir storage is either aggregated into a single model grid where a dam is located or in a predefined reservoir area that is composed of multiple model grid cells (i.e., level-pool). Further, concerted community efforts have been made to develop the national water model (NWM, <http://water.noaa.gov/about/nwm>), which provides a platform for a detailed and high-resolution hydrological simulations including lakes and reservoirs; however, the issues identified above have not yet been resolved in the reservoir scheme of NWM. As of summer 2019, the NWM uses Muskingum-Cunge method for river water routing, level-pool method to represent reservoir storage, and storage-proportional release equation for reservoir release (i.e., passive reservoirs; weir-like operation).

Therefore, advancements are needed to make reservoir schemes commensurate with an increase in spatial resolution. Answering the questions related to the impacts of reservoirs on the terrestrial water cycle (e.g., how does the seasonally inundated floodplains, wetlands, and other flood pulse-dependent ecosystems change by manmade reservoirs?) is possible only through the use of such advanced models that explicitly simulate reservoir dynamics over large scales. In addition, considering the increased use of reservoir operation schemes in continental to global scale studies on both historical analysis (e.g., Pokhrel et al., 2017; Voisin et al., 2017) and future

predictions (e.g., Hejazi et al., 2015; Yamagata et al., 2018), the continued improvement of reservoir schemes—both by adding new capabilities and improving the existing operation/release schemes—becomes even more important.

1.1.3. Application of a New High-resolution Reservoir Scheme: Mekong River Basin

The Mekong River is one of the few large and complex global river systems that still remain mostly undammed (Grumbine & Xu, 2011), but the rapid socio-economic growth, increasing regional energy demands, and geopolitical opportunities have led to a recent rise in basin-wide construction of large hydropower dams (Y. Pokhrel et al., 2018; Winemiller et al., 2016). In the Lancang River, which drains the upper portion of the Mekong River Basin (MRB), China is building dozens of mega dams (Y. Pokhrel et al., 2018); in the Lower Mekong River Basin (LMRB), some large main stem dams are being built and about a dozen main stem and over hundred tributary dams are planned (Grumbine & Xu, 2011; Y. Pokhrel et al., 2018; Stone, 2016). The new dams and reservoirs are expected to fulfill the rapidly growing energy needs and provide other societal benefits; however, the positive benefits come with unprecedented negative social-environmental consequences (Sabo et al., 2017; Schmitt et al., 2018; Stone, 2016).

In the MRB, of particular concern are the effects of flow regulation on the seasonal hydrological regime characterized by a strong unimodal flow pattern, known as the flood pulse (Junk et al., 1989). The monsoon-driven flood pulse delivers a timely supply of water and nutrient-rich sediments for flood-recession agriculture, inland fisheries, and extensive instream and wetland ecosystems, thus serving as a driving force for life and major ecosystems in the LMRB (Arias et al., 2013; Kummu & Sarkkula, 2008). The flood pulse is also the primary driver of the unique flow reversal in the Tonle Sap River (TSR) that discharges water and sediments

from the Mekong River into Tonle Sap Lake (TSL) during wet season and drains water from the lake into the Mekong during dry season. The seasonal river-lake inundation dynamics around TSL supports one of the world's largest and most productive freshwater fishery (Baran & Myschowoda, 2009; Bonheur & Lane, 2002; Mekong River Commission, 2005) and provides dry-season flow for critical ecosystems and agriculture in the Mekong Delta (Frappart et al., 2006). Any alterations in the duration, amplitude, timing, and rapidity of the Mekong flood pulse and the resulting changes in floodplain dynamics in the LMRB can thus severely impact a wide range of ecosystems and undermine regional food security (Kummu & Sarkkula, 2008).

An understanding of the surface hydrology of the MRB, LMRB, and TSL has been improved by the studies (1) based on observations for identifying the historical changes in hydrology of MRB (Arias et al., 2013; Inomata & Fukami, 2008), (2) based on large-scale modeling and scenario analysis for analyzing and predicting overall hydrology of MRB (Costa-Cabral et al., 2008; Mekong River Commission, 2010; Xue et al., 2011), and (3) based on hydrodynamic modeling for understanding flood inundations in TSL (Arias et al., 2012; Arias, Piman, et al., 2014; Kummu & Sarkkula, 2008). While such many pieces of knowledge have been accrued, an integrated view that puts all the pieces in place to provide a holistic view for the entire MRB has not been yet presented. To address this gap, this study applies the newly developed high-resolution reservoir scheme in large-scale hydrological model over the entire MRB. The new modeling framework is indispensable for MRB—where the flow is characterized by a highly pronounced seasonal dynamics and unprecedented boom in the construction hydropower dams is underway—since reservoirs are to be modeled as an integral part of river-floodplain system.

1.2. Research Goal, Objectives, and Questions

The aforementioned importance of understanding the role of manmade reservoirs in global hydrology (Chapter 1.1.1) and the need for improving high-resolution reservoir scheme in large-scale models (Chapter 1.1.2) lead me to pursue the **overarching goal** to improve our understanding of the compounded impacts of manmade reservoirs and climate change on river flow and flood inundation dynamics by advancing our capability to better represent reservoirs in high-resolution large-scale models. The newly developed modeling tool is expected to be useful for the broader hydrological modeling community toward addressing the increasing issues related to the sustainability of food, energy, and water systems under changing Earth environments. Toward achieving this goal, this dissertation is driven by the following specific science questions, which are categorized into two parts.

Part 1. Development of a reservoir scheme for high-resolution global hydrological model:

- Q1. What are the technical challenges and opportunities in better representing river-reservoir-floodplain storage at high-resolution in continental and global scales?
- Q2. How can we better simulate reservoir release in large-scale models using the limitedly available information (e.g., lack of reservoir-specific rule curves)?

Part 2. Investigation of the impacts of dams on land hydrology and water resources in the MRB:

- Q3. What are the implications of potential flow regulation by new dams on downstream flood inundation dynamics?
- Q4. What role does the flood dynamics play in modulating the overall hydrology of the basin?
- Q5. How have the flood dynamics and surface water storage in the MRB changed over the past four decades?

- Q6. Are the effects of dams significant compared to that of climate variability?
- Q7. What will be the role of existing reservoirs in modulating surface water storage and inundation dynamics over the MRB in the future?

The specific **objectives** are (1) to develop a high-resolution reservoir scheme that presents the dynamics of reservoir storage as an integral part of river-floodplain routing to be used in Global Hydrological Models (GHMs), Land Surface Models (LSMs), and Earth System Models (ESMs) and (2) to investigate the impact of proliferating dams on land hydrology and water resources under climate change. The new reservoir scheme is firstly developed and validated for the Contiguous United States (CONUS) where abundant observation data is available. Then, the new model is applied to the Mekong River Basin (MRB) where the flow is characterized by a highly pronounced seasonal dynamics and unprecedented hydropower dam construction boom is underway. While the model is applied to the MRB in the present study, the new scheme can be seamlessly incorporated using global datasets into any high-resolution river-floodplain routing schemes in GHMs and ESMs and applied over other regions or globally.

1.3. Dissertation Outline

The abovementioned research questions are tackled in individual chapters (from Chapter 2 through Chapter 6). The following provides a brief summary of the remaining chapters.

Chapter 2. High-resolution Modeling of Storage Dynamics at the Continental Scale
: Technical challenges and solutions in representing river-reservoir-floodplain storage at high-resolution are presented.

Chapter 3. Development of an Improved Reservoir Operation Scheme
: A new reservoir operation scheme is developed. Problems of the existing reservoir operation schemes are elucidated, the parameterizations in the existing schemes are improved, and a calibration feature is newly introduced.

Chapter 4. Sensitivity Analysis for the Effect of Upstream Flow Regulation on Flood Dynamics in the Lower Mekong River Basin and Tonle Sap Lake
: As a surrogate of potential flow regulations by future dams, scenarios are set up by gradually changing timing (i.e., 1-month early and delayed peak) and magnitude (up to 50% reduction) of flood peak from the upper Mekong river. For those scenarios, the changes in patterns of river flow and inundation in the lower Mekong river basin (LMRB) and Tonle Sap Lake (TSL) are examined.

Chapter 5. Impact of Manmade Reservoirs on Mekong River Basin Hydrology
: Historical flood dynamics over the entire Mekong river basin (MRB) is simulated using the models with and without reservoirs. The historical impacts of reservoirs on the flood dynamics of the MRB are investigated for various aspects (e.g., discharge, water depth, inundation extent, and surface water storage). In addition, the definite future impact of reservoirs is estimated.

Chapter 6. Summary and Conclusion

Chapter 2. High-resolution Modeling of Storage Dynamics at the Continental Scale

2.1. Introduction

A new high-resolution reservoir scheme is developed that addresses the four issues of reservoir modeling identified in Chapter 1.1.2. The new reservoir scheme is incorporated within a river-floodplain routing scheme in a continental scale hydrological model LEAF-Hydro-Flood (Miguez-Macho & Fan, 2012a) (hereafter LHF), resulting in LEAF-Hydro-Flood-Dam (LHFD). The following advances over the previous reservoir schemes are made: (1) the spatial extent and its seasonal dynamics of reservoirs are explicitly simulated, and reservoirs are treated as an integrated part of river-floodplain routing, thus reservoir storage is no longer isolated from river and floodplain storages, and (2) a novel approach for processing and integrating high-resolution DEMs in river-floodplain-reservoir routing is introduced. LHFD model is tested over the contiguous United States (CONUS) at 5 km grids using the abundant data of river flow, reservoir storage, and water use. It is noteworthy that new scheme and data processing algorithm can be seamlessly incorporated into any high-resolution river-floodplain routing models and applied over other regions or globally.

The remainder of the chapter is organized as follows. The LHFD model, approach for pre-processing of DEM, river-reservoir-floodplain routing, and the calibration method are described in Chapter 2.2. Results of high-resolution river-reservoir-floodplain storages are provided in Chapter 2.3. Summary and concluding remarks are presented in Chapter 2.4.

2.2. Materials and Methods

2.2.1. The Hydrological Model LEAF-Hydro-Flood-Dam (LHFD)

LEAF-Hydro-Flood (LHF) is a continental-scale land hydrology model that resolves various hydrological processes in the realm from canopy to groundwater aquifers on a physical basis (e.g., radiative energy transfer, turbulent exchange, heat conduction, snow covering and snow water melting, evapotranspiration, throughfall, runoff, river-floodplain flow, infiltration, soil moisture and heat diffusion, lateral groundwater flow, etc.). The energy and water storages are simulated largely for four entities, i.e., (1) canopy air and vegetation, (2) bare soil surface, (3) 14 soil layers, and (4) river-floodplain. The energy and water fluxes between the interfaces of these entities are also simulated.

In this study, LHF is further developed by incorporating a new reservoir operation scheme to form LEAF-Hydro-Flood-Dam (LHFD). LHF has been continuously developed since its original version of the Land Ecosystem-Atmosphere Feedback (LEAF) model (Walko et al., 2000), which is a land surface scheme of the Regional Atmosphere Modeling System (RAMS). The original LEAF was extensively improved and enhanced to develop LEAF-Hydro for North America (Fan et al., 2007; Miguez-Macho et al., 2007) by allowing (1) the water table to rise and fall or the vadose zone to shrink or grow, (2) the water table, recharged by soil drainage, to relax through discharge into rivers, and lateral groundwater flow, leading to convergence to low valleys, (3) two-way exchange between groundwater and rivers, representing both losing and gaining streams, (4) river routing to the ocean as kinematic waves, and (5) setting sea level as groundwater head boundary condition. LEAF-Hydro was further enhanced to develop LEAF-Hydro-Flood (LHF) (Miguez-Macho & Fan, 2012a) by introducing a river-floodplain routing scheme that solves the full momentum equation of open channel flow, taking into account the

backwater effect (the diffusion term) (D. Yamazaki et al., 2011) and the inertia of large water mass of deep flow (acceleration term) (Bates et al., 2010). LHF was applied over the Amazon river basin using 2 km grids with 4-minute time step for land hydrology and 30-second for surface water routing, where it was extensively validated against observed water table, river discharge, and flooding (Miguez-Macho & Fan, 2012a), soil moisture and evapotranspiration (Miguez-Macho & Fan, 2012b), and terrestrial water storage (TWS) change (Y. Pokhrel et al., 2013) using satellite data from Gravity Recovery and Climate Experiment (GRACE), and used for future projections (Y. Pokhrel et al., 2014).

The objective of Chapter 2 is on advancing the river-reservoir routing scheme. Hence, in the remainder of Chapter 2.2.1, a description for the existing river-reservoir routing scheme of LHF is provided, and an approach to implement reservoirs into LHF to develop LHFD is presented.

2.2.1.1. Existing Surface Water Routing Scheme in LHF

The 1-D continuity equation is given as:

$$\frac{\partial Q}{\partial x} + \frac{\partial A}{\partial t} = q \quad (2-7)$$

where, Q is discharge, A is flow cross section, and q is lateral flow.

The 1-D momentum equation is given as:

$$\frac{\partial v}{\partial t} + v \frac{\partial v}{\partial x} + g \left(\frac{\partial(d+z)}{\partial x} + S_f \right) = 0 \quad (2-8)$$

where, v is mean flow velocity, g is gravitational acceleration, d is flow depth, and z is bed elevation. Here, $\frac{\partial v}{\partial t}$ represents the local inertia (or acceleration), $v \frac{\partial v}{\partial x}$ represents the advective inertia, $\frac{\partial(d+z)}{\partial x}$ represents water (pressure and potential) slope, and S_f represents friction slope. The friction slope S_f is calculated by Manning as:

$$S_f = \frac{n^2 v^2}{R^{4/3}} \quad (2-9)$$

where, R is hydraulic radius.

By combining equations (2-8) and (2-9) and assuming R is equal to d , the following finite difference equation is obtained.

$$\frac{v_i^{t+\Delta t} - v_i^t}{\Delta t} + v_i^{t+\Delta t} \frac{v_{i+1}^t - v_i^t}{\Delta x} + g \frac{h_{i+1}^{t+\Delta t} - h_i^{t+\Delta t}}{\Delta x} + \frac{gn^2 v_i^t}{(d_i^{t+\Delta t})^{4/3}} v_i^{t+\Delta t} = 0 \quad (2-10)$$

where, h is water surface elevation. Water depth and level at the time step $(t+\Delta t)$ can be obtained according to mass balance using the flow velocity at t . Then, equation (2-10) can be implicitly solved.

$$v_i^{t+\Delta t} = \frac{\frac{v_i^t}{\Delta t} + g \frac{h_i^{t+\Delta t} - h_{i+1}^{t+\Delta t}}{\Delta x}}{\frac{1}{\Delta t} + \frac{v_{i+1}^t - v_i^t}{\Delta x} + \frac{gn^2 v_i^t}{(d_i^{t+\Delta t})^{4/3}}} \quad (2-11)$$

To enhance numerical stability, a second-order Runge-Kutta method is employed. Sea water level is used as a boundary condition at the ends of rivers.

Strictly speaking, the assumption of $R=d$ for Equation (2-9) is valid only if the river width (b) is sufficiently greater than water depth (d). If such assumption is relaxed, $d_i^{t+\Delta t}$ in Equations (2-10) and (2-11) should be substituted to R (i.e., cross section area divided by wetted perimeter; $R = bd_i^{t+\Delta t} / (b + 2d_i^{t+\Delta t})$ in case of rectangular channel that LHFD model employs). In case of LHFD, more than 95% grid cells have 10 times greater channel width than mean water depth. The other grid cells (less than 5%) even have small river discharge, hence the effects of the assumption of $R=d$ is not considerable.

2.2.1.2. Spatial Resolution of Routing Grids

Computational cost increases as the finer spatial resolution of modeling is used owing to (1) the increase of routing reaches and (2) the increase of temporal resolution to ensure numerical stability. The number of routing reaches is proportional to the number of grid cells; hence it increases quadratically with the grid cell size. The maximum temporal resolution, Δt_{\max} , is limited to satisfy the Courant-Friedrichs-Lew (CFL) condition for the numerical stability.

$$\Delta t_{\max} = \alpha \frac{\Delta x}{\sqrt{gh_t}} \quad (2-12)$$

where, Δx is the flow distance of flow routing reach, α is a coefficient to enhance stability, h_t is the flow depth at time step t . α varies according to the numerical scheme. $\alpha=1$ (i.e., Courant number is unity) and $\alpha>1$ (i.e., Courant number larger than 1) for explicit schemes and implicit scheme, respectively. CFL condition is a necessary, yet not sufficient, condition for convergence, hence the modeling time step is usually set smaller than Δt_{\max} or, equivalently, $\alpha<1$ is used to calculate Δt_{\max} .

Considering the balance between the spatial resolution and available computational resources, the LHFD model is developed at 5-km resolution. For 1-year simulation, it takes 358 core-hours (2.3-GHz Intel Xeon E5-2697V4 processors; NCAR Cheyenne). In total, ~60,000 core-hours are consumed for 6 sets of 28-year simulations, which is equivalent to 10 days when 252 cores are used. In the setting of 5-km resolution, the default 1-year simulation outputs for daily hydrological states and fluxes require ~119 GB (i.e., $40 \text{ variables} \times 1450 \text{ columns} \times 1510 \text{ rows} \times 4 \text{ bytes/cell} \times 2^{-30} \text{ GB/byte} \times 365 \text{ days}$) of storage space. For a single set of 28-year simulation, the output files require 3.25 TB; here we have 6 sets of simulations (see Chapter 3 for details), hence the total size of output files is 19.5 TB.

Various spatial resolutions are set in other large-scale studies with consideration of computational cost as well. For example, 25-km (15-arcmin) resolution is used for global scale (D. Yamazaki et al., 2011) and 10-km (5- or 6-arcmin) for regional scale studies (Mateo et al., 2014; D. Yamazaki et al., 2014). Predecessors of LHFD model also have been set up in various spatial resolutions. The 5-km routing grids are finer than those of LEAF-Hydro for North America (Fan et al., 2007; Miguez-Macho et al., 2007), which is originally developed to have 12.5 km of river water routing grids while the other land surface modules are set for 1.25 km resolution. LEAF-Hydro-Flood for South America (Miguez-Macho & Fan, 2012a, 2012b; Y. Pokhrel et al., 2013) has 1.5-arcmin (2-km) resolution with 1.83-times bigger domain size (i.e., 1780×2250). The use of finer grid cell for LHFD model is possible, but it will require more computational resources and storage space.

2.2.1.3. A Challenge in Incorporating Reservoirs— Storage Buffer Effect (SBE)

To allow water impoundment behind a dam and prevent flooded water brimming over neighboring basins, two constraints are added: (1) river discharge at the dam location is controlled by the reservoir operation rule, and (2) the downstream of a reservoir is hydraulically disconnected from the reservoir except for the one-way reservoir release. When the river-reservoir-floodplain elevations are accurately parameterized, solving the full momentum equation with the two constraints enables water impoundment within the reservoir and backwater flow to the upstream; however, we find these constraints to be insufficient because the appropriateness of simulated reservoir storage is highly dependent on the accuracy of DEMs.

Specifically, we find that excessively accumulated water storages on non-reservoir upstream cells in the vicinity of reservoirs can cause critical problems in simulating the dynamics of reservoir storage by ‘buffering’ (or dampening) the change in reservoir storage. We refer this buffering contribution of non-reservoir upstream storages to reservoir storage dynamics as the storage buffering effect (SBE). SBE does not cause water balance problem, but reservoir storage can be inappropriately simulated when SBE is excessive; the excessive non-reservoir upstream storages can significantly dampen the change in water level (or storage) within the reservoir. An example of erroneously simulated reservoir storage is provided below.

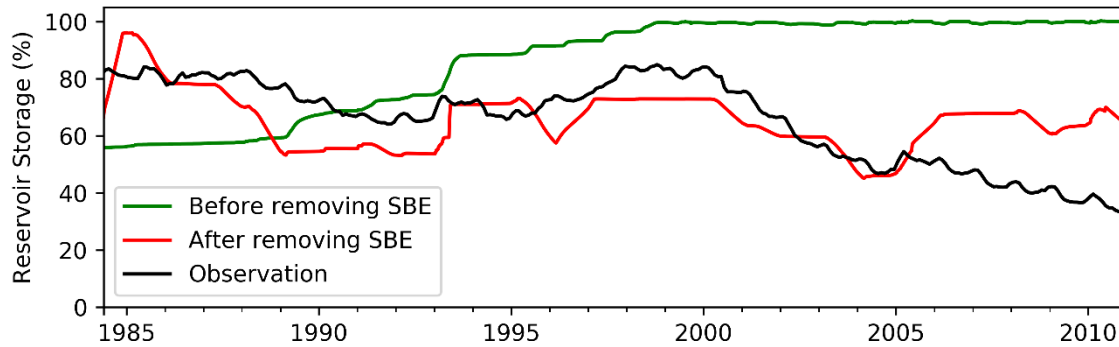


Figure 2-1 An example of the storage simulation problem by storage buffer effect (SBE) for Lake Mead. When SBE is properly removed (red line), the storage fluctuates over time. When SBE is unremoved (green), the reservoir storage increases slowly and monotonously, and the seasonal fluctuation of release reduces significantly after the reservoir is fully filled. The simulation setting of the case where SBE is removed (red line) is identical to H06 in Chapter 3.2.1. The simulation setting of the case where SBE is unremoved (green line) is identical to H06 in Chapter 3.2.1 except for the initial condition obtained from additional 30-years of spin-up.

Figure 2-1 shows an example for Lake Mead in the Colorado river for which reservoir storage is erroneously simulated when SBE is not eliminated. The simulation setting of Figure 2-1 is identical to H06 (see Chapter 3.2.1 for details) except for the initial condition obtained from additional 30-years of spin-up. Since water continues to back up to large upstream non-reservoir cells, it takes ~8 years to increase the storage by ~17% (i.e., from 55% to 72% of storage during 1983-1991 period), which is a very slow filling rate compared to the 2.6 year hydraulic residence time of Lake Mead (Holdren & Turner, 2010). Further, although the non-reservoir upstream storages are hydraulically connected to main reservoir storage, it is not considered in determining the release. Consequently, the release is persistently underestimated, and the reservoir storage can slowly increase near to its full capacity (e.g., from 1983 to 1999 in Figure 2-1). When completely filled, the non-reservoir upstream storages unrealistically dampen the seasonal variation of reservoir storage (e.g., from 1999 to 2010 in Figure 2-1).

It is noted that SBE is a virtual phenomenon which would not occur if a perfect DEM is used. For example, let's assume there is a reservoir where the amount of its upstream river storage capacity is comparable to that of reservoir storage capacity due to wrongly parameterized bathymetry that has too flat profile from the reservoir to its upstream. In this case, the excessive SBE becomes obvious as the significant amount of water stored in the non-reservoir upstream cells becomes comparable to reservoir storage itself. The issue is that the perfect DEMs don't exist especially for large regions; hence, a proper treatment of SBE becomes essential for modelling the existing reservoirs in LHFD.

Here, we eliminate the unintended behavior in storage simulations due to excessive SBE by first improving the parameterization of river-reservoir beds and floodplain elevations (Chapter 2.2.3.3) and then by imposing a constraint on reservoir boundaries. At the boundaries, the slope between water level at non-reservoir cell and bed level of reservoir cell is used as the potential energy gradient at the interface between the reservoir cell and non-reservoir cell for surface water routing. Such treatment of water surface gradient is identical to continually making the bed elevation of the upstream non-reservoir cells equal to the water level of the reservoir.

2.2.2. Data and Preprocessing

2.2.2.1. Dams and Reservoir Information

We use the dams and reservoir information from the Global Reservoir and Dam (GRanD) database (Lehner et al., 2011a, 2011b). A total of 1,889 reservoirs within the CONUS domain, including some reservoirs in the Canadian portion of the Columbia and Missouri river basins, are imported (Figure 2-2a). The GRanD database provides the location and height of dams and the areal extent of reservoirs as well as other details such as the storage capacity, construction year,

and purpose of reservoir. Using the latitude and longitude information, dams can be located on the river network of raster model grids derived from HydroSHEDS flow direction map (Lehner et al., 2008). However, as spatial resolution becomes finer, such a simple method, when automated, often yields significant inaccuracies causing dislocations of main stem dams to the tributaries and vice versa. Such wrongful assignment of dam locations can cause severe problems in hydrologic simulations. For example, if a tributary dam is located in the main stem, a significantly larger drainage area could be erroneously assigned for that reservoir, which results in frequent over-filling and spilling of the reservoir. On the contrary, when a smaller basin area is assigned to a reservoir which should have had a larger basin area, under-filling and excessively underestimated release can be caused. These are inevitable problems in high-resolution surface water modeling using raster grid flow direction maps that determine the direction of flow from a grid cell to its downstream among eight directions (i.e., 4 in cardinal and 4 in diagonal directions) even though, in reality, surface water can flow in any direction (see Shin & Paik, 2017 and references therein). In this study, we resolve these issues by comparing the drainage area at a reservoir location estimated by the model with that obtained from GRanD database. If discrepancies in the two drainage areas are found for any dam, the dam location is adjusted to match the model estimated drainage area with that from GRanD. Among the neighboring cells of the cell located based on the given latitude and longitude, the nearest cell whose estimated drainage area differs from GRanD database drainage area by less than 20% (an arbitrarily set threshold) is determined as a dam location (Figure 2-3).

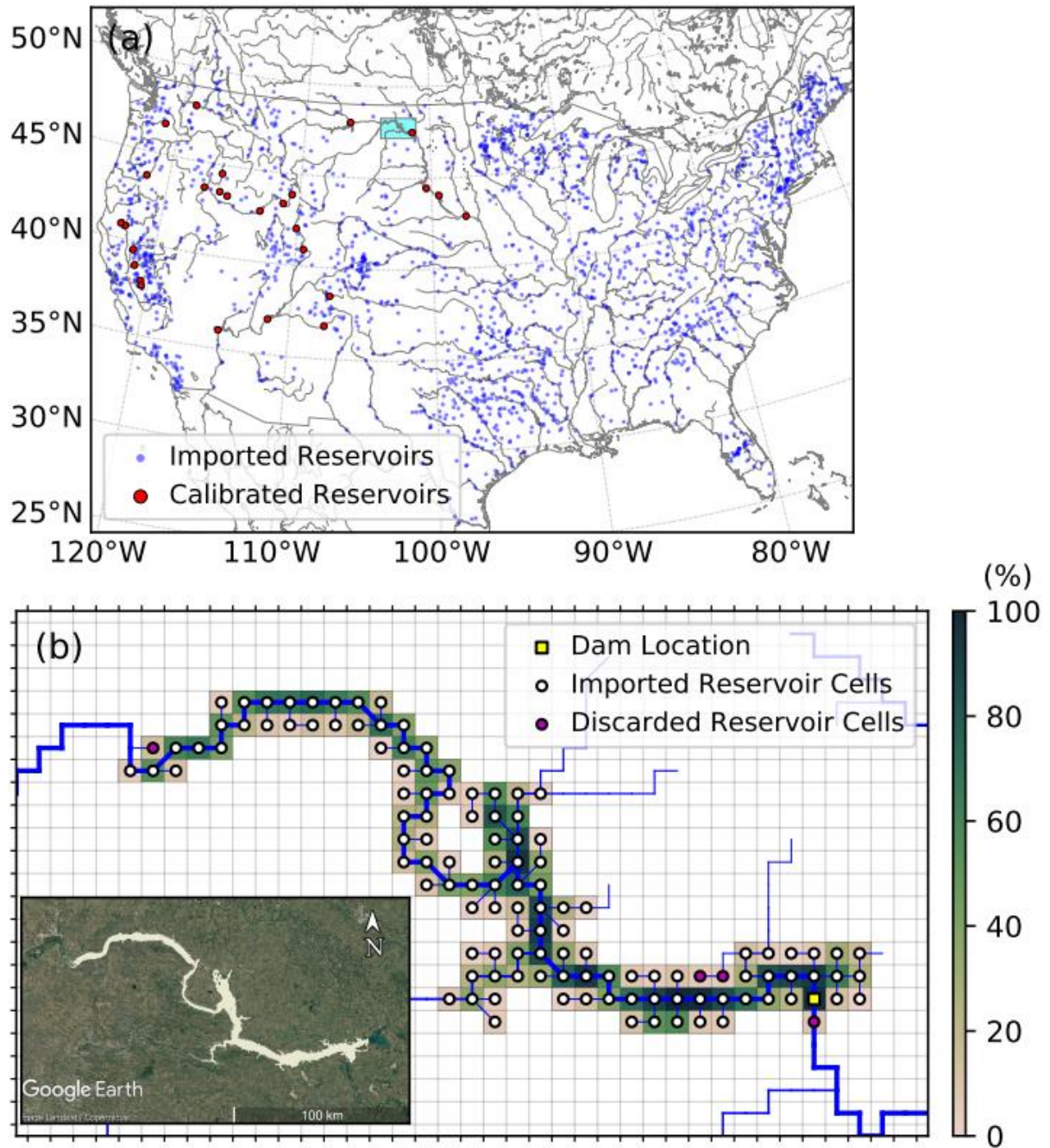


Figure 2-2 Reservoirs locations and an example of imported surface extent. (a) The 1,889 reservoirs simulated in LHFD model (blue circles) and 27 calibrated reservoirs (red circles), and (b) the rasterized maximum reservoir extent of Lake Sakakawea in the Missouri river shown by a cyan box in (a). The color coding in (b) represents the fraction of GRanD reservoir extent within LHFD grid cells. River network is shown by blue lines with the width scaled using the simulated river discharge. The inset in (b) shows Landsat imagery derived using Google Earth with the vector-form reservoir extent from the GRanD database shown in white.

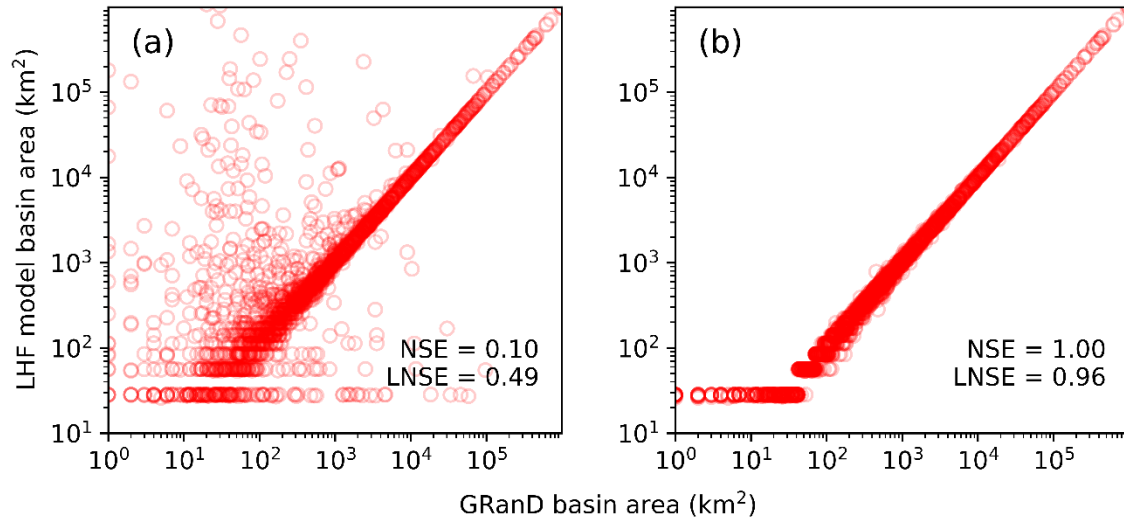


Figure 2-3 Comparison of drainage area at dam locations based on GRanD database and LHF model (a) before and (b) after the application of coordinates correction. NSE and LNSE are Nash–Sutcliffe efficiency coefficient and Log Nash–Sutcliffe efficiency coefficient, respectively.

In the newly developed scheme, a reservoir storage is no longer aggregated to a dam location but is spread over multiple upstream cells from the dam location. Hence, the maximum reservoir extent has to be set to diagnose the total amount of reservoir storage for a given surface water profile. Considering seasonally varying reservoir surface area, the maximum reservoir extent should be sufficiently large enough to cover the reservoir when it is completely filled. For this purpose, we convert each reservoir polygon of GRanD database to raster grids to define the maximum reservoir extent. When the polygon is converted to raster grids, all grid cells having any overlaps with the polygon (Figure 2-2b, all color-filled cells) are preliminary classified as reservoir cells. In many cases, not all grid cells within the preliminary reservoir extent are hydraulically connected to the main reservoir body (Figure 2-2b, cells with red-filled circles). The disconnected cells are small in number and account for small portion of reservoir extent in GRanD database (see small background values and the number of red circles in Figure 2-2b),

thus we discard those disconnected cells and import the remaining cells as the maximum reservoir extent (cells with white-filled circles in Figure 2-2b). This process is repeated for all 1,889 reservoirs.

2.2.2.2. Water Use Data

Downstream water use data is required for simulating reservoir release at each dam location. We use the data from the US Geological Survey (USGS) that is available for 1981-2010 period (Maupin et al., 2014). USGS provides the averaged water use at 5-year intervals but the model needs daily to monthly water use. Therefore, we temporally disaggregate the USGS data to the monthly scale by imposing the monthly irrigation water use patterns simulated by our 1° global model HiGW-MAT (Y. Pokhrel et al., 2015) as shown in the example of Butte County, California in Figure 2-4. Total irrigation water use (Figure 2-4a, red boxes) is disaggregated following the seasonal variability of monthly irrigation (Figure 2-4b). Here, the monthly irrigation demand is imported from HiGW-MAT model that incorporates the information on irrigated areas, crop types, and crop calendar (Y. Pokhrel et al., 2015). To consider both inter- and intra-annual variability, the monthly irrigation fraction is calculated for every 5-years, i.e., dividing monthly irrigation demand by 5-year average demand. Water uses in the sectors other than irrigation (Figure 2-4a, green boxes) are assumed to remain constant throughout the year since irrigation dominates water use seasonality while the others do not vary significantly. The monthly water use (Figure 2-4c) is derived by adding the irrigation water use disaggregated by the monthly irrigation fraction to the other water uses. This method generates a monthly time series of water use with seasonal and inter-annual variability while preserving the total amount of water use for each 5-year intervals.

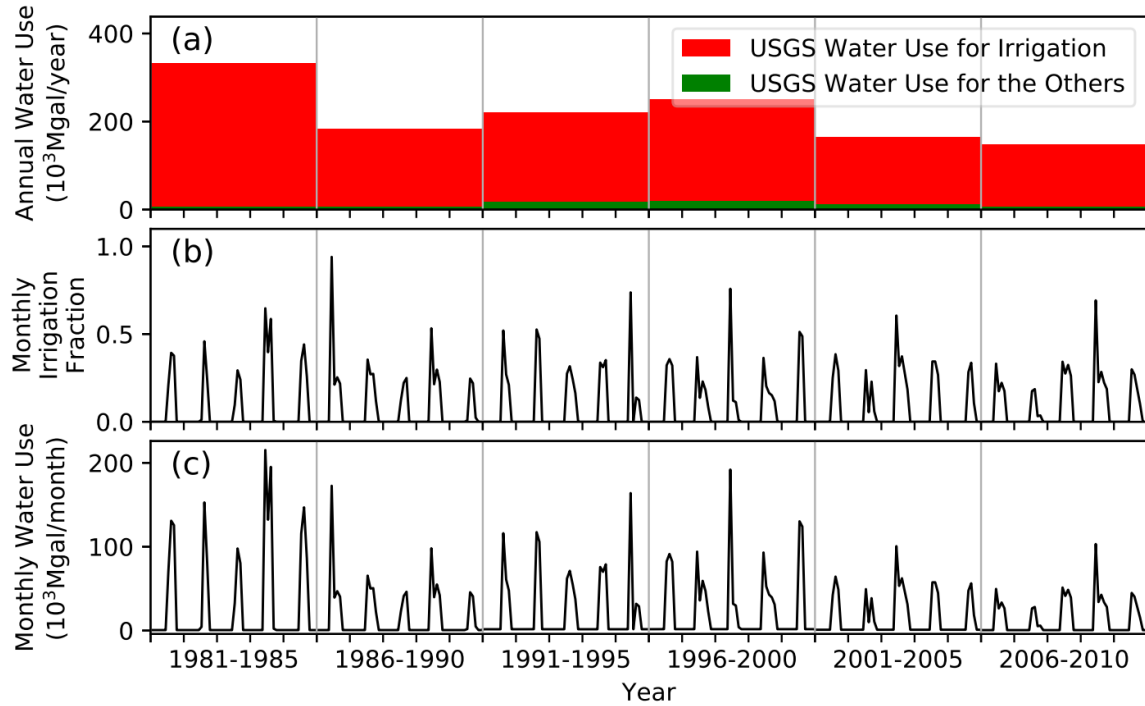


Figure 2-4 Temporal disaggregation of USGS water use data to monthly time scale for Butte county in California. (a) The averaged USGS water use in 5-year intervals, (b) monthly irrigation fraction to total irrigation amount, and (c) total monthly water use.

To allocate water uses to each reservoir, the county-based values are then regridded to 5 km model grids. Each reservoir fulfills the downstream demands in the region within a given distance from the reservoir, located at lower elevation than the reservoir. There is a varying range of downstream extent used in previous studies: 100 km for high-resolution simulations over the contiguous US (Voisin et al., 2017), and 250 km (Biemans et al., 2011; Haddeland et al., 2006) and 1000 km (Hanasaki et al., 2006) over the globe. In this study, we set the downstream extent to 200 km, which is larger than the value of Voisin et al. (2017) but smaller than those used in global studies. Our rationale is that a sufficiently large downstream extent needs to be considered in modeling large river basins such as the Colorado and Columbia, but 1000 km could be too large which is in the order of the entire length of such large rivers. To prevent excessive demand allocation, an upper limit of 0.8 is set for *DPI* (demand per inflow; see

Chapter 3.2.1 for detail), which is equivalent to further reducing the downstream extent if necessary.

2.2.2.3. River-reservoir Bed and Floodplain Elevations

Integrated river-floodplain-reservoir routing requires reliable terrain data that represent bare-earth elevations. Acquiring such data for existing reservoirs is challenging, if not impossible, because the available DEMs provide only water surface elevations over reservoirs which can sometimes be in tens to hundreds of meters above the actual reservoir bed elevation (e.g., red lines in Figure 2-5a). Alternatively field survey and remotely sensed bathymetry data (e.g., Gao, 2015) can be used but (1) field surveys are sparse, and (2) remotely sensed data are available only for a limited number of reservoirs and cover only the non-permanent parts of the water body. To overcome these data limitations, here we derive reservoir bed elevations assuming that (1) an abrupt elevation drop on the longitudinal river profile occurs at reservoir locations, which closely corresponds to dam height and (2) most rivers have a concave upward profile resulting from geologic, hydrologic, and climate conditions (Figure 2-5a).

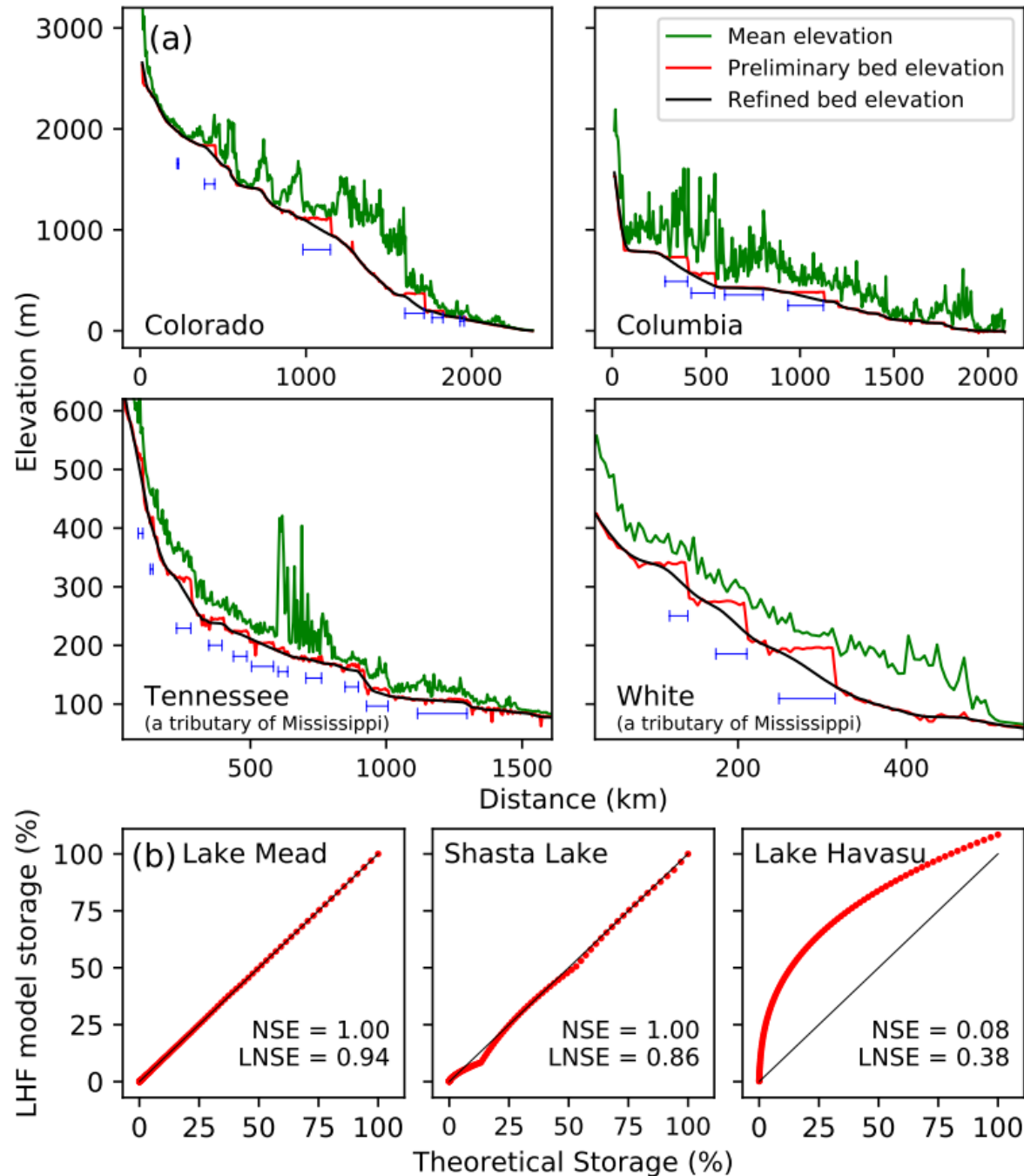


Figure 2-5 River and reservoir elevation parameterizations. (a) The longitudinal profiles of mean, preliminary, and refined bed elevations for Colorado, Columbia, Tennessee, and White rivers. The blue horizontal bars show the location and longitudinal extent of the major dams. For Tennessee and White rivers only the middle reach is shown, where dams exist. (b) Storage-depth parameterization using theoretical inverted-triangle reservoir formulation for Lakes Mead, Shasta, and Havasu (red dots). Black diagonal lines represent 1:1 lines.

To derive river-reservoir bed and floodplain elevations, we use MERIT DEM (Multi-Error-Removed Improved-Terrain DEM; Yamazaki et al., 2017), which is based on SRTM DEM (Shuttle Radar Topography Mission DEM) but includes multiple errors corrections made by separating absolute bias, stripe noise, speckle noise, and tree height bias using multiple satellite datasets and filtering techniques. In particular, distortions in topography slopes in SRTM DEM and other inconsistencies in error removal method have been improved in MERIT DEM, hence MERIT DEM is suitable especially for terrain-dependent hydrologic applications such as reservoir-floodplain simulations (D. Yamazaki et al., 2017). In principle, the flow direction results from one DEM is not applicable to another DEM, hence the use of MERIT DEM requires the retrieval of flow directions that can be conducted by various automated methods (e.g., Shin & Paik, 2017), however manual corrections are essential which involve tedious and laborious tasks for large scale modeling. Hence, instead of retrieving new flow directions from MERIT DEM, we use the readily available flow direction data from HydroSHEDS (Lehner et al., 2008) which is already manually corrected, is also based on SRTM DEM, and has been widely used (e.g., Fan & Miguez-Macho, 2011; Gong et al., 2011; Wada, de Graaf, et al., 2016). To verify the consistency of MERIT DEM and HydroSHEDS-based flow directions, we compared the longitudinal river-reservoir bed profiles for selected river basins; it is found that HydroSHEDS flow direction becomes consistent with MERIT DEM when the spatial resolution is upscaled to the current model grid size of 5 km (Figure 2-6). The HydroSHEDS flow direction map is used after upscaling it to 5 km model grids in LHFD using a similar approach as in Miguez-Macho and Fan (2012a), which is based on Yamazaki et al. (2009). Detailed description of flow direction upscaling is provided below.

To utilize flow directions from high-resolution DEM for coarse-resolution DEM, we employ the method of Yamazaki et al. (2009) with some modifications. While the original method of Yamazaki et al. (2009) allows designating the downstream grid cell among any grid cells in the domain, a common convention of designating downstream cell is to choose one among 8-neighboring grid cells. Here, we follow the common convention, which makes our method slightly different than the method of Yamazaki et al. (2009) in that the flow direction is chosen among 8 directions (i.e., 4 cardinal and 4 diagonal directions). In short, the upscaling procedure can be summarized as follows. Among fine-resolution pixels within a coarse-resolution grid cell of interest, the pixel having the largest upstream area is chosen as the outlet pixel. While tracing down the pixels along the fine-resolution flow path from the outlet pixel, the nearest outlet pixel of other grid cells is identified as the tentative next outlet pixel. If the grid cell containing the tentative next outlet pixel is one of 8-neighboring grid cells from the grid cell of interest, the given grid cell is determined as the downstream grid cell. Otherwise, among the 8-neighboring grid cells from the grid cell of interest, the grid cell containing the nearest pixel on the fine-resolution flow path is determined as the downstream grid cell.

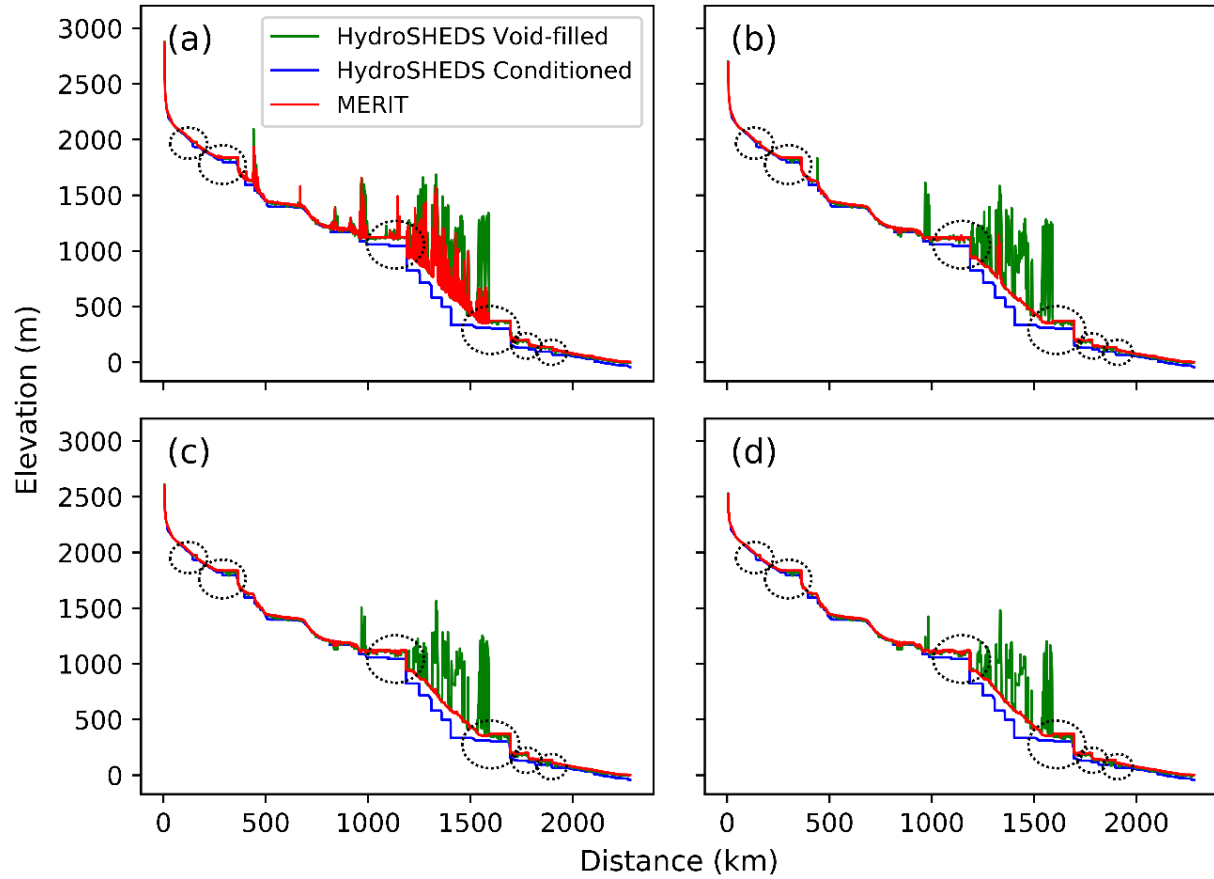


Figure 2-6 Longitudinal bed profiles of Colorado river derived from 90 m HydroSHEDS void-filled (green), HydroSHEDS conditioned (blue), and MERIT (red) DEMs. The elevations of (a) the cell on the flow path, and the lowest cell among the (b) 10th ($\approx 1.8\text{km}$), (c) 20th ($\approx 3.6\text{km}$), and (d) 30th ($\approx 5.4\text{km}$)-order neighboring cells from the flow path are used to derive the profiles. Dotted black circles represent the reservoir locations in the order of Fontenelle, Flaming Gorge, Lake Powell, Lake Mead, Lake Mohave, and Lake Havasu (from upstream to downstream). The longitudinal profiles are extracted based on HydroSHEDS flow directions. As higher order neighboring cells are used, the noise on MERIT DEM profile by the discrepancy between HydroSHEDS flow directions and MERIT DEM decreases. It is found that the void-filled HydroSHEDS has large noises and the conditioned HydroSHEDS has artificially lowered and stepwise longitudinal bed profiles even on the sections where dams do not exist. MERIT DEM contains less noises and has stepwise longitudinal profiles only where dams exist.

Since MERIT DEM does not provide river-reservoir bed elevations, especially where reservoirs exist, we devise a new algorithm to derive reservoir bed elevations using the information of surface extent of reservoirs (Chapter 2.2.3.1). We apply the following procedure for the entire study domain; example results for the Colorado, Columbia, and Mississippi river

basins are shown in Figure 2-5a. First, to derive the first-order estimate of river-reservoir bed elevations, the minimum (Figure 2-5a, preliminary bed elevation, red line) values of 90 m DEM cells within a 5 km model grid cell are selected, assuming that the cell with the lowest elevation is generally the river mouth of each model grid cell. Then, we obtain an elevation profile by fitting the elevations between upstream and downstream cells of the reservoir using an exponential function (Tanner, 1971) that is widely used for describing longitudinal bed profiles. The elevation of cells along the fitted profile are lowered to the fitted profile. By doing so, large water body elevations in sections marked blue in Figure 2-5a are removed. Finally, to remove spikes and pits with minimal distortion of river-reservoir bed profiles, depressions are filled after applying the locally weighted scatterplot smoothing (LOWESS) filter (Cleveland, 1979) (Figure 2-5a, refined bed elevation, black line). As this procedure is repeated for every flow reaches in the model domain (e.g., a flow reach starting from the middle of the main reach of Colorado river), every model grid cell is treated to have smoothly refined bed elevations. This process results in the removal of tens to hundreds of meters of reservoir water depth to obtain the bed elevations.

In LHF, each grid cell is considered to have a rectangular river channel cross-section. Flood water (i.e., overbank flow) that overtops the river channel is simulated to be evenly spread over the flat floodplain (e.g., Fan et al., 2017; Neal et al., 2012). Current version of LHFD employs the same river cross-section parameterization method for reservoir parameterization: each cell has a river-reservoir bed elevation (Figure 2-5a, black line) and a floodplain elevation (described next) regardless of whether it is a non-reservoir or a reservoir cell; bed and floodplain elevations are assumed to be flat within a grid cell. We note that reservoir and non-reservoir cells are identically modeled and the information on whether a cell is a reservoir cell (Chapter 2.2.3.1;

Figure 2-2b) is used only for diagnosing the reservoir storage, which is the sum of surface water stored in all cells within the reservoir.

In LHF, the floodplain elevations were determined from high-resolution DEM using the climatological equilibrium water table (EWT) as a reference (Miguez-Macho & Fan, 2012a); that is, when a 5 km model grid cell corresponds to multiple high-resolution DEM pixels, assuming that the pixels lower than EWT represent perennial rivers, the floodplain elevation is determined to the average elevation of the pixels higher than EWT. This method could be reasonable when natural rivers are of interest, but as reservoirs are additionally considered in LHFD, the river-reservoir bed and floodplain elevations are additionally required to be parameterized to reasonably represent the reservoir bathymetry and the storage-depth relationship. For example, the reservoir storage when a reservoir is completely filled (i.e., water level reaches near dam crest) should be equal to the storage capacity; however, the storage at that water level can be calculated to be far more (or less) than the storage capacity due to prevailing large errors in DEMs, for which a proper treatment of topography data is unavoidable.

Owing to the lack of observations, we use the inverted triangle storage-depth relationship (Liebe et al., 2005; $V = ah^3$ and $A = dV / dh = 3ah^2$ where V , A , h , and a are storage, surface area, depth, and shape factor, respectively), which is one of the widely used relationships in global scale studies (Adam et al., 2007; van Beek et al., 2011; Wada et al., 2014). First, for reservoir cells (Chapter 2.2.3.1; Figure 2-2b), the mean values of 90 m DEM cells within a 5 km model grid cell (Figure 2-5a, green line) are regarded as preliminary floodplain elevations. Second, assuming the increasing water level that is flat within a reservoir, we adjust floodplain elevations of reservoir cells to satisfy the inverted triangle storage-depth relationship. Most

reservoirs can be well parameterized to represent the given relationship as shown as a straight profile or a partly uneven profile in comparison of theoretical and modeled storages (Figure 2-5b). A deviating profile of some reservoirs is attributed to the use of flat floodplain geometry, which inevitably incurs sudden large storage increments at water levels where the water overtops the floodplains. All aforementioned procedures are systemically automated, hence enabling an easy inclusion of any available site-specific data to better represent bathymetry and storage-depth relationship.

2.2.2.4. Atmospheric Forcing and Other Parameterizations

We use the meteorological forcing data from North American Regional Reanalysis (NARR) (Mesinger et al., 2006), which fully assimilates the observations from multiple sources, making it suited for driving continental scale hydrological models to mimic the observed dynamics of water flows and storages. NARR produces the full atmospheric fields from 1979 to present and is available at 3-hourly step; the original data at 32km grids are spatially interpolated using bilinear interpolation method to model grid resolution as done in our previous studies (Miguez-Macho & Fan, 2012a; Y. Pokhrel et al., 2013, 2014). All other model parameters are identical to those used in Fan et al. (2007), Miguez-Macho et al. (2007), and Miguez-Macho and Fan (2012a).

2.3. Results and Discussion

Figure 2-7 shows the spatial patterns of the integrated simulation of river-floodplain-reservoir storage at 5km model grids over the entire CONUS. This figure demonstrates that the broad spatial patterns of storages in rivers, reservoirs, and floodplains are clearly captured by the model for large river basins. Validating these results over the whole study domain is not possible due to the lack of spatially-varying data of reservoir storage, depth, and extent, therefore we focus on selected river basins and reservoirs. The comparison of the reservoir surface extent with a satellite-based data for a portion of Colorado, Columbia, and Mississippi river basins (shown by rectangles in the top panel of Figure 2-7) is presented in the bottom panel of Figure 2-7. The comparisons for Yellowstone, Missouri, Ohio, and Tennessee river basins are provided in Figure 2-8.

The left column of the bottom panel in Figure 2-7 and Figure 2-8 shows the surface water occurrence data from Pekel et al. (2016) and the middle column presents the water storage depth from this study (i.e., a zoomed-in view of the results shown in the top panel). The surface water occurrence data represent the presence of “open to sky” water over the globe at 30 m resolution from 1984 to 2015 (e.g., the grids with permanent ground and permanent surface water have 0% and 100% values, respectively). Note that for a consistent comparison of results at the model grid scale of 5km, the 30m data from Pekel et al. (2016) is spatially averaged to 0.04° grids following Yamazaki et al. (2015). Even though a direct comparison and evaluation of the simulated storage depth cannot be made because the data from Pekel et al. (2016) provides only the extent of surface water occurrence, these comparisons evidently suggest that the overall spatial patterns of river-reservoir-floodplain storages, especially the water storage extent in the upstream of the major reservoirs (reservoirs are shown as red dots in the left column of bottom panel in Figure 2-

7), are well captured by the model. In the Colorado river basin, the cascade reservoirs are accurately captured by the model and in the Mississippi both the flood extent along the main stem as well as the surface water extent in many small and large reservoirs can be readily discerned. A larger flood extent in the model can be seen along the Mississippi valley alluvial plain and its downstream, which could be because of an actual model overestimation of flood, the effect of vegetation over water bodies not captured in the open water data, or the inconsistency in temporal aggregation between the model results and the data from Pekel et al. (2016).

Also shown in Figure 2-7 (right column of the bottom panel) are the results of river-reservoir storage from our global model (Y. Pokhrel et al., 2015) at 1° grids that used the original H06 reservoir scheme. We present these comparisons with a global model to demonstrate the major improvements made in the present study over the previous global studies in which multiple reservoirs are lumped into a single grid cell and reservoir storages are spatially spread across a large grid cell with relatively small storage depth. Note the large storage depth simulated by the new model around the dam locations in the Colorado river (Figure 2-7, lower panel middle column). The above described spatial features of river-reservoir-floodplain storage in Colorado, Columbia, and Mississippi river basins are similarly found in the Yellowstone, Missouri, Ohio, and Tennessee river basins (Figure 2-8). Some recent studies (e.g., Voisin et al., 2017; Wada, de Graaf, et al., 2016) have used the global models at a relatively finer grid (i.e., 10-15 km), but they use the similar approaches as in the global studies of Pokhrel et al. (2015).

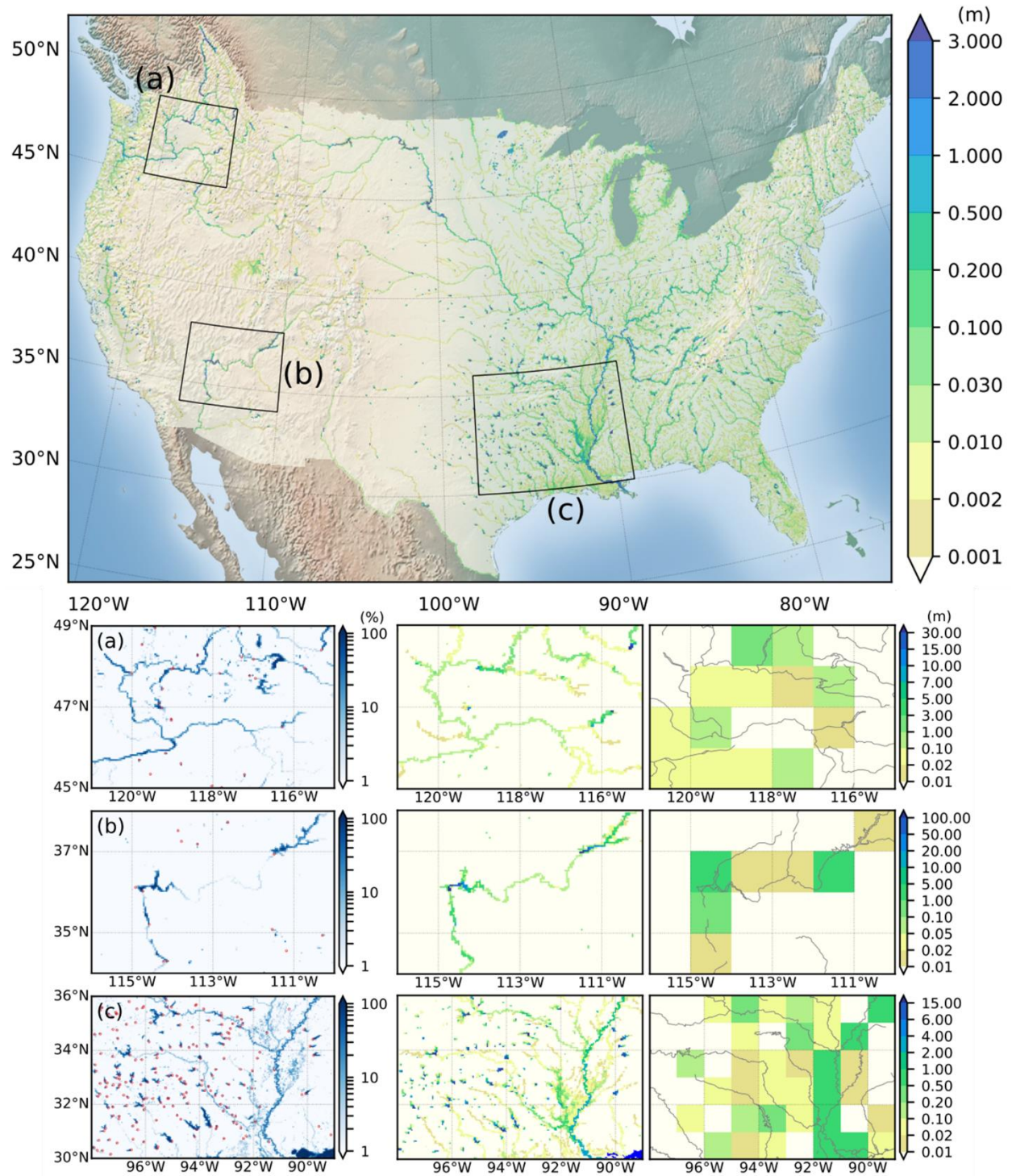


Figure 2-7 Simulated river-reservoir-floodplain storages averaged over 1985-2010 period (top; background shows shaded topographic relief). The bottom panels show the comparison of simulated storage from this study (middle) with the surface water occurrence data from Pekel et al. (2016) (left), and 1° grid global model results from Pokhrel et al. (2015) (right) for (a) Columbia, (b) Colorado, and (c) Mississippi river basins shown by black rectangles in the top

panel. The lower-right region in the Mississippi subplot, shown as dark blue color, is a part of the ocean. Red circles on the left column indicate dam locations. Simulated storages are grid-averaged water depths. The color coding for the middle column is same as that for the right column.

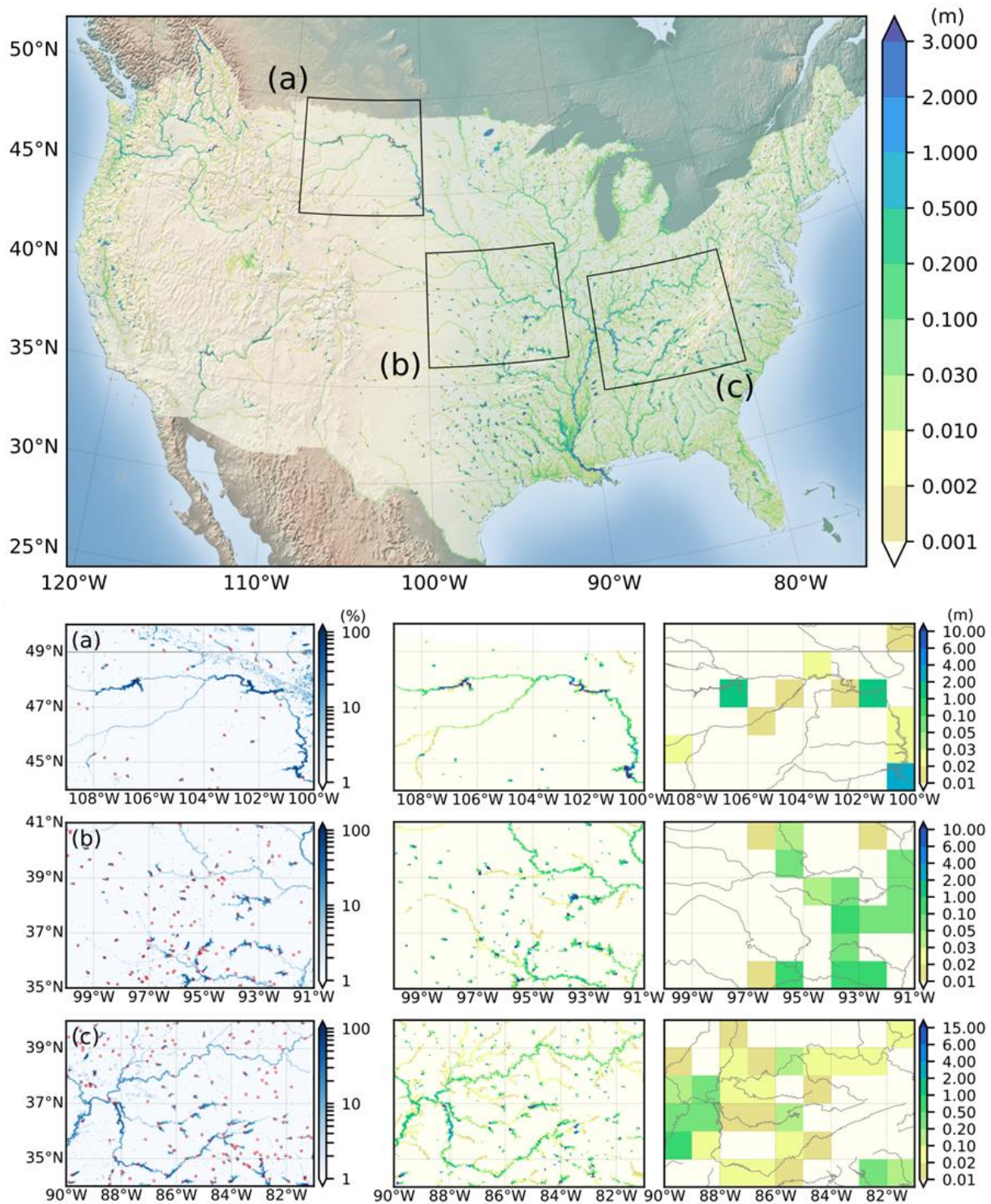


Figure 2-8 Same as in Figure 2-7 but for additional regions: (a) Yellowstone and upper Missouri, (b) lower Missouri, and (c) Ohio and Tennessee river basins.

2.4. Summary and Conclusion

This study presents the first results of a fully coupled river-reservoir-floodplain storage simulations at 5km grids over the CONUS. First, a new approach for processing DEM to derive reservoir bed elevation is presented, which is critical for spatially explicit representation of reservoir storage dynamics in high-resolution simulations. Second, 5-yearly water use data in the downstream of dams, which determines reservoir release, is temporally disaggregated to monthly values by using the temporal variations in irrigation water use obtained from global model simulations. Third, the issues of Storage Buffer Effect (SBE) is identified, and a new approach is proposed to eliminate SBE in the upstream of reservoirs. The comparison of simulated spatial distribution of integrated river-reservoir-floodplain storage with remote-sensing based water extent data demonstrates a promising capability of the model to simulate the spatial extent over and around large reservoirs and floodplains.

The river-reservoir-floodplain parameterization can also be enhanced further by utilizing the data from satellite altimetry (e.g., Envisat and GLAS/ICESat) and surface water extent from remote sensing (e.g., MODIS and Landsat). The use of finer grids (Pokhrel et al., 2013) or sub-grid topography (Yamazaki et al., 2011) could enable a more detailed simulation of surface water storage dynamics. Despite some limitations, the present study presents a framework for explicit simulation of reservoir storage and surface extent dynamics that can be used within hyper-resolution hydrological models, thus providing a major advance over previous studies on large-scale reservoir simulations. While the model is tested over the CONUS at 5km grids in the present study, the scheme and data processing algorithms can be seamlessly incorporated into any high-resolution river-floodplain routing models and applied over other regions at scales ranging from a river basin to the entire globe using site-specific and global datasets (e.g., GRanD

database, MERIT DEM, and satellite-based products). According to a recent study (Fleischmann et al., 2019), the continental scale hydrodynamics models are found to yield satisfactory results when the modeling reach length is small ($<15\text{km}$; 1-5km are preferable). The current grid size of 5km is in their recommended range, but it is possible to reduce the grid size. The only problem in reducing the grid size is computational cost, hence it would add more value on the newly developed model when the numerical scheme is optimized to reduce the computational cost.

Chapter 3. Development of an Improved Reservoir Operation Scheme

3.1. Introduction

Modeling reservoirs involves determination of storage and release by using the information on inflow, storage capacity, and downstream demands. Owing to the difficulty in representing individual operation rules in large-scale models, studies have used generic operation schemes to simulate reservoir operation within continental and global scale hydrological models. Early works simulated reservoir releases by using a rectangular weir equation or retarding flow velocity (Coe, 2000; Döll et al., 2003; Meigh et al., 1999). Pioneering works on grid-based, explicit simulation of reservoirs in global models were presented by Hanasaki et al. (2006) and Haddeland et al. (2006). A number of subsequent studies have improved and incorporated these schemes into various other global hydrological models (GHMs) and land surface models (LSMs) (e.g., Adam et al., 2007; van Beek et al., 2011; Biemans et al., 2011; Pokhrel et al., 2015; Pokhrel, Hanasaki, Koirala, et al., 2012; Voisin et al., 2013; Wada et al., 2014), and other studies have modified them for reservoir-specific applications by including operation rules for the individual reservoirs (Mateo et al., 2014; G. Zhao et al., 2016).

In this Chapter, an improved reservoir operation scheme based on the original scheme of Hanasaki et al. (2006) is presented with analytical comparisons of existing and new operation schemes, and a new calibration method that is computationally efficient is proposed in Chapter 3.2. The new reservoir scheme incorporated within LHFD model is applied to the CONUS with the various simulations settings (Chapter 3.3), and the simulations results are presented and discussed in Chapter 3.4. Lastly, summary and conclusion are given in Chapter 3.5.

3.2. Improvements on Reservoir Operation Scheme

3.2.1. The Improved Reservoir Operation Scheme

Building upon the schemes of Hanasaki et al. (2006) (hereafter, H06) and Biemans et al. (2011) (hereafter, B11) we develop an enhanced reservoir operation scheme by improving the parameterizations in these existing schemes and adding new capabilities to better simulate reservoir storage and release dynamics. For each operational year, starting with the first month when monthly mean inflow changes from above to below the annual mean flow (Hanasaki et al., 2006), these schemes determine the total amount of annual release based on the initial reservoir storage and impose the variability of monthly release considering the seasonality of water use. There are two common issues in these parameterizations that we address in this study: (1) excessive release in high demand season and (2) unstable storage simulation for small reservoirs. In the following, we introduce the revised scheme first and provide the comparisons with H06 and B11 as necessary.

The inter-annual variability of release is determined by the release coefficient (k_{rls} [-]), which is the ratio between the initial storage at the beginning of the operational year (S_0 [L³]) and the long-term target storage (αC [L³]), where α is a non-dimensional constant set to 0.85 (Hanasaki et al., 2006) and C [L³] is the reservoir storage capacity taken from GRanD database. The release coefficient is calculated as:

$$k_{rls} = \frac{S_0}{\alpha C} \quad (3-1)$$

Then, the provisional monthly release (r'_m [L³/T]) is calculated as:

$$r_m' = \bar{i}_m + d_m - \bar{d}_m \quad \text{if } DPI < 1 - M \quad (3-2a)$$

$$r_m' = \bar{i}_m (M + (1 - M) d_m / \bar{d}_m) \quad \text{otherwise} \quad (3-2b)$$

where \bar{i}_m and \bar{i}_m are long-term monthly and annual mean inflow [L^3/T], respectively, d_m and \bar{d}_m are monthly and annual mean demand [L^3/T], respectively, DPI is the ratio between annual mean demand and annual mean inflow ($= \bar{d}_m / \bar{i}_m$) [-], and M is the ratio between the minimum monthly release and long-term annual mean inflow [-] that assures $r_m' \geq M \bar{i}_m$. Regardless of the value of M , which can be arbitrarily set to 0.1 (B11), 0.5 (H06), or any other values, the expected value of r_m' over the operational year is mathematically equal to \bar{i}_m . Note that d_m can comprise various demands including domestic, industrial, irrigation, power generation, and others depending on the purpose of reservoirs. By considering the seasonality of various demands, the reservoir scheme is devised to mimic the generic behavior of reservoirs with respect to their purpose.

The targeted monthly release, r_m , can then be calculated as:

$$r_m = R k_{rls} r_m' + (1 - R) \bar{i}_m \quad \text{where } R = \min(1, \alpha c) \quad (3-3)$$

where R is the demand-controlled release ratio [-], c is the ratio between capacity and mean annual inflow ($= C / (\bar{i}_m \cdot 1 \text{ year})$) [-]. As R varies from 0 to 1, the reservoir release changes from run-of-the-river flow to demand-controlled release.

In addition to r_m , all of the excess water is released when the reservoir is full. Conversely, release is prevented when the storage reaches to the minimum level. Finally, reservoir release is calculated under these two constraints of spilling and minimum storage level.

3.2.2. Analytical Comparison with the Existing Reservoir Operation Schemes

We propose the following two major improvements to address the issues identified earlier. First, we propose using “ $DPI < 1-M$ ” in equation (3-2) to prevent excessive release in high demand season; the existing schemes use “ $DPI < 0.5$ ”. Equations (3-2a) and (3-2b) aim to fully satisfy water needs in low-demand regions and partially satisfy the needs in high-demand regions, respectively (Hanasaki et al., 2006). Equation (3-2b) is comparable with the hedging rule that preserves some water to meet the future demands because high DPI makes a reservoir susceptible to drought conditions. Even if M is adjusted by user preference, equation (3-2b) should produce a dampened release pattern compared to the release pattern from equation (3-2a). However, unless proper modification of the criterion (i.e., $DPI < 1-M$) is followed the release variability gets amplified instead of being dampened. The analytical derivation of $DPI < 1-M$ is provided below.

Using equation (3-2) we can write:

$$r'_{\max,(a)} = (1 + (D_{\max} - 1)DPI)\bar{i}_m \quad (3-4)$$

$$r'_{\min,(a)} = (1 + (D_{\min} - 1)DPI)\bar{i}_m \quad (3-5)$$

$$r'_{\max,(b)} = (M + (1 - M)D_{\max})\bar{i}_m \quad (3-6)$$

$$r'_{\min,(b)} = (M + (1 - M)D_{\min})\bar{i}_m \quad (3-7)$$

Where $r'_{\max,(a)}$, $r'_{\min,(a)}$, $r'_{\max,(b)}$, and $r'_{\min,(b)}$ are the maximum and minimum provisional monthly release calculated from equations (3-2a) and (3-2b), respectively, D_{\max} and D_{\min} are the maximum and minimum of $d_m/\overline{d_m}$, respectively, M is the minimum release ratio, DPI is the ratio between annual mean demand and annual mean inflow, and $\overline{i_m}$ is the annual mean flow. Then, the differences of maximum and minimum values between equations (3-2a) and (3-2b), Δ_{\max} and Δ_{\min} , are:

$$\Delta_{\max} = r'_{\max,(a)} - r'_{\max,(b)} = (1 - D_{\max})(1 - M - DPI)\overline{i_m} \quad (3-8)$$

$$\Delta_{\min} = r'_{\min,(a)} - r'_{\min,(b)} = (1 - D_{\min})(1 - M - DPI)\overline{i_m} \quad (3-9)$$

Compared to the use of equation (3-2a), if the use of equation (3-2b) enables less variability in release, Δ_{\max} and Δ_{\min} should be positive and negative, respectively. Since $D_{\max} \geq 1$, $D_{\min} \leq 1$, $\overline{i_m} > 0$, the equation (3-2a) should be used when

$$DPI < 1 - M \quad (3-10)$$

Second, we propose using $R = \min(1, \alpha c)$ instead of $R = \min(1, 4c^2)$ (H06; B11). Here we provide an analytical derivation of a new equation for R . The target storage, S_{target} , can be calculated from a simple mass balance as follows:

$$S_{\text{target}} = S_0 + \overline{i_m} \cdot (1 \text{ year}) - k_{rls} \overline{i_m} \cdot (1 \text{ year}) = S_0 + \frac{C}{c} - \frac{S_0}{\alpha C} \frac{C}{c} = S_0 \left(1 - \frac{1}{\alpha c} \right) + \frac{C}{c} \quad (3-11)$$

After the rearrangement of equation (3-11),

$$\frac{S_{\text{target}}}{C} = \left(1 - \frac{1}{\alpha c} \right) \frac{S_0}{C} + \frac{1}{c} \quad (3-12)$$

The relationship between initial storage and target storage for varying c of equation (3-12) is shown in Figure 3-1a, which demonstrates the need for new parameterization of R in equation (3-3). The equation (3-3) is intended to prevent overflow and storage depletion when reservoir storage capacity is small compared to annual flow (i.e., lower case c) by allowing some portion of run-of-the-river flow (Hanasaki et al., 2006). The need of equation (3-3) comes from the assumption in equation (3-1) where the initial storage scaled to the reservoir storage capacity (i.e., S_0 / C) serves as a surrogate for potential outflow scaled to the expected inflow (i.e., k_{rls}) to achieve a long-term target storage (i.e., αC). Hence, the rate of outflow variation (e.g., 20 % reduction/increment in outflow) contributes to the rate of storage change by $1/c$ times of it (e.g., $20/c$ % reduction/increment in storage). As a result, when c is large, equation (3-1) allows reservoir storage to be gradually guided to αC rather than abruptly filling or releasing the storage up to αC within a year; conversely, when c is small, unless a proper reduction of R is followed, the storage simulation is expected to be unstable since the target storage (S_{target}) is repeatedly set to either $S_0 < \alpha C < S_{\text{target}}$ or $S_{\text{target}} < \alpha C < S_0$ that causes frequent over-filling and under-filling; hence the reduction of R is needed for those cases.

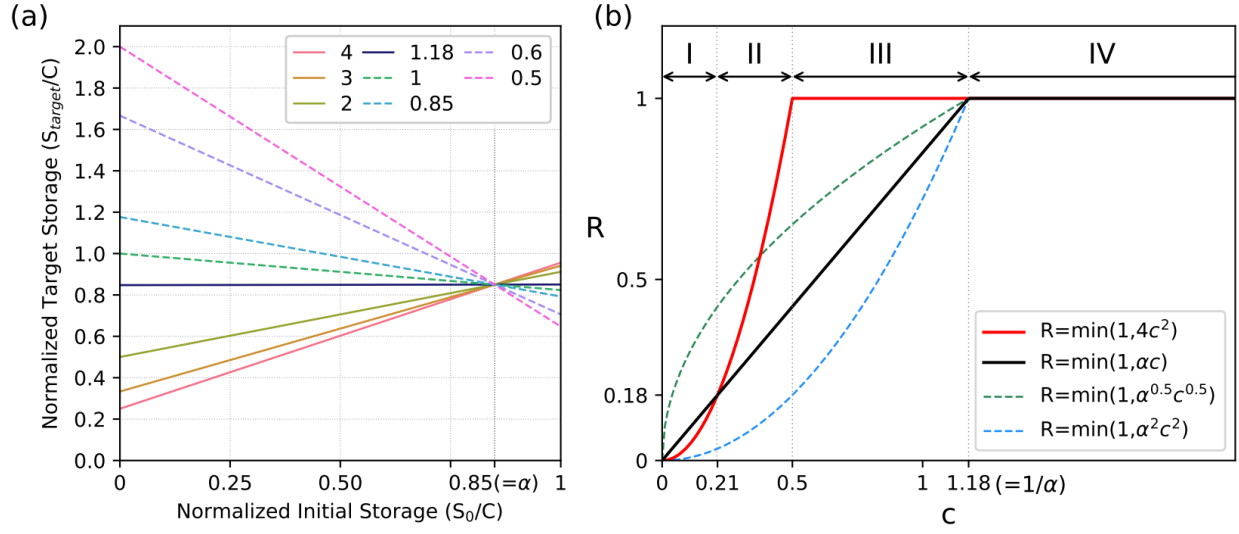


Figure 3-1 Demonstration of the need to use $R = \min(1, \alpha c)$. (a) The relationship between initial storage and target storage for varying c when R is not reduced ($R=1$), and (b) the comparison of various equations for R for four groups of c values.

Therefore, for the stability of reservoir storage, the slope term of $(1 - 1/\alpha c)$ should be positive (Figure 3-1). Otherwise, the transition between over-filling and under-filling of reservoir storage will be repeated. The unstable reservoir storage can be simulated for reservoirs having the following c value.

$$c < 1/\alpha \quad (3-13)$$

For reservoirs satisfying equation (3-13), the stability of reservoir storage simulation can be enhanced by setting the value of R to less than 1. The principle is that the portion of run-of-the-river has an effect of decreasing inflow and outflow terms in the equation (3-11) to $\overline{Ri_m} \cdot (1 \text{ year})$ and $\overline{Rk_{rls} i_m} \cdot (1 \text{ year})$, respectively. When the effect of R is considered, the slope term between initial storage and target storage can be rewritten as $(1 - R/\alpha c)$. Hence, the stability of reservoir storage simulation can be enhanced when R is set as follows.

$$R \leq \alpha c \quad (3-14)$$

Hence, the necessary condition of R for the stability of storage simulation is:

$$R = \min(1, \alpha c) \quad (3-15)$$

The reservoirs having $c < 1/\alpha$ are found to require a reduction of R as shown in the relationship between S_0 and S_{target} (Figure 3-1a). In contrast, the existing equation (i.e., $R = \min(1, 4c^2)$) reduces R values only for some of those reservoirs (i.e., $c < 0.5$), hence $R = \min(1, 4c^2)$ can result in unstable storage simulation, specifically for reservoirs having $0.5 \leq c < 1/\alpha$ (Figure 3-1a, dotted lines). For example, for a reservoir having $c = 0.5$, when the initial storage is 30% and 95% of capacity, S_{target} is set to 159% and 71% of capacity, respectively (Figure 3-1a, pink dotted line).

Among the feasible cases of reducing R , the necessary condition to ensure reservoir storage stability is when $S_0 = \alpha C = S_{\text{target}}$, which can be provided by the new equation: $R = \min(1, \alpha c)$. To effectively compare $R = \min(1, \alpha c)$ with $R = \min(1, 4c^2)$, 4 groups of c values are defined as follows: Groups I, II, III, and IV for $c < 0.21$, $0.21 < c < 0.5$, $0.5 < c < 1.18$, and $c > 1.18$, respectively (Figure 3-1b). Compared to $R = \min(1, 4c^2)$, $R = \min(1, \alpha c)$ can potentially cause a reduced stability for reservoirs having $c < 0.21$ (Group I; Figure 3b), however, those reservoirs already have more than 82% of outflow as run-of-the-river flow (i.e., a relatively small reservoir influence on flows). In addition, the difference in outflow portion of run-of-the-river flow between the old and new equations is only less than 5%. Meanwhile, the necessary condition ensures a higher stability for reservoirs having $0.21 < c < 0.5$ (Group II; Figure 3b), and newly introduces stability for reservoirs having $0.5 < c < 1.18$ which are not

covered by the original equation (Group III; Figure 3-1b). The new equation can also be compared with other univariate power functions of c , i.e., $R = \min(1, \alpha^n c^n)$, which have a shape parameter of n . The equations with $n \neq 1$ can results in an increased (when $n > 1$) or reduced (when $n < 1$) stability compared to the necessary condition (Figure 3-1b, dotted lines). In this study, to ensure a desired storage stability while satisfying the downstream demand, R is parameterized using $n = 1$.

3.2.3. The Calibration of R

$R = \min(1, \alpha c)$ provides the necessary condition for R to stabilize storage for varying α and c (see Chapter 3.2.2); however, R is not necessarily a power function or a univariate function of c because additional variables can be incorporated to define R in the form of polynomial or conditional equations. In addition, the current formulations using i_m , d_m , and R to impose seasonal variation of reservoir operation can be further improved in different ways; here we propose doing so by calibrating R . Specifically, we calibrate R for reservoirs having release and storage observations for our simulation period of 1983-2010; for other reservoirs we use a general function of $R = \min(1, \alpha c)$. The specific objectives of calibrating R are to (1) improve the simulated release and storage of individual reservoirs, (2) examine the appropriateness of newly developed equation for R , i.e., $R = \min(1, \alpha c)$, and (3) identify potential improvements on the reservoir operation scheme. The first objective is achieved by determining optimal R values, and the latter two are accomplished by comparing R values from $R = \min(1, \alpha c)$ and calibration.

Due to the interdependence between upstream and downstream reservoirs (Taeb et al., 2017), iterative model simulations are necessary for a concurrent calibration of multiple

reservoirs. Such iterative simulations involve excessive computational costs for high-resolution modeling at continental to global scales. To overcome this difficulty, we propose a calibration approach that utilizes the time series of river discharge simulated without considering dams and sequentially calibrates R from upstream to downstream. The rationale is that the inflow to a reservoir is determined by the releases from its immediate upstream reservoirs and the unregulated upstream river flows. The inflow to a reservoir having K of immediate upstream reservoirs is estimated as:

$$In(t) = \sum_{k=1}^K Out(k,t) + \left(1 - \frac{\sum_{t=1}^T \sum_{k=1}^K Out(k,t)}{\sum_{t=1}^T Q_{NAT}(t)} \right) \times Q_{NAT}(t) \quad (3-16)$$

where $In(t)$ is the inflow to the reservoir at time t , $Out(k,t)$ is the outflow of the k -th immediate upstream reservoir, $Q_{NAT}(t)$ is the river discharge from the without-dam simulation at the reservoir location and time t , K is the number of immediate upstream reservoirs, and T is the number of time steps. When $K=0$, $In(t)$ is identical to $Q_{NAT}(t)$. Using the inflow from equation (4) and the prescribed operation rule (Chapter 3), release and storage are sequentially calculated from the upstream to downstream for all reservoirs. Notably, if observed discharge (i.e., release) is available, R is calibrated to minimize Root Mean Squared Error (RMSE) of release. For reservoirs where observations are unavailable, the new equation $R = \min(1, \alpha c)$ is used to determine R . By doing so, while the entire hydrological model is not required to be iteratively run, the calibrated results of upstream reservoirs are reflected in the calibration of downstream reservoirs. To pursue the objectives enlisted above under the uncertainties in large scale

modeling, we use the entire period for the calibration to find the optimal R values that explain the given release data best rather than distinguishing the calibration and validation periods.

3.3. Experimental Settings

Altogether six simulations for **NAT** (without dams), **H06** (Hanasaki et al., 2006), **B11** (Biemans et al., 2011), **R_{old}**, **R_{new}**, and **R_{cal}** are conducted as summarized in Table 3-1. Note that all six simulations with different reservoir operation rules are conducted using the same settings for model parameters and forcing. While M can be set as a spatially varying parameter, we use it as a constant number—either 0.1 (B11) or 0.5 (H06) (see Table 3-1)—to make our results comparable to the existing schemes that used a constant M . Considering the availability of USGS water use data, simulations are conducted for the period of 1983-2010. A 20-year spinup simulation is first conducted without considering reservoirs. Further, the first two years of simulations are discarded as spinup for reservoirs, thus 26 years of results (1985-2010) are analyzed. Of the 1,889 reservoirs imported from the GRanD database for the CONUS domain, 27 reservoirs are selected for calibration (Figure 2-2a and Table 3-2), for which the long-term storage and release data are available from USGS, California Data Exchange Center, US army corps of engineers, and US Bureau of Reclamation.

Table 3-1 Summary of experimental settings

Simulation ¹	M	Criterion in equation (3-2) ²	Equation for R	Calibration of R
NAT	-	-	-	-
H06	0.5	$DPI < 0.5$	$R = \min(1, 4c^2)$	-
B11	0.1	$DPI < 0.5$	$R = \min(1, 4c^2)$	-
R _{old}	0.1	$DPI < 1 - M$	$R = \min(1, 4c^2)$	-
R _{new}	0.1	$DPI < 1 - M$	$R = \min(1, \alpha c)$	-
R _{cal}	0.1	$DPI < 1 - M$	$R = \min(1, \alpha c)$	✓

¹ NAT: without dam simulation, H06: Hanasaki et al. (2006), B11: Biemans et al. (2011)

² The criterion of H06 can also be written to $DPI < 1 - M$ since $M=0.5$

Table 3-2 The attributes of reservoirs selected for calibration (Source: GRanD database)

Groups ¹	ID ²	Reservoir Name	Dam Name	River	(Lat, Lon)	Storage Capacity (Mm ³)	Main Purpose	Data Source ³
I	310	Franklin D. Roosevelt	Grand Coulee	Columbia	(47.95, -118.98)	6395.6	Irrigation	USBR
	391	Lucky Peak Lake	Lucky Peak	Columbia	(43.53, -116.05)	378.7	Flood control	USBR
	423	Fontenelle	Fontenelle	Colorado	(42.03, -110.07)	185.6	Hydroelectricity	USBR
	884	Lake Sharpe	Big Bend Dam	Missouri	(44.04, -99.45)	2343.6	Flood control	US Army
	895	Lewis and Clark Lake	Gavins Point Dam	Missouri	(42.85, -97.49)	666.1	Flood control	US Army
II	101	Wickiup Reservoir	Wickiup Reservoir	Columbia	(43.68, -121.69)	267.0	Irrigation	USBR
	182	Folsom Lake	Folsom	Sacramento	(38.71, -121.16)	1102.7	Irrigation	CDEC
	396	Palisades	Palisades	Columbia	(43.33, -111.20)	1480.2	Irrigation	USBR
	411	American Falls	American Falls	Columbia	(42.78, -112.87)	2061.5	Irrigation	USBR
III	63	Rimrock	Tieton	Colorado	(46.66, -121.13)	244.2	Irrigation	USBR
	132	Shasta Lake	Shasta	Sacramento	(40.72, -122.42)	4890.7	Irrigation	CDEC
	148		Oroville	Sacramento	(39.54, -121.48)	4366.5	Flood control	CDEC
	370	Lake Cascade	Cascade	Columbia	(44.52, -116.05)	805.5	Irrigation	USBR
	384	Jackson Lake	Jackson Lake	Columbia	(43.86, -110.59)	1076.8	Irrigation	USBR
	394	Anderson Ranch	Anderson Ranch	Columbia	(43.36, -115.45)	521.8	Irrigation	USBR
	541	Blue Mesa	Blue Mesa	Colorado	(38.45, -107.33)	923.2	Hydroelectricity	USBR
IV	131	Clair Engle Lake	Trinity	Klamath	(40.80, -122.76)	2633.5	Irrigation	CDEC
	198	New Melones	New Melones	San Joaquin	(37.95, -120.52)	2985.0	Irrigation	CDEC
	210		Don Pedro	San Joaquin	(37.70, -120.42)	2504.0	Irrigation	CDEC
	307	Fort Peck Lake	Fort Peck Dam	Missouri	(48.00, -106.41)	23560.0	Flood control	USAC
	386	Lake Owyhee	Owyhee	Columbia	(43.64, -117.24)	881.9	Irrigation	USBR
	451	Flaming Gorge	Flaming Gorge	Colorado	(40.92, -109.42)	4336.3	Water supply	USBR
	597	Lake Powell	Glen Canyon	Colorado	(36.94, -111.49)	25070.0	Hydroelectricity	USBR
	601	Navajo	Navajo	Colorado	(36.80, -107.61)	1278.0	Irrigation	USBR
	610	Lake Mead	Hoover	Colorado	(36.02, -114.73)	36700.0	Water supply	CDEC
	753	Lake Sakakawea	Garrison Dam	Missouri	(47.51, -101.43)	30220.0	Flood control	US Army
	870	Lake Oahe	Oahe Dam	Missouri	(44.46, -100.40)	29110.0	Flood control	US Army

¹ Groups are classified by storage capacity and annual mean flow (Chapter 3).

² Global Reservoir and Dam (GRanD) Database ID

³ USBR: United States Bureau of Reclamation, CDEC: California Data Exchange Center, and US Army: United States Army Corps of Engineers

3.4. Results and Discussion

3.4.1. LHFD Model Validation for the CONUS

The main focus of Chapter 3 is on simulating reservoir storage and release, but we first briefly discuss the evaluation of river discharge simulations in the CONUS scale. Because the model has been extensively evaluated over the North America as well as the Amazon in previous studies (Fan et al., 2007; Miguez-Macho et al., 2007; Miguez-Macho & Fan, 2012a, 2012b; Y. Pokhrel et al., 2014), we revisit this briefly for annual streamflow and seasonality of flow. Overall, annual streamflow is accurately simulated in the major river basins (Figure 3-2). The seasonality of flow is also reproduced well in many large river basins, but further improvements are needed especially for small basins (Figure 3-3). Since the site-specific calibration is not conducted yet for the current version of LHFD except for the calibration of R values for 27 reservoirs, the hydrographs are expected to be improved by calibrations. The impact of reservoir operation on river flows is found to be large in some rivers (e.g., Colombia, Colorado, and Missouri rivers) and to be small in other rivers (e.g., Mississippi and Ohio rivers).

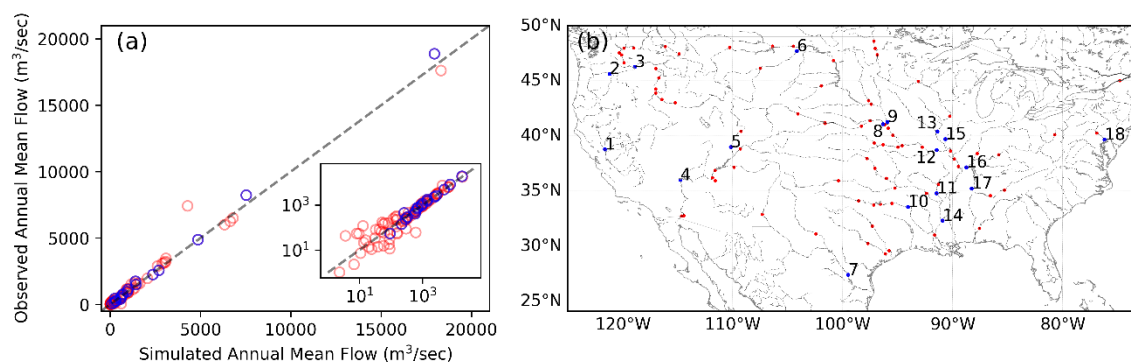


Figure 3-2 Model validation for annual mean flow over the contiguous US. (a) Comparison of simulated and observed annual mean flows averaged over the period 1983-2010 for (b) 96 USGS streamflow gauge stations. The 18 USGS stations located near the confluences (indicated in blue) are chosen to show their hydrographs in Figure 3-3. The other stations are indicated in red.

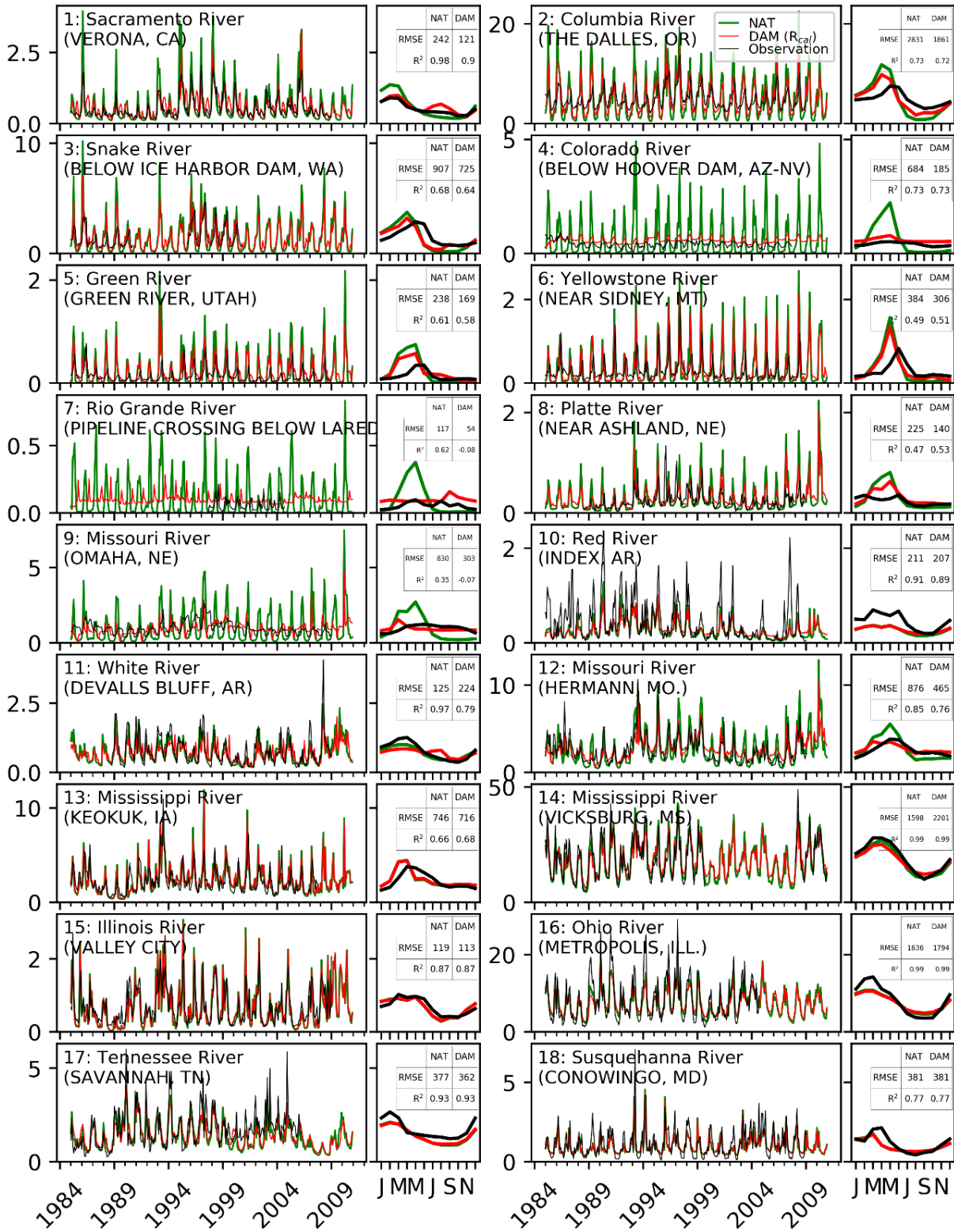


Figure 3-3 Validation of seasonal river discharge at the major gauging stations over the contiguous US (unit: $10^3 \text{ m}^3/\text{s}$). The locations of USGS gauge stations are indicated in Figure 3-2 (b).

3.4.2. Improvements in Reservoir Release and Storage

We present the evaluation of simulated reservoir release and storage from NAT, H06, B11, R_{old} , R_{new} , and R_{cal} simulations (see Table 3-1 for experiment settings) with the observed data obtained from multiple sources (see Chapter 3.3). As discussed in Chapter 3.2.2, the results of release and reservoir storage can be categorized into four groups by c values defined in Figure 3-1. Hence, among 27 reservoirs selected for calibration of R , we present the evaluation for six reservoirs, which are located in different geographic regions (i.e., Columbia, Colorado, San Joaquin, Sacramento, and Missouri river basins) and provide a good coverage of different groups (i.e., Groups I, II, III, IV), in Figure 3-4 with a summary of performance measures in terms of correlation and Root Mean Square Error (RMSE) in Table 3-3. The results for additional reservoirs are provided in Figure 3-5.

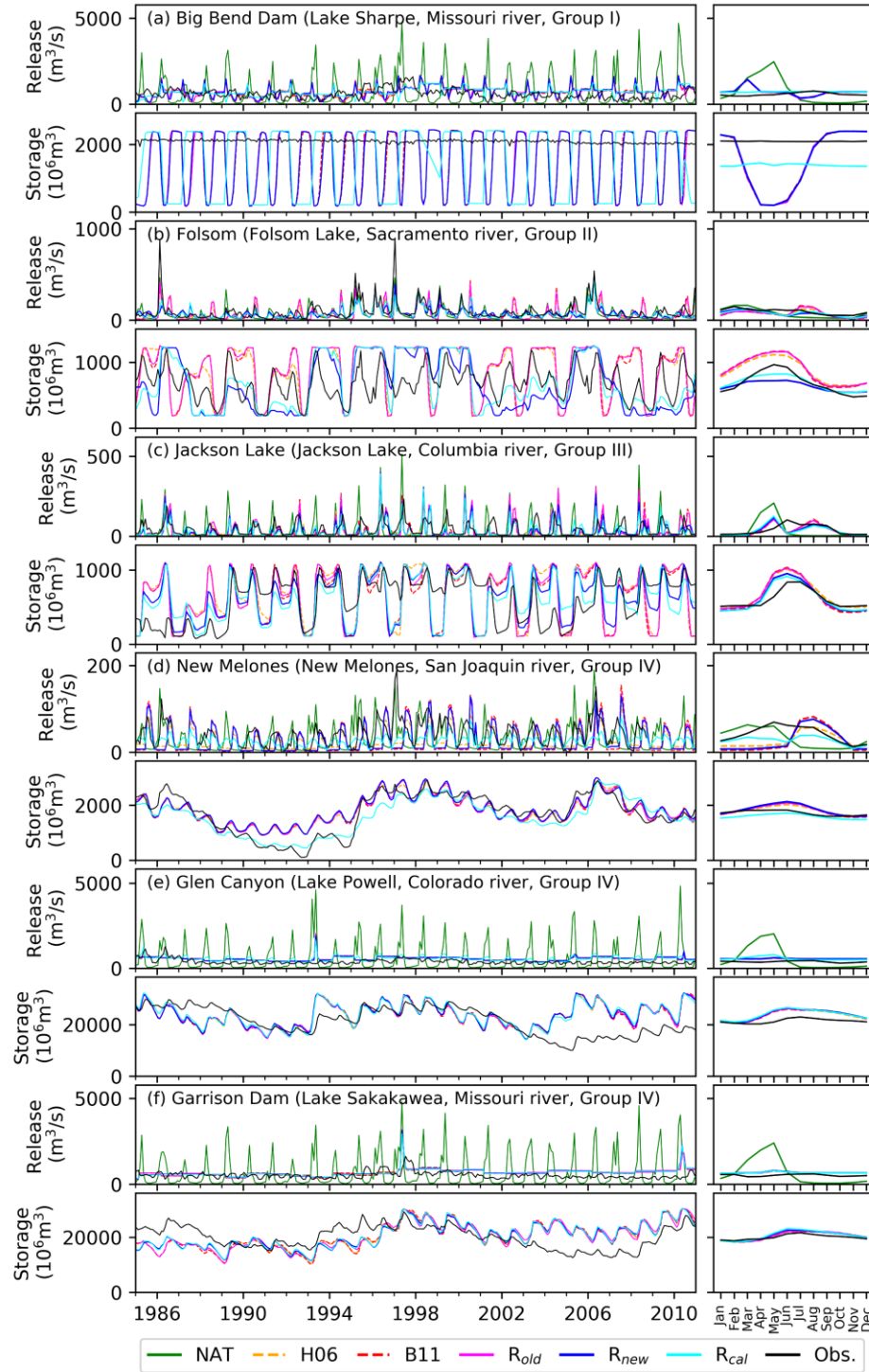


Figure 3-4 Evaluation of simulated release and storage for the six selected reservoirs in the Columbia, Colorado, San Joaquin, Sacramento, and Missouri river basins. NAT, H06, B11, R_{old} , R_{new} , and R_{cal} denote different simulation settings (Chapter 3.3). The panels on the right show the seasonal cycle.

Table 3-3 Summary of performance measures for different simulations

River flow (Reservoir Release)							Reservoir Storage					
NAT		H06	B11	R _{old}	R _{new}	R _{cal}	H06		B11	R _{old}	R _{new}	R _{cal}
(a) Big Bend Dam (Lake Sharpe, Missouri river, Group I)												
R-value	-	0.04	0.04	0.04	0.08	1.00	R-value	0.04	0.04	0.04	0.08	1.00
CORR ¹	-0.11	-0.05	-0.05	-0.05	-0.07	0.10	CORR	-0.02	-0.03	-0.02	-0.02	0.07
RMSE ²	1040	461	464	455	460	378	RMSE	1087	1085	1086	1079	1216
(b) Folsom (Folsom Lake, Sacramento river, Group II)												
R-value	-	0.96	0.96	0.96	0.42	0.56	R-value	0.96	0.96	0.96	0.42	0.56
CORR	0.77	0.64	0.58	0.59	0.63	0.61	CORR	0.45	0.42	0.42	0.47	0.49
RMSE	69	83	91	90	84	85	RMSE	399	416	417	359	337
(c) Jackson Lake (Jackson Lake, Columbia river, Group III)												
R-value	-	1.00	1.00	1.00	0.80	0.70	R-value	1.00	1.00	1.00	0.80	0.70
CORR	0.03	0.26	0.29	0.28	0.31	0.31	CORR	0.32	0.33	0.33	0.45	0.48
RMSE	87	61	64	65	56	52	RMSE	398	386	392	322	299
(d) New Melones (New Melones, San Joaquin river, Group IV)												
R-value	-	1.00	1.00	1.00	1.00	0.50		1.00	1.00	1.00	1.00	0.50
CORR	0.34	0.30	0.25	0.26	0.27	0.40	CORR	0.87	0.86	0.86	0.86	0.89
RMSE	37	34	42	39	39	30	RMSE	383	394	391	401	345
(e) Glen Canyon (Lake Powell, Colorado river, Group IV)												
R-value	-	1.00	1.00	1.00	1.00	0.87		1.00	1.00	1.00	1.00	0.87
CORR	-0.01	0.24	0.25	0.23	0.23	0.25	CORR	0.23	0.24	0.23	0.22	0.29
RMSE	889	239	239	243	244	253	RMSE	6438	6420	6476	6532	6322
(f) Garrison Dam (Lake Sakakawea, Missouri river, Group IV)												
R-value	-	1.00	1.00	1.00	1.00	1.00	R-value	1.00	1.00	1.00	1.00	1.00
CORR	-0.05	0.22	0.21	0.22	0.20	0.21	CORR	0.28	0.27	0.26	0.26	0.26
RMSE	982	303	304	305	311	303	RMSE	5302	5339	5318	5215	5197

¹Correlation²Root Mean Square Error

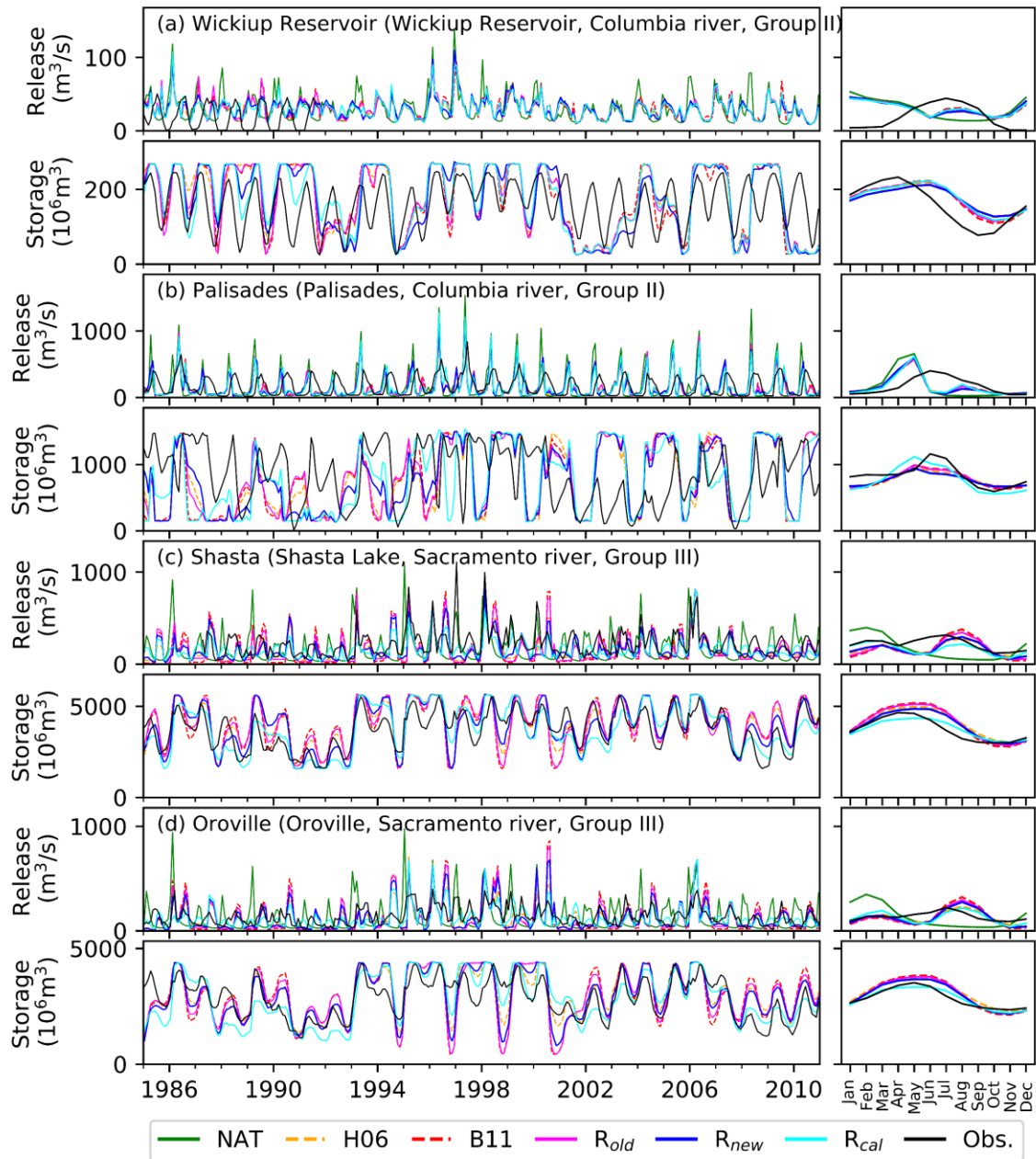


Figure 3-5 Same as in Figure 3-4 but for additional reservoirs

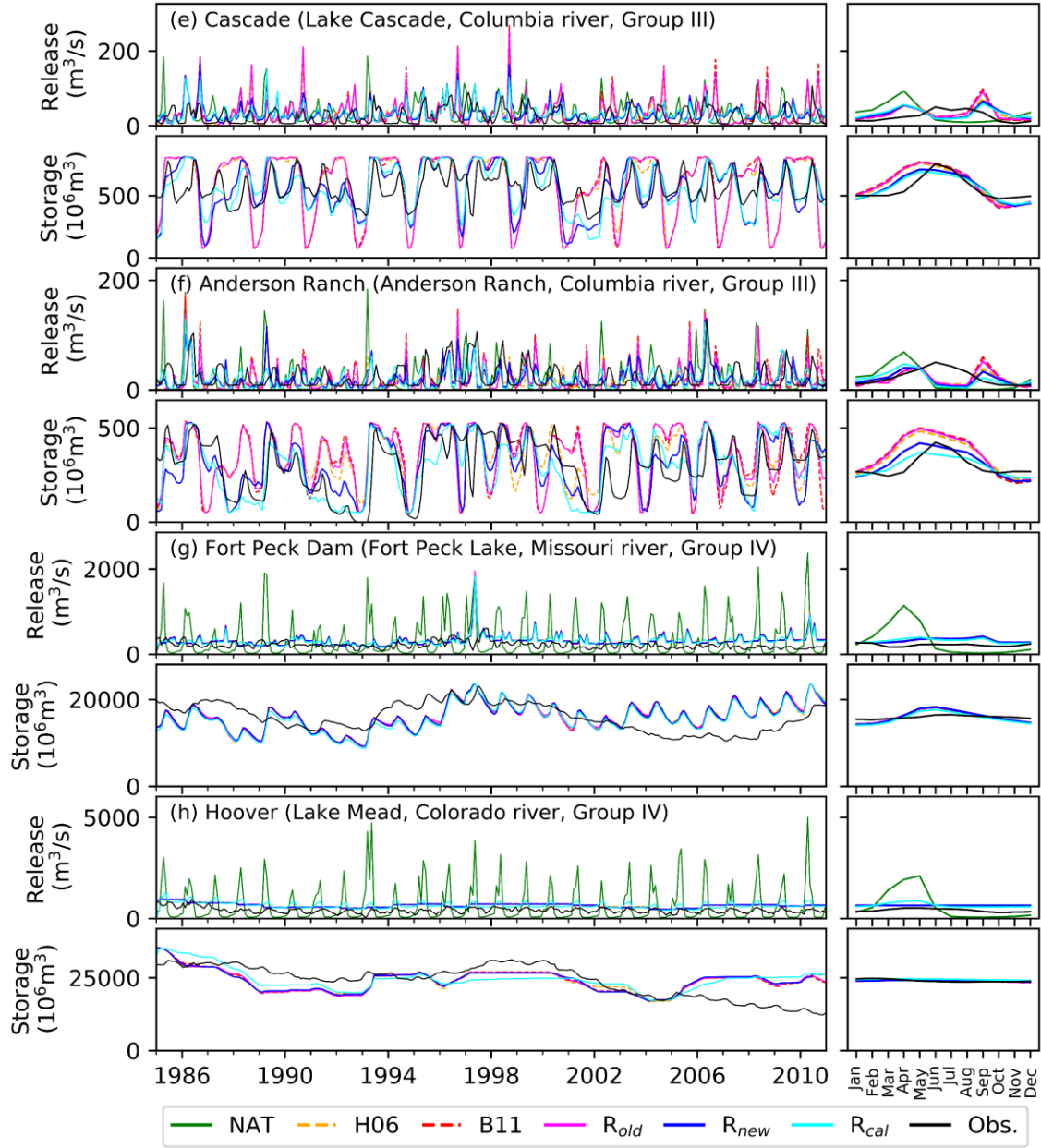


Figure 3-5 (continued)

Results of individual reservoir release and storage suggest that (1) the large seasonal variation of river flow in the simulation without reservoirs is damped by the inclusion of reservoirs (comparison of NAT and others), (2) the new criterion in equation (3-2) (i.e., $DPI > 1 - M$) prevents excessive release in high-demand season (comparison of B11, R_{old} , R_{new} , and R_{cal}), (3) the use of new equation of R mitigates the issues of storage depletion, particularly for

reservoirs in Groups II and III (comparison of H06, B11, R_{old} , R_{new} , and R_{cal}), (4) the proper adjustment of R value improves seasonal dynamics of the release and/or storage in most cases (comparison of all simulations), and (5) all reservoir schemes are found to exhibit poor performance for small reservoirs (Group I), suggesting the need of further improvements (comparison of all).

As the relative size of storage capacity to mean flow (i.e., c) increases (i.e., a transition from Group I toward Group IV in Figure 3-1b), the reduction in peak becomes more pronounced as the reservoirs can retain a large portion of the excess inflow during wet season and release it later during drying seasons (Figure 3-4def). On the contrary, for reservoirs having small c (e.g., Figure 3-4abc), the magnitude of variability in release may not decrease as substantially since the excessive inflows easily fill the reservoir storages up to their capacities, beyond which the remainder is released as spillway overflow. When c is very small (i.e., Group I), adjusting R may not necessarily influence reservoir storage stabilization (Figure 3-4a). However, with moderate c values (i.e., Groups II and III), reducing R becomes crucial, and the use of new equation for R effectively enhances the release and storage simulations (Figure 3-4bc). Specifically, for the reservoirs in Group III, the equation for R from H06 (i.e., $R = \min(1, 4c^2)$) always sets $R=1$, and hence the amplified release patterns and the consequent over- and under-filling storage patterns are simulated due to the periodic excessive inflows (Figure 3-4c). Similarly, the overestimated R values by $R = \min(1, 4c^2)$ for reservoirs in Group II can also have frequent over- and under-filling storage patterns (Figure 3-4b). After the proper adjustment of R value by using the newly proposed equation (i.e., $R = \min(1, \alpha c)$), the issues of amplified release and unstable storage are mitigated, and the releases and storages of reservoirs in Groups II and III are significantly

improved (Figure 3-4bc). The comparable R values from $R = \min(1, \alpha c)$ (i.e., R_{new}) and the calibration (i.e., R_{cal}) demonstrate the appropriateness of new equation, specifically for reservoirs in Groups II and III.

3.4.3. The Role of R in Release and Storage Simulations

The R values of the reservoirs in Group IV (e.g., New Melones, Lake Powell, and Lake Sakakawea; Figure 3-4def) are calculated to be 1 by both $R = \min(1, 4c^2)$ and $R = \min(1, \alpha c)$ equations. Consequently, many reservoirs in Group IV show similar storage-release patterns for H06, B11, R_{old} , and R_{new} simulations. For R_{cal} simulation, depending on the calibration effect, the magnitudes of changes in release and storage can vary substantially. For example, the release and storage of New Melones (Figure 3-4d) with $R=1$ and $R=0.5$, before and after calibration, respectively, show significantly different trends and patterns. Meanwhile, the calibrated R for Lake Powell (Figure 3-4e) is rather high (i.e., $R=0.87$; Table 3-3), which imposes a relatively small interannual seasonality in release. Further, for Lake Sakakawea (Figure 3-4f), calibration yields $R=1$ (i.e., identical to that from both old and new equations), making the changes in release and storage insignificant. However, the release and storage for New Melones are significantly improved when R is calibrated, demonstrating that results could be potentially improved by further improving the R equation which is currently a univariate power function of c . As shown for Lake Sakakawea, certain advancements beyond improving R could also be necessary since seasonal variation in natural and actual release can differ from each other.

Distinct results are derived from the calibration of R for cascade of reservoirs such as the Lake Sharpe (Figure 3-4a) located in the main stem of Missouri river that has three large upstream reservoirs: Lake Oahe, Lake Sakakawea (Figure 3-4f), and Fort Peck Lake. Due to high

\bar{i}_m of main river stem and small C , the R value of Lake Sharpe is set to 0.04 and 0.08 by $R = \min(1, 4c^2)$ and $R = \min(1, \alpha c)$ equations, respectively. With an uncalibrated (small) R , r_m is determined to be similar to i_m (Figure 3-4a, green line in right panel) which results in a highly variable release patterns in H06, B11, R_{old} , and R_{new} simulations; for example, the maximum amount of monthly target release (i.e., $\max(r_m) \times (1\text{-month})$) is ~ 3 times of storage capacity that inevitably causes an oscillating storage simulation. Conversely, the calibration of R reflects the steady patterns of observed release and storage (Figure 5a, black lines) to determine r_m ; r_m is determined to be steady when R is set to 1 (by calibration) and d_m is small (as given). In R_{cal} simulation, the inflow to Lake Sharpe is simulated to be steady except for the peaks during 1997-1998 due to the large upstream reservoirs in cascade (see Figure 3-4f). While the oscillation is not entirely eliminated despite steady r_m and stable inflow, its frequency is reduced. It is noteworthy to recall that the reservoirs having low c (i.e., Group I) hardly recover the storage stability once S_0 deviates significantly from αC (see discussions in Chapter 3.2.2). In addition, the calibration increases R (i.e., boosting the instability) instead of decreasing it. Since the current simulations start from natural river storages with small S_0 for the 1st operational year, S_{target} is overestimated and results in large S_0 for the 2nd year; S_{target} for the 2nd year is underestimated that results in small S_0 for the 3rd year and vice versa. Even if S_0 is set exactly equal to αC , a given and several consequent operation years will have steady reservoir storage at most, but even with small changes in year-to-year inflow from the upstream (Figure 3-4f) or occasional large inflows (e.g., flooding pulses during 1997-1998) reservoir storage can readily begin to oscillate.

Even if the inter-annual inflow is stable and a steady intra-annual release is planned to Lake Sharpe in R_{cal} simulation, storage is not stabilized even after 28 years. Based on the reasoning above, the reservoir storage of Lake Sharpe will remain unstable regardless of an extended simulation period. Considering a common rationale in hydrological modeling that extended model runs with steady input will result in equilibrium states, the results of Lake Sharpe are counter-intuitive. Such modeling issues have not been explored in previous studies because their focus has been on reproducing the large-scale patterns, especially of reservoir release. When the grid resolution is increased and smaller reservoirs are considered, the issues encountered in Lake Sharpe can unintentionally and ubiquitously spread over a large domain, which can adversely affect the magnitude and timing of simulated surface water fluxes and cannot be addressed by an extended spinup. This calls for caution in using the proposed scheme when applied for small reservoirs, and the need for further improvements by developing generic reservoir operation rule that can provide potentially stable results for small reservoirs and through incorporation of reservoir-specific operation rules.

3.4.4. Stability of Reservoir Simulation over the CONUS

As discussed above, the stability of reservoir storage is significantly improved in the enhanced scheme, but the stability varies largely among reservoirs in the four different groups. The improvements in stability are examined by using a frequency analysis for over-filled and under-filled days for all 1,889 reservoirs (Figure 3-6). Over-filled and under-filled days are defined as days when a reservoir storage is $>95\%$ of the maximum capacity and $<105\%$ of the minimum storage, respectively. While overfilling and under-filling can happen in real-world operation, too frequent occurrences in simulations arise from the deficiencies in reservoir release parameterizations described in Chapter 3.2.2. When the over-filled and under-filled days of H06,

B11, and R_{old} are compared for each group of reservoirs using Kruskal-Wallis H test ($\alpha=0.05$), none of the groups shows statistically significant differences for both over-filled and under-filled days. When H06, B11, R_{old} , R_{new} , and R_{cal} are tested, statistically significant differences are found for the over-filled days in group II ($p=1e-7$) and group III ($p=5e-17$) and for the under-filled days in group III ($p=2e-5$). From the results of decreasing quantiles and average of over-filled and under-filled days, it is concluded that the new reservoir operation scheme mitigates the problem of unstable reservoir storage simulation, especially for reservoirs in Groups II and III. In terms of enhancing the storage stability, the contribution of the new R equation (i.e., $R = \min(1, \alpha c)$) (compared to R_{old} and R_{new}) is found to be larger than the contribution of the new criterion of equation (3-2) (i.e., $DPI < 1-M$) (in comparison of H06, B11, and R_{old}). The reservoirs in Group I and Group IV are less influenced by different reservoir operation schemes due to inherent and large variability (as discussed with Lake Sharpe in Figure 3-4a) and the identical $R=1$ values, respectively.

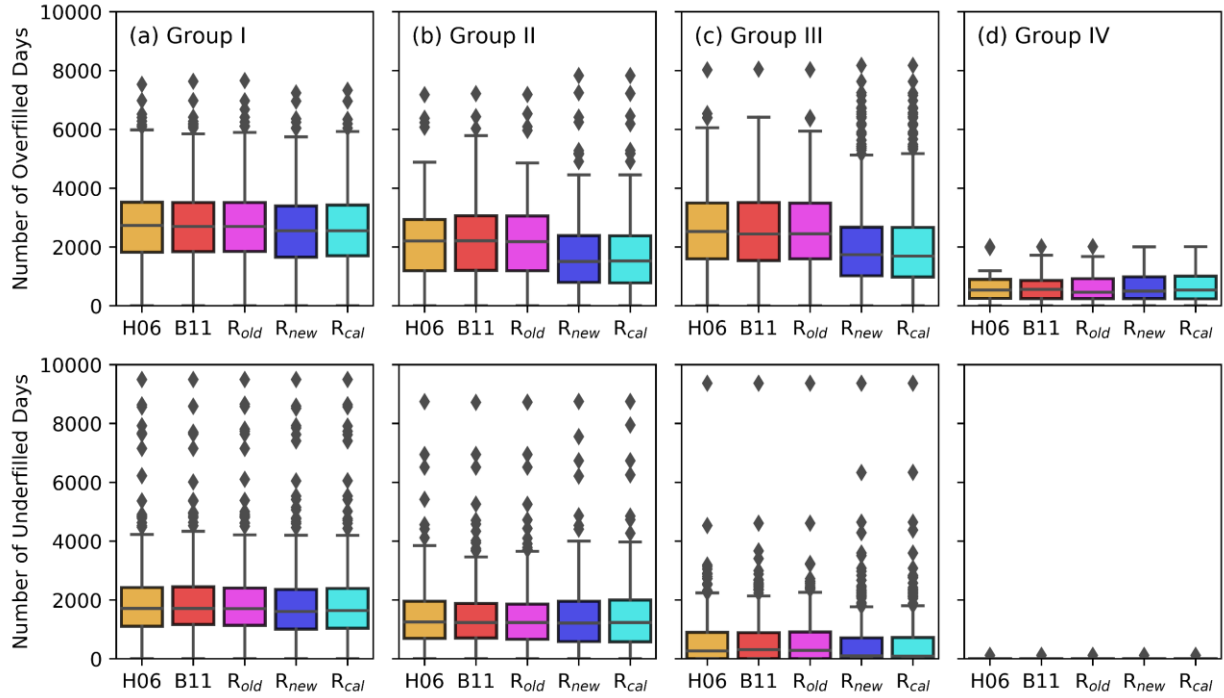


Figure 3-6 Boxplot showing stability of simulated reservoir storages for 1,889 GRanD reservoirs estimated from frequency analysis for the occurrence of (a) overfilling and (b) underfilling.

3.4.5. Flow Regime Change due to Reservoirs

Finally, we examine the effects of reservoir operation on river flows having different exceedance probabilities to ensure that the reservoir-induced changes in extreme flows are well simulated over the entire CONUS domain. Figure 3-7 presents the difference between Q_{DAM} (R_{cal} simulation) and Q_{NAT} (NAT simulation) presented as percentage change relative to Q_{NAT} for exceedance probabilities of 90% (low flow; Q_{90}), 50% (median flow; Q_{50}), and 10% (high flow; Q_{10}) (Figure 3-7). Expectedly, the Q_{90} is increased and Q_{10} is decreased in much of the study domain (Figures 3-7a and 3-7c). Further, an increase in the median flow can be seen in most regions (Figure 3-7b). Meanwhile, sporadic decreases in Q_{90} and Q_{50} and increase in Q_{10} can also be seen, similar to that found in previous studies that examined the impacts of dams on extreme flows. This is likely due to the following two reasons. First, frequent over- and under-filling of

relatively small reservoirs (Figure 3-6) potentially cause a reduction in low flow and an increase in high flow as can be seen in the lower portion of the Mississippi river basin where there are large number of such small reservoirs. Second, in the river-floodplain parameterizations in LHF model, the channel geometry and elevations of tributaries are sensitive to the water level in the main stem of the river, which can cause a magnified flow pattern in the tributaries, especially when flows are modified through reservoir regulation. For example, if river-reservoir bed elevations of tributaries are parameterized to be rather flat, when the water level at the main stem, which acts as the lower boundary condition for tributaries, is modified by reservoir operation, the variability of flow and water level in the tributary could increase. Despite some unintended outcomes due to the interference between river-floodplain and reservoir parameterizations, the overall patterns of increased low flow and decreased high flows are reproduced by the model. This is particularly true for large rivers having reservoirs with large storage capacity.

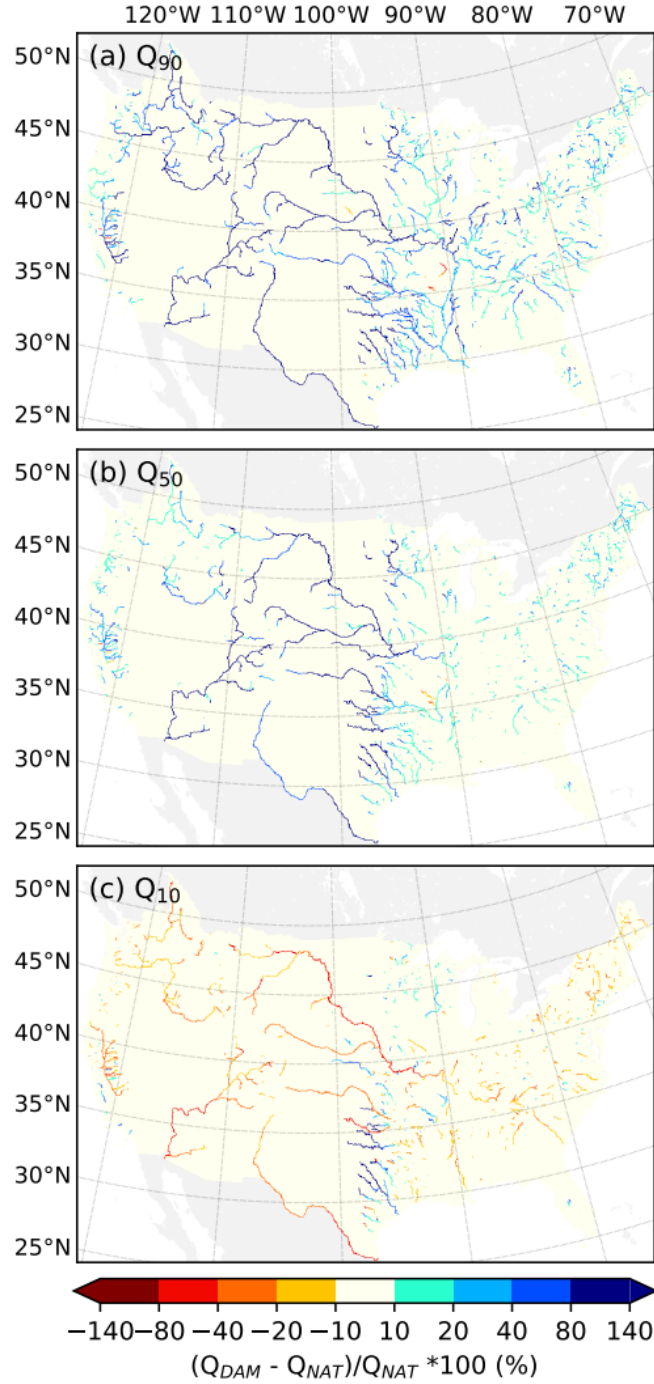


Figure 3-7 Effect of reservoir operation on long-term average daily river discharge with the exceedance probability of (a) 90% (low flow; Q_{90}), (b) 50% (median flow; Q_{50}), and (c) 10% (high flow; Q_{10}), shown as relative change between Q_{DAM} (i.e., R_{cal}) and Q_{NAT} (i.e., NAT simulation). To avoid overly exaggerated relative change, results for grid cells having very small river discharge (i.e., $Q_{99} < 1 \text{ m}^3/\text{sec}$) are represented to have $\pm 10\%$ change (light yellow color).

3.5. Summary and Conclusion

The temporal dynamics of reservoir storage and release is improved by a novel parameterization that enables stabilized storage and release simulations and by employing a computationally-efficient calibration method that does not require iterative reservoir simulations over the entire domain. Simulated results of reservoir release and storage for the selected reservoirs are evaluated with observations, and the importance of resolving certain unintended behaviors in the previously used reservoir operation schemes is discussed. The proposed model improvements result in a better simulation of the seasonal dynamics of reservoir storage; however, further improvements are needed to account for diverse features of real-world reservoir operation rules. From the calibration of R , the limitations of generic reservoir operation rules that imposing release seasonality using demand seasonality are identified, and the potential further improvements on the formulation of R are found. Specifically, further improvements are necessary to enhance simulation stability for small reservoirs (i.e., Group I) and better simulate the seasonality in storage and release for large reservoirs (i.e., Group IV). In addition, the unintended effects of reservoir operation on extreme flows due to main stem-tributary interference in regions with small reservoirs could be improved by enhancing the proposed reservoir release scheme. There are many other important issues in reservoir modeling which should be addressed in the following studies. For example, a novel approach is needed to implement the optimal operation of multi-objective cascade reservoirs (e.g., Huang et al., 2002; Yang et al., 2017) in large-scale models against the “curse of dimensionality” (Bellman, 1961; Labadie, 2004) and high uncertainties. Future studies should also consider incorporating long-distance water transfer from reservoirs, which can be a significant water balance component in

some regions and has been increasingly discussed in recent literature (Hanasaki et al., 2018; Y. Pokhrel et al., 2016; Wada et al., 2017).

Chapter 4. Sensitivity Analysis for the Effect of Upstream Flow Regulation on Flood Dynamics in the Lower Mekong River Basin and Tonle Sap Lake

4.1. Introduction

In Chapter 4, the questions of “*Q3. What are the implications of potential flow regulation by new dams on downstream flood inundation dynamics?*” is answered by examining different scenarios of flow regulation designed by altering the magnitude and timing of flood pulse near Stung Treng, a location in the vicinity of the proposed site for the massive Sambor dam with 18km barrier, which, if built, is feared to severely fragment the river dolphin population and block fish migration (Brownell et al., 2017; Fawthrop, 2018). This approach is novel in that we use the altered flow patterns over scenarios of flow regulation by the existing and planned dams because the existing dams have caused little hydrologic alterations in mainstream flows (Arias, Piman, et al., 2014), and the number, construction time, and size of dams to be built remains highly uncertain. It is noted that the flow alteration patterns in Chapter 4 are not designed to perfectly capture the actual flow regulation by any specific future dam but to provide a framework for sensitivity analysis under different degree of flow regulation by a single of multiple dams in the upstream of the location where we alter the flows. Further, while future dams could be operated for different purposes, our analysis is based on flow regulation patterns of hydropower and flood control dams whereby a reduced flood peak is accompanied by an increased low flow. Thus, the approach enables a mechanistic understanding of the changes in downstream flooding under different levels of potential flow regulation by any upstream dams. Further, while previous studies have mostly focused on the TSL, a relatively complete picture of flood dynamics and its consequent TWS variations across the entire MRB is provided. By doing

so, the question of “*Q4. What role does the flood dynamics play in modulating the overall hydrology of the basin?*” is also addressed.

4.2. Materials and Methods

4.2.1. HiGW-MAT

HiGW-MAT (Y. Pokhrel et al., 2015) is a global hydrological model based on the global land surface model (LSM) MATSIRO (Takata et al., 2003) coupled with the river routing model TRIP (Taikan Oki & Sud, 1998). HiGW-MAT simulates both the natural water cycle and human activities such as irrigation, flow regulation, and groundwater pumping, but the human impact schemes are turned off because the objective here is to examine the effects of potential flow regulation by future dams, not limited to the existing ones; note that the existing dams have caused little impact on the Mekong flow (Arias, Piman, et al., 2014). MATSIRO simulates key vegetation, surface hydrological, soil moisture, and groundwater processes on a full physical basis. A complete description can be found in Takata et al. (2003), with further details on its recent improvements in the studies of Pokhrel and coauthors (Y. Pokhrel et al., 2015, 2016; Y. Pokhrel, Hanasaki, Koirala, et al., 2012).

4.2.2. CaMa-Flood

CaMa-Flood (D. Yamazaki et al., 2011, 2014) is a hydrodynamic model, which computes river hydrodynamics (i.e., river discharge, flow velocity, water level, and inundated area) by solving shallow water equation of open channel flow, explicitly accounting for backwater effects using the local inertial approximation (D. Yamazaki et al., 2013). The physics of CaMa-Flood is similar to the river-floodplain routing module of LHF (see Chapter 2.2.1). In this chapter, CaMa-Flood version-3.6 is used with regional settings at 10km resolution for the MRB (D. Yamazaki et al., 2014), which includes the capability for downscaling output to 500m grids; version-3.6 accounts for channel bifurcation, a critically important process to realistically simulate river-floodplain dynamics in the Mekong Delta. In CaMa-Flood, water level and inundated areas are

diagnosed from water storage in each unit catchment; river discharge from each unit catchment is calculated using the shallow water equation; water storage at each unit catchment is updated by a mass conservation equation considering discharge input from the upstream unit catchment(s), discharge output to the downstream unit catchment, and local runoff input from HiGW-MAT. The 10km river network map is generated by upscaling the 3 arc-second (90m) HydroSHEDS flow direction map (Lehner et al., 2008) and digital elevation model from SRTM3 DEM (D. Yamazaki et al., 2014). Manning's roughness coefficient for rivers and floodplains is set basin wide at 0.03 and 0.10, respectively, following Yamazaki et al. (2011, 2012, 2014); sensitivity of the coefficient to model results is discussed in Yamazaki et al. (2011). All other model parameters including river width are identical to those in Yamazaki et al. (2014).

4.2.3. Simulation Settings

First, the HiGW-MAT model is used to simulate runoff and all TWS components (i.e., soil moisture, snow, river storage, and groundwater) for 1979-2010 period using identical settings, parameters, and forcing data as in Pokhrel et al. (2015); the first two years are discarded as spinup; results for 1981-2010 are analyzed. Since HiGW-MAT is a global model, results for the MRB (90-110°E, 5-35°N) are extracted from global simulations at 1°×1° grids. Runoff is used to drive the CaMa-Flood model and the storage components are used for TWS analysis. Note that the HiGW-MAT is used for a single simulation without considering flow alterations.

Then, similarly to the previous studies (D. Yamazaki et al., 2014; F. Zhao et al., 2017), daily runoff from HiGW-MAT is used in CaMa-Flood to simulate river-floodplain hydrodynamics at 10km over the MRB. The 10km resolution flood depth is then downscaled to 500m grids using SRTM3 high-resolution DEM assuming that the water levels of 500m grids

within a 10km grid is identical (D. Yamazaki et al., 2014). A series of simulations are conducted for: (1) 1981-2010 period using continuous HiGW-MAT runoff and with no flow alterations; (2) an average year, using the climatological mean daily runoff for 1981-2010 period; (3) a historical dry year (1998); and (4) a historical wet year (2000). For (2), (3), and (4), a baseline simulation is firstly conducted without flow alterations. Then, simulations with different degree of dampened flood peak (i.e., by 10, 20, 30, 40, and 50%) and early and delayed arrival of the peak by one month (see details below) are conducted.

Table 4-1 Geographic location of stations in MRB

Station	Name	Latitude	Longitude	Classification
LP	Luang Prabang	19.89	102.14	Mainstream Mekong
PA	Pakse	15.12	105.80	Mainstream Mekong
ST	Stung Treng	13.53	105.95	Mainstream Mekong
Dam	Dam	13.55	105.95	Mainstream Mekong
KT	Kratie	12.49	106.02	Mainstream Mekong
KC	Kampong Cham	12.00	105.47	Mainstream Mekong
KL	Kompong Luong	12.58	104.22	Tonle Sap River
LO	Lake Outlet	12.52	104.47	Tonle Sap River
PK	Prek Kdam	11.81	104.80	Tonle Sap River
PP	Phnom Penh Port	11.58	104.92	Mainstream Mekong
NL	Neak Luong	11.26	105.28	Mainstream Mekong
KK	Koh Khel	11.27	105.02	Bassac River
CD	Chau Doc	10.70	105.13	Bassac River
VN	Vam Nao	10.58	105.36	Mainstream Mekong
MTu	My Thuan	10.27	105.92	Mekong Delta
MTo	My Tho	10.36	106.37	Mekong Delta
CT	Can Tho	10.03	105.79	Bassac River/Song Hau

To generate the altered flood pulse patterns as a surrogate of flow regulations by future dams, we change the timing and magnitude of flood peak near Stung Treng gauging station (13.53°N, 105.95°E; Table 4-1) in the Mekong river, immediate downstream of the confluence of the 3S river systems, a location near the proposed site for the massive Sambor dam (Fawthrop, 2018). This approach enables us to mechanistically examine the changes in flood magnitude,

timing, duration, and extent under different levels of dam regulations or altered flow patterns due to climate change. Although the majority of the proposed large dams are likely to be used for hydropower generation, no information is available on how these dams will be operated. However, as most dams do, the new dams will alter the magnitude and timing of river flow by attenuating the peak and increasing low flow. Thus, to capture these altered flow patterns, we generate a proxy of dam release using a release equation modified from the reservoir operation rule proposed in Chapter 3, which can be written as:

$$Q_{i,DAM} = Q_{mean} \times \left(M + (1-M) \frac{Q_{i,NAT}}{Q_{mean}} \right) \quad (4-1)$$

Where, $Q_{i,DAM}$ is the altered flow, $Q_{i,NAT}$ is the simulated natural flow at the dam location, and Q_{mean} is the mean annual natural flow for each operational year. M is a calibration parameter that determines the release; e.g., when M is unity, the equation represents a constant release throughout the year, and when M is zero, release is equal to the natural flow, representing no reservoir effect. Here, we calibrate M to attenuate peak by 10, 20, 30, 40, and 50% from the baseline (i.e., average year) flow. Because Q_{mean} is different for each year, M values are differently calibrated among years, i.e., average (1981-2010 mean), dry (1998), and wet (2000), to maintain the same degree of peak flow attenuation. Once Q_{mean} and M are determined, $Q_{i,DAM}$ is generated using equation (4-1) that produces enhanced low-flow to compensate for peak flow reduction, preserving water balance. For the scenarios with altered timing of peak, $Q_{i,DAM}$ is derived by shifting the peak of the hydrograph one month earlier or later. Note that the scenarios of altered timing are analyzed only for 10, 30, and 50% peak flow attenuation scenarios.

These scenarios are designed to reflect the compounded impacts of flow regulation and climate change to flood dynamics under the uncertainties in climate change as well as in number,

specifications, and operation rules of future dams. Here, the reduction in magnitude and a delay in timing of the flood peak are typically caused by hydropower and flood-control dams. The timing of peaks can change as timings of precipitation and snow melting are altered under climate change. While these scenarios may not capture the actual flow regulations by future dams, they represent the plausible scenarios of the cumulative effects of upstream dams, similar to those observed in other large river basins such as the Colorado (Y. Pokhrel et al., 2016), and also climate changes on flow regime. Hence, this approach enables a mechanistic understanding of the changes in flood dynamics in the LMRB including Mekong Delta region by different levels of flow regulations under climate change.

4.2.4. Terrestrial Water Storage (TWS) and its Estimation

TWS is composed of water stored over and underneath the land surface; thus, it is estimated by vertically integrating snow water, canopy water, river and floodplain water, soil water, and groundwater storages over a given spatial domain, typically a river basin. Mathematically, this can be expressed as (Y. Pokhrel et al., 2013):

$$\begin{aligned}
 \text{TWS} &= \text{Surface water} + \text{Subsurface water} \\
 \text{Surface water} &= \text{FW} + \text{RW} + \text{SW} + \text{CW} \\
 \text{Subsurface water} &= \text{VW} + \text{GW}
 \end{aligned} \tag{4-2}$$

Where,

- FW = water on the floodplains
- RW = water in the river channels
- SW = snow water
- CW = water stored in canopy surfaces
- VW = soil water in the vadose zone (unsaturated store)
- GW = groundwater (below the water table, saturated store)

The TWS derived from the measurements made by the Gravity Recovery and Climate Experiment (GRACE) satellite mission (Tapley, 2004) provides the vertically-integrated TWS and thus includes all components listed in Equation (4-2). In hydrological models such as

HiGW-MAT, however, each of the components is typically simulated on an individual basis. Thus, vertically integrated TWS for comparison with GRACE-based TWS is estimated by adding all components using Equation (4-2).

Because GRACE measures the TWS variations over large regions, the GRACE data and model results are typically compared as basin averages (Felfelani et al., 2017; Y. Pokhrel et al., 2013; Syed et al., 2009) over river basins having an area larger than the GRACE footprint of ~200,000 km² (Yeh et al., 2006). In the present study, we estimate the basin-averaged TWS from both GRACE and HiGW-MAT model by taking an area-weighted average:

$$H(x, t) = \frac{\sum_{i=1}^n S_i(x, t)}{A}, \quad S_i(x) = \begin{cases} 1 \times s \times a_i & \text{inside the basin} \\ 0 & \text{outside the basin} \end{cases} \quad (4-3)$$

where s is the LSM or GRACE estimate, a_i is the cell area, S_i is the weighted estimate for each cell inside the basin, n is the number of cells in a basin, A is the total area of the basin, and $H(x, t)$ represents the estimate of water storage for basin at time t .

Following Felfelani et al. (2017), simulated TWS components from HiGW-MAT are vertically integrated to derive TWS anomalies averaged over the MRB for 2002-2010 period, an overlapping period between GRACE and simulations. Two sets of basin-averaged TWS are derived from the model results. In the first set, the flood water (FW) component in Equation (4-1) doesn't exist because river-floodplain storage is lumped in the river water (RW) component of the TRIP routing model used in HiGW-MAT. Then, another set of TWS time series is derived by replacing the river storage in HiGW-MAT-based TWS by FW based on the explicit simulation by the CaMa-Flood model without altering the other TWS components. The two sets of TWS are then compared with the TWS from GRACE to examine the role of river-floodplain storage in modulating TWS variations. Note that the river storage in HiGW-MAT and river-floodplain

storage in CaMa-Flood are simulated using the same runoff from HiGW-MAT, thus the mass balance in TWS computations is preserved. The component contribution of river-floodplain water to the total TWS is calculated as the ratio of seasonal amplitude of river-floodplain storage to the seasonal amplitude in the simulated total TWS (Y. Pokhrel et al., 2013). For uniformity, CaMa-Flood results at 10km grids are first upscaled to the grid resolution of GRACE data and HiGW-MAT model (i.e., 1°).

4.2.5. Data

Historical observations of river discharge and water level are obtained from the MRC. For the analysis of TWS variations, we use both the Spherical Harmonics (SH) and mascon-based GRACE products. The level-3 SH-based products are obtained from three processing centers: (i) the Center for Space Research (CSR), (ii) the Jet Propulsion Laboratory (JPL), and (iii) the German Research Center for Geoscience (GFZ), available at: <https://grace.jpl.nasa.gov/data/get-data/>. The mascon products are obtained from Scanlon et al. (2016).

4.3. Results and Discussion

4.3.1. Model Evaluation

Over the MRB (Figure 4-1), river discharge is found to be reasonably reproduced (Figure 4-2). Meanwhile, the oscillating hydrographs with high frequencies in the Mekong delta regions (CT and MTu stations) are not reproduced by CaMa-Flood because the boundary condition near ocean is assumed to be steady in CaMa-Flood version 3.6. Some of deviating hydrographs in those regions are attributed by the errors in DEMs in flat delta regions and high uncertainties in parameterization of river geometries in Mekong Delta region that cause the biases in bifurcation scheme (D. Yamazaki et al., 2017). Otherwise, river discharges on main stems (LP, PA, KT, and PP stations) and flow reversal in TSR (PK station) are well simulated. The related discussions are given in the model evaluation on flooded area below.

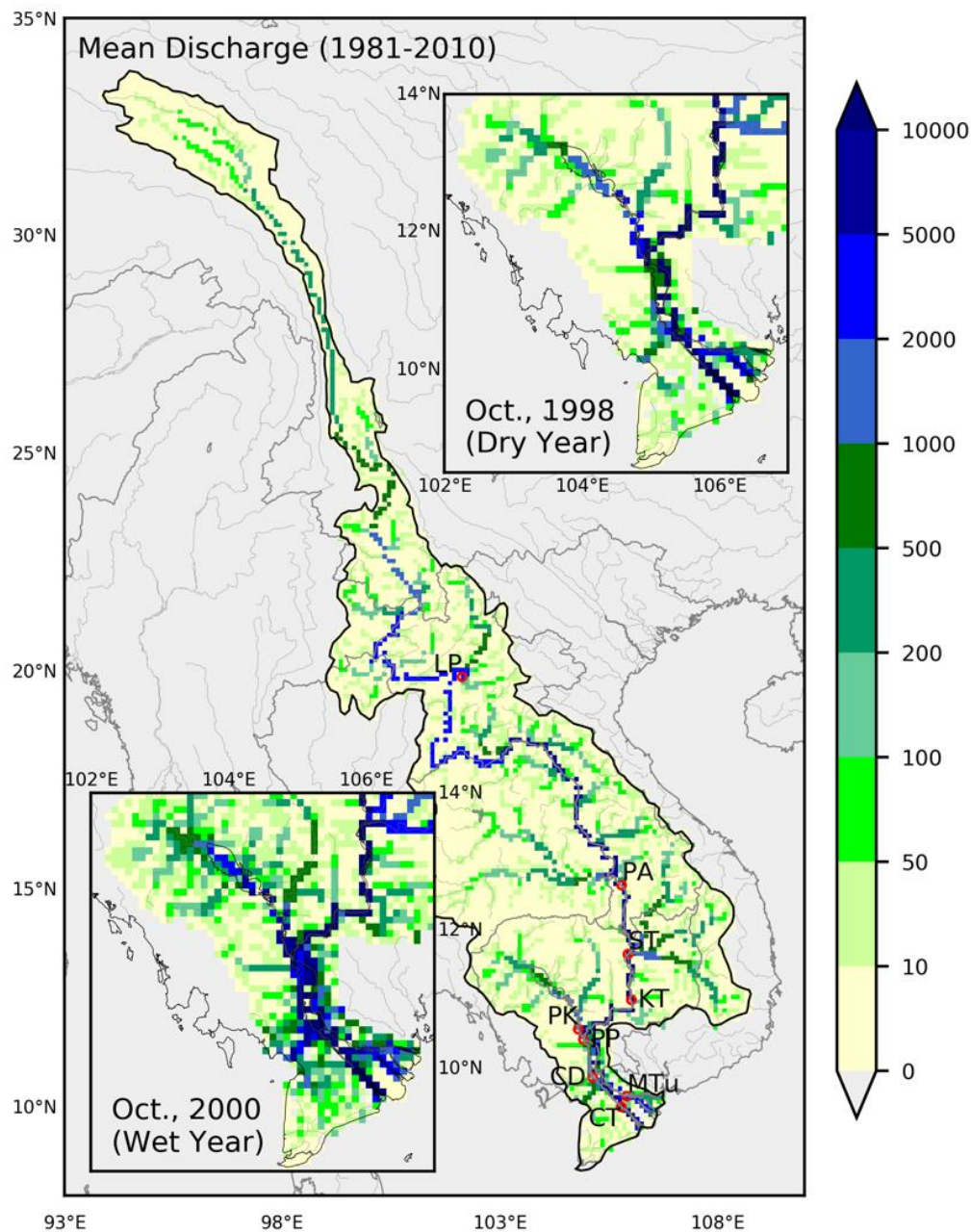


Figure 4-1 Long-term (1981-2010) mean river discharge (m^3/s) simulated by CaMa-Flood at 10km spatial resolution over the entire Mekong River Basin (MRB). The upper right and lower left insets show river discharge for the Lower Mekong during peak flow season in 1998 (dry year) and 2000 (wet year), respectively. Red circles show the locations for river discharge validation presented in Figure 4-2; station names are: LP (Luang Prabang), PA (Pakse), ST (Stung Treng), KT (Kratie), PP (Phnom Penh Port), PK (Prek Kdam), CD (Chau Doc), CT (Can Tho), and MTu (My Thuan).

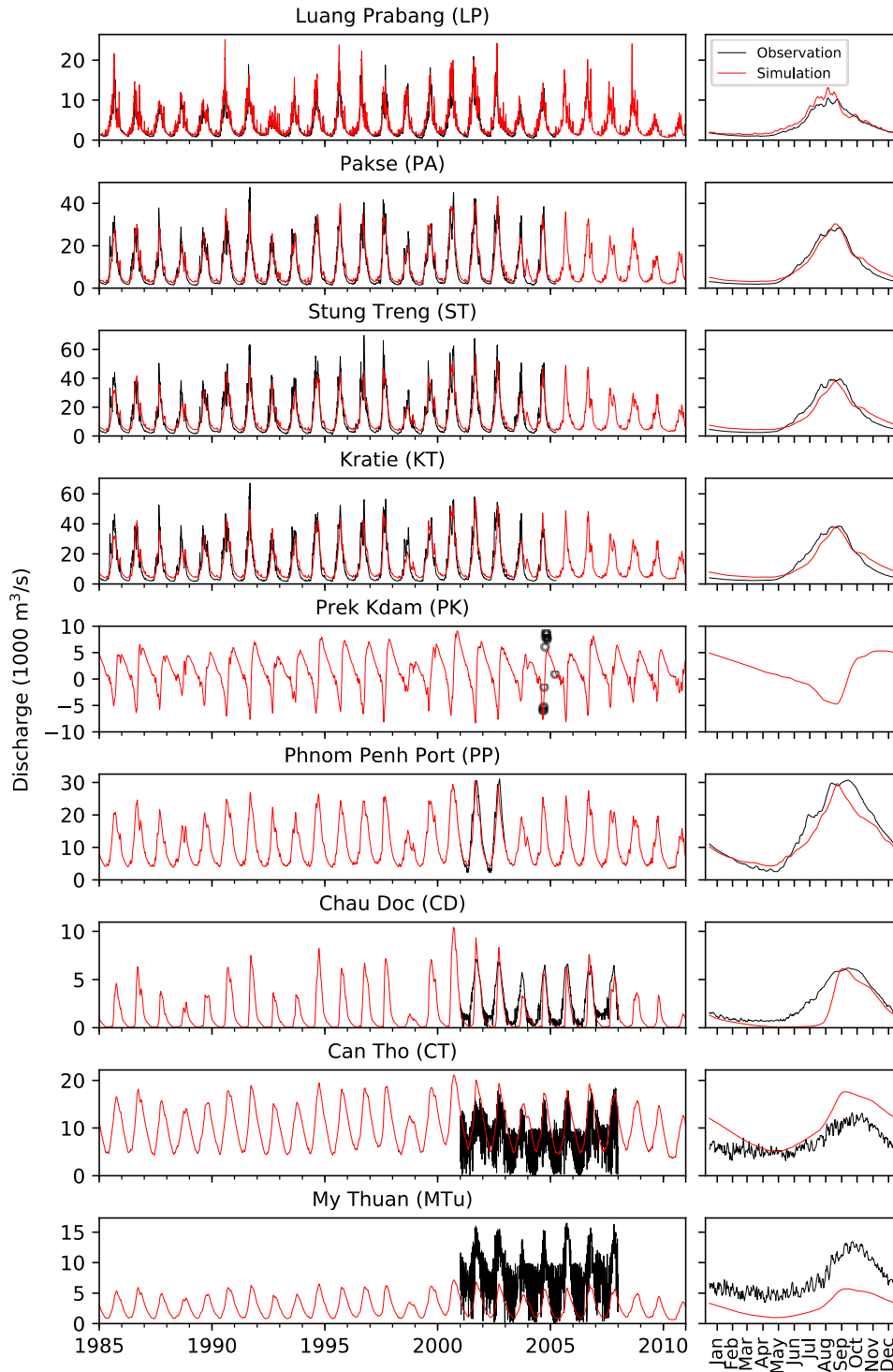


Figure 4-2 Evaluation of simulated river discharge with observations obtained from the Mekong River Commission (MRC) at locations indicated by red circles in Figure 4-1. While the simulated results are shown for the period of 1985-2010, observed data are shown for the period available. The right panels show the daily climatological mean over the period for which observations were available. For PK station, limited data were available only for year 2004.

Next, we evaluate flood occurrence (i.e., number of flooded months per year) and water surface elevation. Modeled flood occurrence, derived from the flood depth downscaled to 500m grids (Figure 4-3), is compared with the satellite-based 30m global data (upscaled to 500m) of historical water occurrence (Pekel et al., 2016) (Figure 4-4ab). A good agreement can be observed in terms of the broad patterns of flooded areas, but discrepancies are evident in flood occurrence itself. Notable differences can be seen around the northwest portion of the TSL, where numerous previous studies (Arias, Piman, et al., 2014; Kummu & Sarkkula, 2008; Sakamoto et al., 2007) as well as our results suggest a permanent water occurrence (i.e., 12-month flood occurrence) but the satellite data indicate nonexistence of such permanent water. This possible underestimation of permanent water occurrence in the satellite data results from underestimated water occurrence during April-July, likely due to the presence of relatively shallow and turbid water.

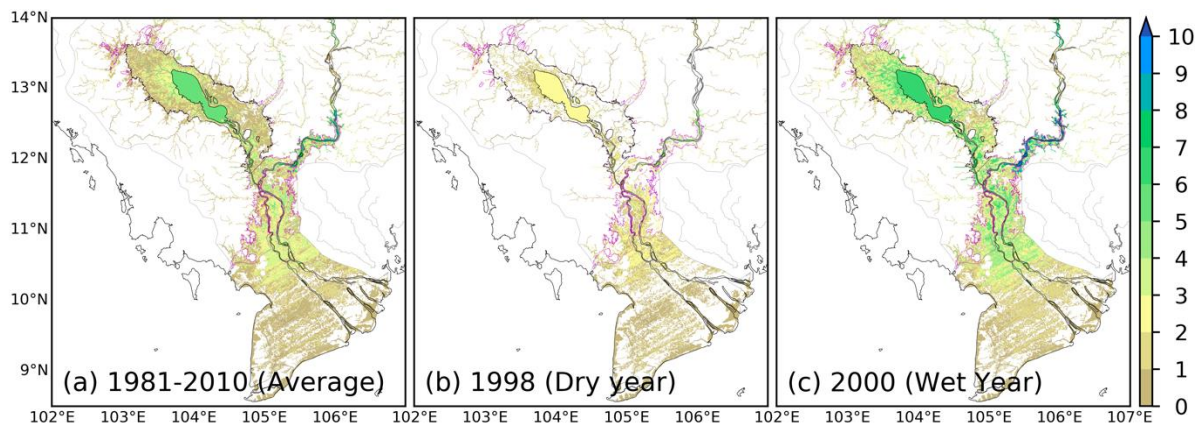


Figure 4-3 Simulated annual mean flood depth downscaled to 500m spatial resolution using high resolution SRTM topography data for (a) average year (mean of 1981-2010), (b) dry year (1998), and wet year (2000). The region enclosed by magenta lines shows the areas of major flood around Tonle Sap Lake (TSL) and Lower Mekong within Cambodia (source: <https://data.humdata.org/>), and the thick black outline marks the flooded areas around TSL used in previous studies (Arias et al., 2012).

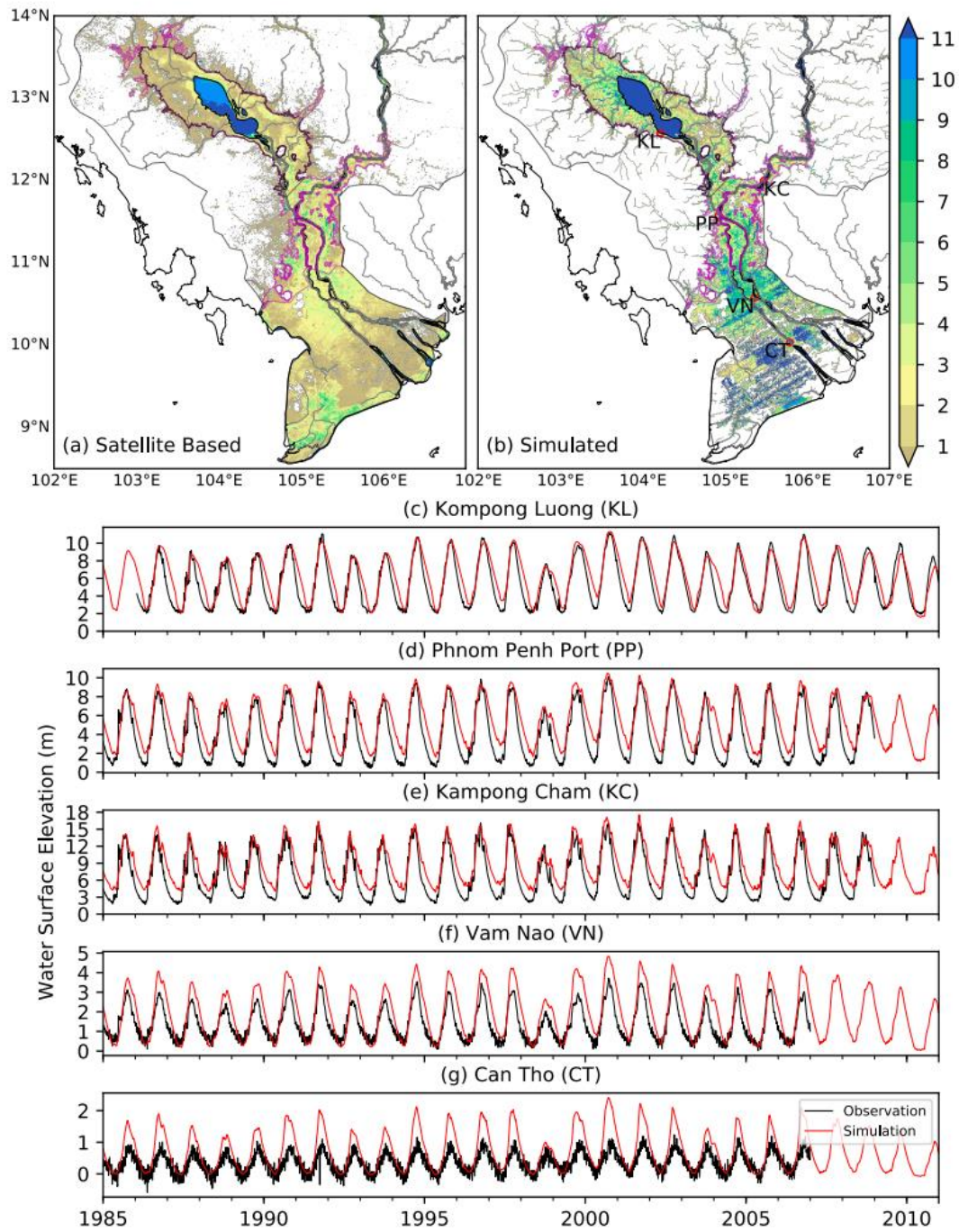


Figure 4-4 Monthly flood occurrence and daily water surface elevation. (a, b) Comparison of simulated flood occurrence (number of months) with satellite-based flood occurrence of Pekel et al. (2016). The region enclosed by magenta lines shows the areas of major flood around TSL and Lower Mekong within Cambodia (source: <https://data.humdata.org/>), and the thick black outline marks the flooded areas around TSL used in Arias et al. (2012). (c-g) Comparison of simulated (CaMa-Flood) and observed (obtained from MRC) water surface elevation at five stations indicated by red circles in (b). Observations are shown only for the period available.

Further, the model simulates high flood occurrence around the main body of the lake, along river channels, and the flat floodplains in the Mekong Delta, expected but not seen in the satellite data. This could be a possible model overestimation caused by the uncertainties in topographic and climate data, or an underestimation in the satellite product, which represents “open to sky” water presence, potentially underestimating water occurrence under vegetated areas such as in the gallery forests and flood-recession agriculture around the lake and in the delta region (Arias, Cochrane, et al., 2014). Moreover, while the model provides a continuous simulation of monthly flood occurrence, only limitedly available cloud-free images are used in the satellite product (Pekel et al., 2016). Note that the stripes in the Mekong Delta region (Figure 4-4b) result from small but inherent errors in the digital elevation model (DEM) in low-lying areas (D. Yamazaki et al., 2017). For TSL region, the model clearly captures the areas of major flood (magenta lines in Figure 4-4a,b). Further, comparison of simulated flooded areas with the estimates from a previous study (Arias et al., 2012) for the major flooded regions around TSL (black outline in Figure 4-4a) suggests that the model well captures the total flooded areas both during dry and wet seasons (Table 4-2).

Table 4-2 Comparison of flooded areas with Arias et al. (2012) for the major flood regions around Tonle Sap Lake indicated by thick black line in Figure 4-4a.

Dry Season	Flooded Area (km ²)			Difference (%) ^b	
	MODIS ^a	GIS ^a	CaMa-Flood (this study)	MODIS	GIS
5/8/2000	2,841	3,072	3,442	17	11
4/15/2001	2,751	3,096	3,671	25	16
5/25/2002	2,580	2,433	3,144	18	23
6/2/2003	2,605	3,003	3,173	18	5
5/16/2004	2,579	2,281	3,100	17	26
5/1/2005	2,841	3,177	3,036	6	-5
5/1/2006	2,667	2,442	3,143	15	22
5/17/2007	2,626	3,029	3,405	23	11
Wet Season	Flooded Area (km ²)			Difference (%)	
	MODIS	GIS	CaMa-Flood (this study)	MODIS	GIS
10/23/2000	14,763	14,030	14,521	-2	3
10/8/2001	14,392	13,792	13,038	-10	-6
10/16/2002	14,264	13,103	12,517	-14	-5
10/24/2003	12,037	10,863	9,330	-29	-16
10/23/2004	12,264	10,894	10,669	-15	-2
10/16/2005	13,026	12,665	10,480	-24	-21
10/24/2006	13,180	12,624	13,635	3	7
10/16/2007	12,404	12,300	10,668	-16	-15

^a MODIS and GIS data are from Arias et al. (2012)

^b Difference (%) = $\frac{\text{CaMa-Flood} - \text{MODIS (or GIS)}}{\text{CaMa-Flood}} \times 100$

Since the satellite data could contain uncertainties, we evaluate the modeled water surface elevation—a primary determinant of flood extent, depth, and occurrence—with the ground-based observation to add further confidence to our flood simulations (Figure 4-4 c-g). Evidently, both the seasonal magnitude and temporal variability of water elevation are well captured by the model, especially at the Kompong Luong (KL) in the TSL and Phnom Penh Port (PP). Simulated water levels are not as accurate in the lower portion of the delta (e.g., Can Tho; Figure 4-4g), which could be due to the uncertainties in DEM, river width, and channel bathymetry represented in our river bifurcation scheme (D. Yamazaki et al., 2014). At Can Tho, discrepancies could also be attributed to tide effects, not considered in the current model. Given the scale of the model domain, uncertainties in data, and the difficulty in accurately representing channel bifurcation, we consider these results to be reasonable for this study.

4.3.2. Role of River-Floodplain Storage on TWS dynamics and Historical Variability

Next, we examine the role of river-floodplain water storage in modulating the TWS dynamics in the MRB using TWS variations simulated by the models and from GRACE satellites. By comparing the TWS solely from HiGW-MAT, the combined TWS from HiGW-MAT and CaMa-Flood, and TWS from GRACE, we find that river-floodplain storage plays a critical role in modulating the total TWS variations, and hence the hydrology of the MRB (Figure 4-5). First, the variations in river-floodplain storage from CaMa-Flood (solid blue line) exhibit substantially larger seasonal amplitude than the river storage (dashed blue line) in HiGW-MAT that does not consider TSR flow reversal and lacks floodwater storage. While certain inter-annual variations are obvious, the differences can be clearly discerned from the seasonal cycle (**Figure 4-5b**). Second, a one-month delay in the peak can be seen in river-floodplain storage in CaMa-Flood as compared to the river storage in HiGW-MAT, which expectedly results from

larger floodplain storage in CaMa-Flood during wet season—partly due to TSR flow reversal—and a subsequent release in the dry season.

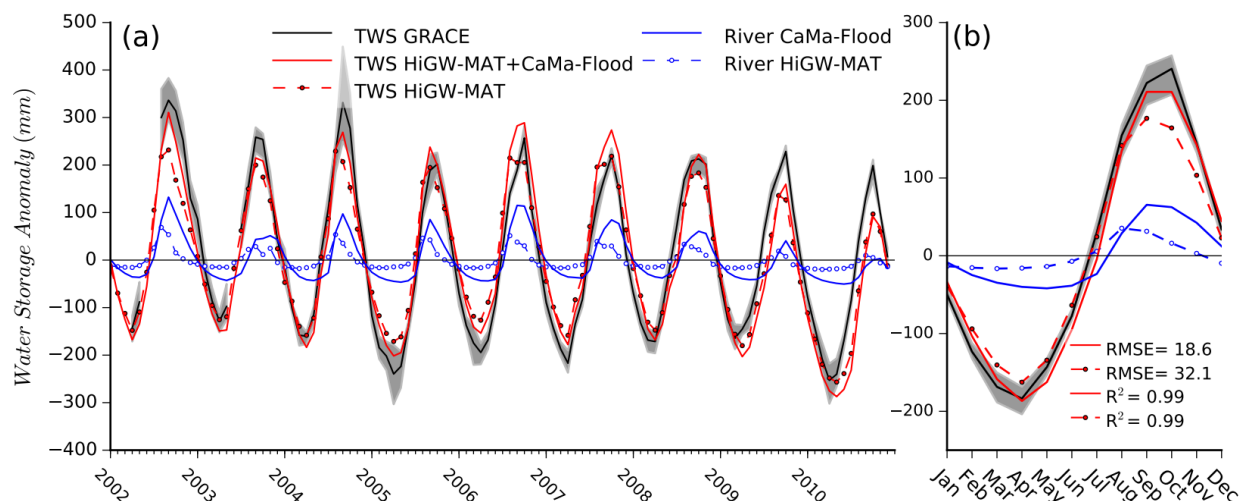


Figure 4-5 Role of river-floodplain storage on TWS dynamics over the MRB. (a) Black line shows the mean of TWS anomaly from spherical harmonics- and mascon-based GRACE products with the range between different products indicated by grey shading. For modeled TWS anomalies, four sets of result are shown: combined total TWS from HiGW-MAT and CaMa-Flood (solid red), total TWS only from HiGW-MAT (dashed red), river-floodwater storage from CaMa-Flood (solid blue), and river water storage from HiGW-MAT (dashed blue) which lumps the flood water storage. (b) The seasonal cycle. Results are averaged for the entire MRB.

Third, as a consequence of larger seasonal swing and delayed peak in CaMa-Flood, the combined TWS from HiGW-MAT and CaMa-Flood provides a better agreement with GRACE compared to the TWS from HiGW-MAT alone. The better agreement is reflected not only graphically, but also statistically; while the already-high R^2 (0.99) does not change, the root mean squared error (RMSE) reduces from ~32 to ~18mm (**Figure 4-5b**). Because GRACE provides the vertically integrated total TWS, not its components (e.g., Pokhrel et al., 2013), river-floodplain storage from CaMa-Flood could not be separately validated, but an independent evaluations of water level (**Figure 4-4 c-g**) and river discharge (**Figure 4-1** and **Figure 4-2**) suggest that CaMa-Flood well simulates the overall hydrodynamics. Fourth, comparison of the

seasonal amplitude in the combined TWS (Figure 4-5; solid red line) and the river-floodplain storage from CaMa-Flood (Figure 4-5b; solid blue line) suggests that river-floodplain storage explains ~27% of the seasonal amplitude of total TWS variations averaged over the entire MRB as opposed to only ~13% by river storage in HiGW-MAT (Figure 4-5; dashed blue line); for the LMRB, while CaMa-Flood river-floodplain storage contributes to ~49% of total TWS, HiGW-MAT river storage only accounts for ~12% (Figure 4-6). These findings imply that the potential alterations in the Mekong flood pulse and TSR flow reversal will affect not only the dynamics of flood patterns but also the overall basin hydrology because changes in surface water storage can alter other components of the basin water balance.

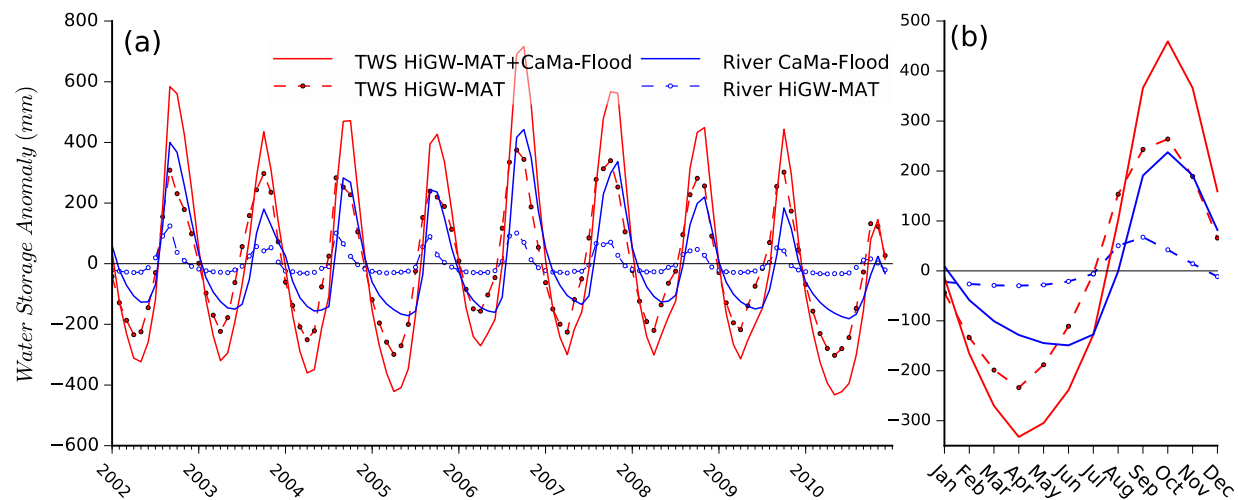


Figure 4-6 Same as in Figure 4-5 but only for the Lower Mekong region. Note that GRACE data are not included here because of the reduced reliability of the data when averaged over small regions.

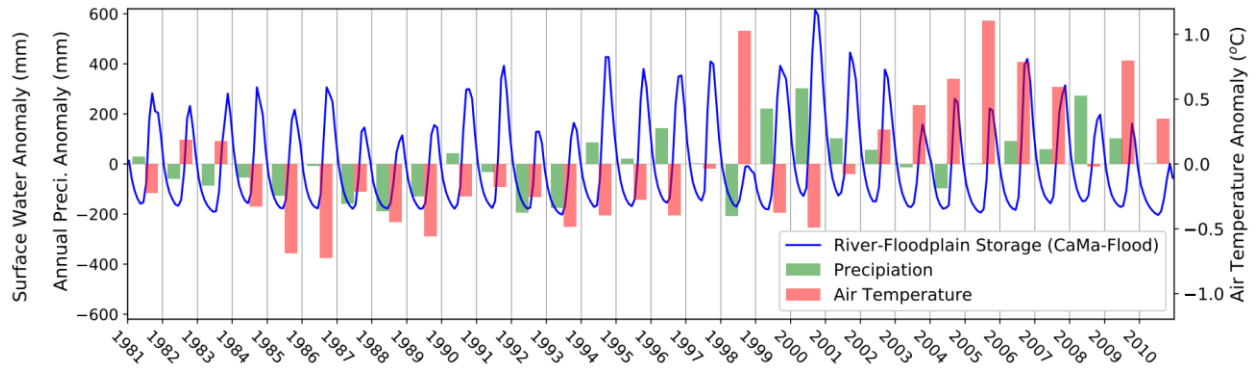


Figure 4-7 Relationship between river-floodplain storage from CaMa-Flood (monthly) and climate variability (annual mean precipitation and temperature) over the Lower Mekong domain. Precipitation and temperature data are same as those used as input to HiGW-MAT model.

Figure 4-7 shows the historical variations in river-floodplain storage from CaMa-Flood over the Lower Mekong domain under varying climate conditions (i.e., annual precipitation and temperature). Evidently, annual storage variations are largely dictated by the variabilities in inter-annual precipitation (correlation of 0.67) and temperature (correlation of -0.31). High precipitation, often combined with low basin-wide temperatures, lead to wet years and vice versa; however, no significant trend in river-floodplain storage (Mann-Kendall test, $p=0.958$, $\alpha=0.05$) is found over the 30-year period. The lowest and highest storages clearly stand out in years 1998 and 2000, which are among the driest and wettest years, respectively in past few decades (Hung et al., 2012; Mekong River Commission, 2005); flood occurrence in these years is discussed further in the next chapter. Note that these results do not account for the effects of existing dams, but such effects are relatively small compared to the flow volume in the main stem of the Mekong (**Figure 4-8**).

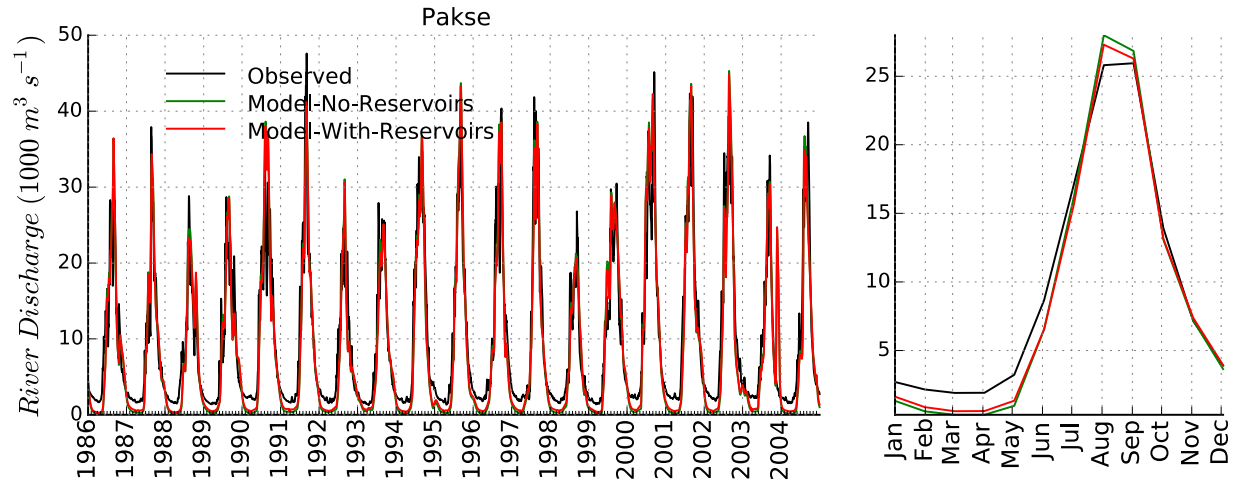


Figure 4-8 Daily river discharge at Pakse (PA) station (location shown in Figure 4-1 and Table 4-1) simulated by HiGW-MAT model with and without considering the existing dams. Observed data from MRC are also shown. The right panel shows the monthly seasonal cycle. Model results are taken from Pokhrel et al. (2015).

4.3.3. Potential Effects of Flow Regulation on Flood Dynamics in the LMRB

4.3.3.1. Potential Effects of Flow Regulation on Mean River Discharge in the LMRB

Figure 4-9 presents the potential effects of upstream flow regulation (altered magnitude and timing of peak near Stung Treng, **Table 4-1**; marked by a star in **Figure 4-11**) on downstream flow dynamics in the mainstream Mekong, TSR, and some distributaries in the delta region (locations shown in **Figure 4-11**; Table 4-1). Note that only the magnitude and timing of peak is altered, and mass balance is preserved in all flow regulation scenarios. Results in **Figure 4-9** represent a surrogate of an average year, defined as the mean for 1981-2010 period; typical dry and wet years are discussed next. Up to the PP station, highly similar altered flow patterns are observed to that at the dam location (**Figure 4-9a-c**) but interesting features emerge in the downstream of PP and in the TSR. Most notably, upstream flow alterations are found to severely impact the magnitude, timing, and direction of discharge into TSL (LO and PK stations; **Figure 4-9d,e**), which could potentially disrupt the natural flood dynamics in the TSR and cause a

regime shift in TSL water balance. Results suggest that, for different flow regulation scenarios, the peak of flow from the TSL to the Mekong would reduce by 7-37% and 7-34% (**Table 4-3a**) and that of the reversed flow from the Mekong into TSL by 11-80% and 15-88% (**Table 4-3b**) at LO and PK stations, respectively. Together, the changes in the peaks of the bi-directional flow in the TSR would dampen the seasonal amplitude (i.e., maximum-minimum) of the hydrograph at LO and PK stations by 8-51% and 10-60% (**Table 4-3c**), respectively, under different upstream flow regulation scenarios. These changes in flood dynamics could significantly alter the onset, duration, and amount of flow reversal in the TSR. We find that the onset could be delayed by 1-38 days and 1-40 days (**Table 4-3d**), respectively, at LO and PK stations, with a reduction in the total duration of reversed flow by 2-51 days and 2-55 days (**Table 4-3e**). As a result, the total volume of water entering the TSL due to flow reversal could reduce from 12,202 (23,646) million m³ by 14-87% (15-92%) at the LO (PK) station for different flow alteration scenarios (**Table 4-3f**).

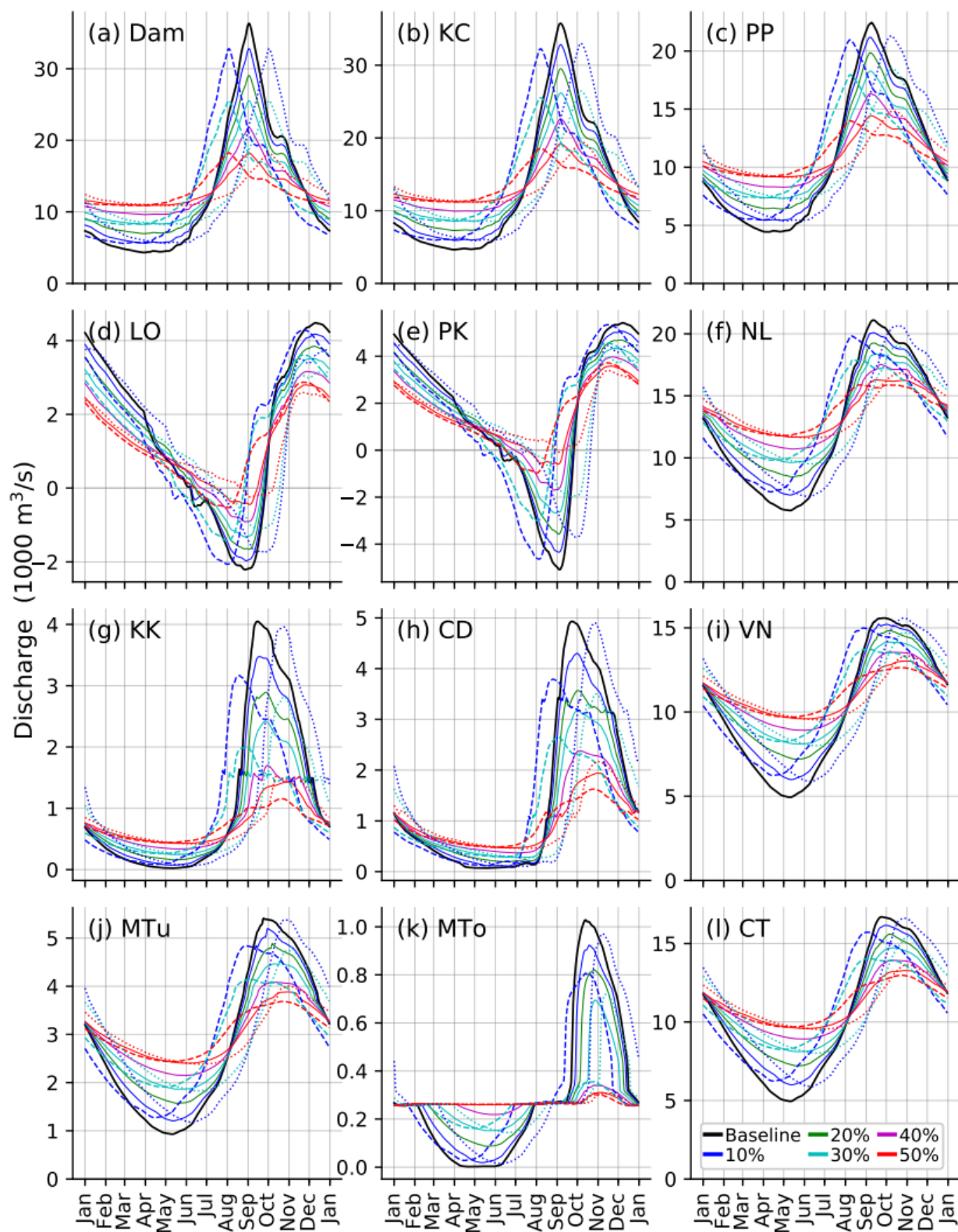


Figure 4-9 Potential changes in daily river discharge by flow regulation. The thick black line shows the baseline flow (1981-2010 average); other colors represent different scenarios of

change in peak flow magnitude (solid lines). Dashed and dotted lines represent the scenarios of early and delayed peak timing, respectively, by one month for different degree of peak flow alteration represented by the color coding. Results of altered timing are shown only for 10, 30, and 50% peak flow reduction scenarios. Station names are: KC (Kampong Cham), PP (Phnom Penh Port), LO (Lake Outlet), PK (Prek Kdam); NL (Neak Luong), KK (Koh Khel), CD (Chau Doc), VN (Vam Nao), MTu (My Thuan), MTo (My Tho), and CT (Can Tho); latitudes and longitudes are provided in **Table 4-1**.

Table 4-3 Changes in major flood characteristics (e.g., onset, magnitude, duration, and amount) compared to the baseline simulation at different stations analyzed in Figure 4-8. The Lake Outlet (LO) and Prek Kdam (PK) stations are indicated by grey shading. Numbers enclosed in boxes are those noted in the text. For 10, 30, and 50% peak flow alteration scenarios, results for the scenarios with one-month early and delayed peak timing are also provided.

(a) Q_{\max} in baseline (m^3/s) and $\Delta Q_{\max}(\%)$													(b) Q_{\min} in baseline (m^3/s) and $\Delta Q_{\min}(\text{m}^3/\text{s})$												
Station	Baseline (m^3/sec)	10% Delay	10% Early	20%	30%	30% Delay	30% Early	40%	50%	50% Delay	50% Early		Station	Baseline (m^3/sec)	10%	10% Delay	10% Early	20%	30%	30% Delay	30% Early	40%	50%	50% Delay	50% Early
Dam	36,329	-10	-10	-10	-20	-30	-30	-40	-50	-50	-50		Dam	4,318	1,280	1,280	1,280	2,646	3,927	3,927	3,927	5,293	6,573	6,573	6,573
KC	35,747	-8	-8	-10	-17	-27	-26	-29	-37	-46	-48		KC	4,645	1,264	1,235	1,311	2,625	3,907	3,875	3,967	5,287	6,547	6,528	6,587
PP	22,450	-6	-5	-7	-12	-19	-17	-20	-27	-36	-38		PP	4,434	980	948	1,026	1,972	2,879	2,858	2,933	3,839	4,721	4,694	4,764
LO	4,479	-7	-16	-4	-14	-22	-29	-19	-29	-37	-42	-36	LO	-2,210	240 (-11%)	458 (-21%)	146 (-7%)	551 (-25%)	887 (-40%)	1,105 (-50%)	798 (-36%)	1,293 (-58%)	1,762 (-80%)	1,967 (-89%)	1,682 (-76%)
PK	5,423	-7	-17	-1	-13	-20	-27	-16	-27	-34	-37	-31	PK	-5,085	742 (-15%)	1,394 (-27%)	444 (-9%)	1,508 (-30%)	2,414 (-47%)	3,076 (-60%)	2,076 (-41%)	3,376 (-66%)	4,483 (-88%)	5,002 (-98%)	4,120 (-81%)
NL	21,105	-5	-2	-6	-9	-13	-10	-15	-17	-23	-20	-25	NL	5,749	1,244	1,131	1,509	2,709	3,865	3,754	4,062	4,965	5,921	5,843	6,038
KK	4,049	-14	-2	-22	-29	-40	-30	-50	-58	-65	-62	-71	KK	25	46	40	60	134	221	210	237	313	403	394	416
CD	4,931	-13	-1	-23	-28	-35	-29	-46	-52	-61	-56	-67	CD	69	36	31	45	123	210	203	223	300	396	387	415
VN	15,578	-2	0	-4	-5	-9	-6	-12	-13	-16	-14	-19	VN	4,938	1,046	933	1,288	2,266	3,168	3,065	3,305	3,976	4,654	4,600	4,749
MTu	5,408	-4	0	-11	-10	-16	-11	-23	-24	-28	-26	-32	MTu	930	275	244	342	641	933	899	980	1,219	1,472	1,453	1,507
MTTo	1,028	-10	-5	-22	-20	-32	-30	-65	-67	-70	-70	-71	MTTo	2	16	12	26	85	149	142	160	216	253	253	252
CT	16,704	-3	-1	-6	-7	-12	-8	-16	-17	-20	-18	-22	CT	4,948	1,049	934	1,288	2,268	3,170	3,067	3,307	3,968	4,638	4,587	4,727
(c) $Q_{\max} - Q_{\min}$ in baseline (m^3/s) and $\Delta(Q_{\max} - Q_{\min})(\%)$													(d) Onset of reversed flow in baseline (day of year) and its change (day)												
Station	Baseline (m^3/sec)	10% Delay	10% Early	20%	30%	30% Delay	30% Early	40%	50%	50% Delay	50% Early		Station	Baseline (DOY)	10%	10% Delay	10% Early	20%	30%	30% Delay	30% Early	40%	50%	50% Delay	50% Early
Dam	32,012	-15	-15	-15	-31	-46	-46	-62	-77	-77	-77		LO	159	1	32	-29	6	8	37	-20	16	38	74	7
KC	31,102	-13	-13	-15	-28	-43	-42	-46	-59	-74	-73	-76	PK	160	1	32	-29	7	9	42	-18	21	40	83	8
PP	18,016	-12	-12	-14	-25	-39	-38	-41	-55	-71	-68	-73	(e) Duration of reversed flow in baseline (day) and its change (day)												
LO	6,690	-8	-17	-5	-18	-28	-36	-25	-39	-51	-57	-49	Station	Baseline (Days)	10%	10% Delay	10% Early	20%	30%	30% Delay	30% Early	40%	50%	50% Delay	50% Early
PK	10,508	-10	-22	-5	-21	-33	-43	-28	-46	-60	-67	-55	LO	112	-2	-7	0	-9	-13	-16	-13	-24	-51	-63	-46
NL	15,356	-15	-10	-18	-30	-43	-38	-47	-56	-70	-66	-73	PK	109	-2	-13	1	-10	-15	-23	-14	-31	-55	-100	-48
KK	4,024	-15	-3	-23	-32	-46	-36	-57	-66	-75	-72	-82	(f) Volume of reversed flow in baseline (10^6 m^3) and its change (%)												
CD	4,862	-14	-1	-24	-31	-40	-34	-52	-59	-70	-65	-77	Station	Baseline (Mm^3)	10%	10% Delay	10% Early	20%	30%	30% Delay	30% Early	40%	50%	50% Delay	50% Early
VN	10,641	-13	-9	-18	-28	-43	-37	-48	-56	-68	-64	-72	LO	12,202	-14	-25	-9	-29	-47	-56	-43	-68	-87	-94	-84
MTu	4,478	-11	-6	-20	-26	-41	-33	-50	-57	-67	-64	-72	PK	23,646	-15	-30	-7	-31	-50	-64	-43	-72	-92	-100	-86
MTTo	1,026	-12	-7	-24	-28	-47	-44	-81	-88	-94	-95	-95													
CT	11,757	-13	-9	-19	-29	-44	-37	-51	-57	-69	-65	-72													

In the Mekong Delta region, flow regulations cause relatively predictable changes in river flow dynamics along the mainstream channels, but flood dynamics becomes highly unpredictable in the distributaries and bifurcated channels. In the main channels (e.g., NL, VN, and CT stations; **Figure 4-9f,i,l**), the alterations in the magnitude of seasonal amplitude (i.e., dampened peak and enhanced low flow) show a similar pattern to the upstream flow alterations with a more pronounced increase in low flow than the reduction in flood peak. This interesting phenomenon in the downstream of the confluence of the TSR results partly from the weakened flow reversal in the TSR; that is, because less water flows into the TSR during wet season, the mainstream flow in the downstream of PP station is not significantly affected by TSR flow reversal. Consequently, in dry season, most of the enhanced low flow from the upper main stem is directly discharged to the downstream with considerably less contribution from TSR flow. In other words, while the TSL plays a role of a detention reservoir by dampening flood peak and enhancing low flow in the downstream, such role becomes less significant when the mainstream flow is regulated by upstream reservoirs, reducing the wet-season flow into the lake.

At the KK and CD stations (**Figure 4-9g,h**) which are on the Bassac River, a distributary of the Mekong originating near PP, flood peak is substantially reduced due to the dampened upstream flood peak; however, the increase in low flow is relatively small but distributed over a longer period than at the mainstream stations. Understanding these potential changes in high and low flows is crucial because the Bassac River is a critical transportation corridor between Cambodia and Vietnam. Moreover, in these downstream locations likely increase in water levels due to sea level rise and tides could interfere with the changes brought by upstream dam regulation, causing unpredictable flow and water level patterns. Further downstream, highly unpredictable flows are observed at MTo (near My Tho in Vietnam) station (**Figure 4-9k**),

because of unpredictable changes in channel bifurcation dynamics; here, flood seasonality potentially ceases under high upstream flow regulation and delayed peak scenarios (**Table 4-3a,b**). Note that some of these changes could have resulted from the uncertainties in channel bifurcation simulations in our model in the low-lying areas as discussed earlier.

Figure 4-9 also includes the results from simulations with one month early and delayed peak at the dam location. Overall, the changed timing of peak results in correspondingly shifted hydrograph in the immediate downstream of dam location; however, the altered timing is found to affect also the magnitude of peak flow in the TSR and delta region. At LO and PK stations (**Figure 4-9 d-e**), the compounded effects of reduced peak and altered timing cause an even larger impact on the timing, duration, and amount of reversed flow than caused only by reduced peak (also see **Table 4-3 d-f**). Notably, results suggest that TSR flow reversal at PK station almost ceases if the flood peak reduced by 50% arrives with a one month delay relative to the baseline flow (**Figure 4-9e, Table 4-3b**). In the delta region (e.g., KK and CD; **Figure 4-9 g-h**), delayed (early) timing is found to increase (reduce) the flood peak magnitude, suggesting that there is an optimum timing for flood patterns to be maintained at the base level; any changes in timing can causes a significant increase or decrease in the flood peak magnitude. The changes in water surface elevation are found to follow similar patters to the changes in discharge (**Figure 4-10**).

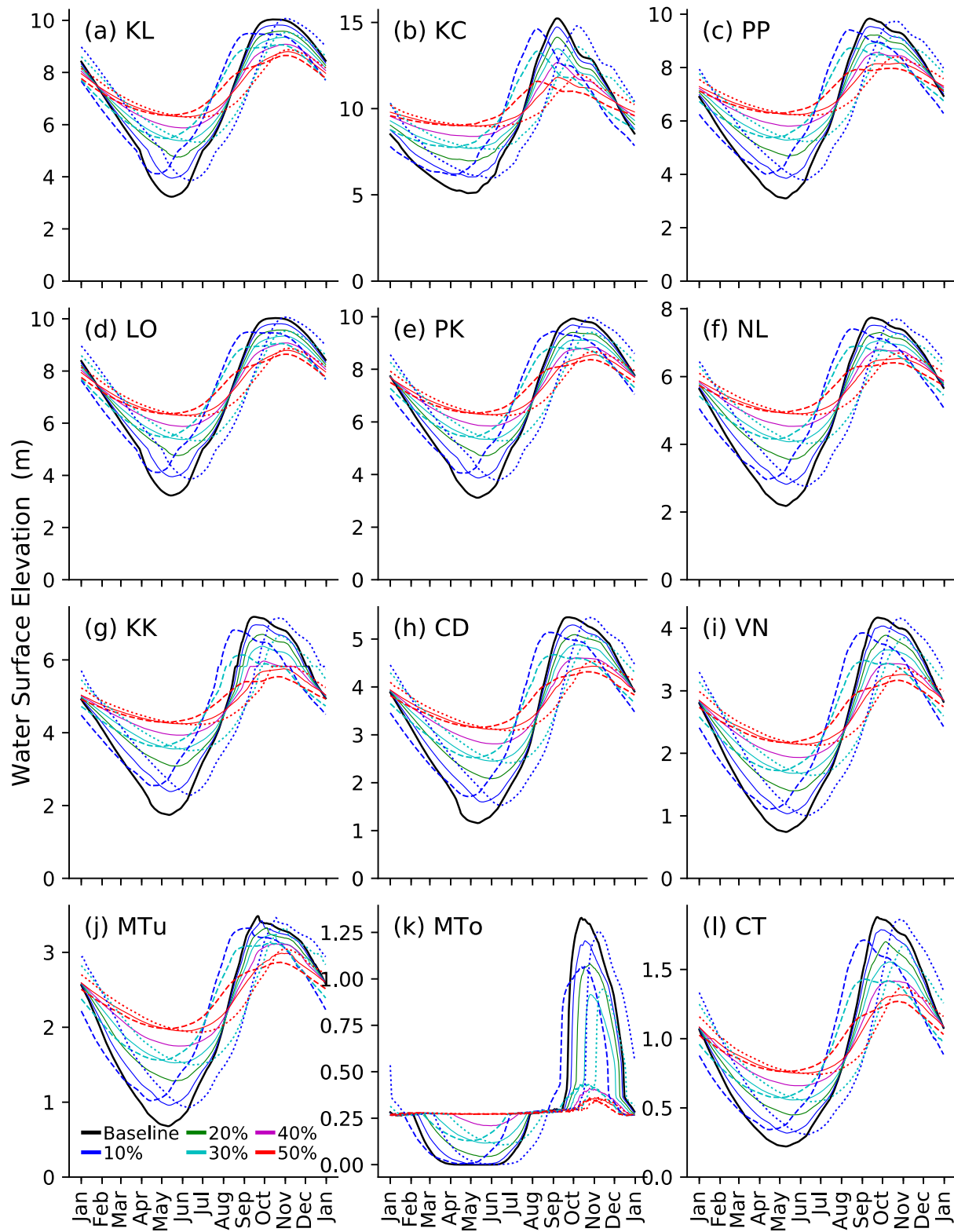


Figure 4-10 Same as in Figure 4-9 but for simulated water level (i.e., water surface elevation).

4.3.3.2. Potential Effects of Flow Regulation on Mean Flood Occurrence in the LMRB

Figure 4-11 presents the changes in flood occurrence within the same spatial domain shown in **Figure 4-4**. Evidently, downstream impacts vary among different scenarios of flow regulation. First, the changes are relatively small for 10% and 20% peak reduction. Second, increased flood occurrence can be seen at the vicinity of TSL and along the main river channels because of increased water retention during dry season. Away from the lake and in the flooded agricultural areas, flood occurrence decreases significantly (by up to 5 months or more) because of large decline in flood water entering the TSL from the Mekong during wet season. Overall, flooded areas in the TSL region (thick black line within the red rectangle in **Figure 4-11f**) averaged for the high flood season (August-October) decrease by 413 km² (4.6%), 774 (8.6%), 1122 (12.5%), 1602 (17.8%), and 2075 (23.1%) for 10, 20, 30, 40, and 50% scenarios, respectively. Similarly, flooded areas during dry season (April-June) increase by 93 km² (2.9%), 311 (9.7%), 580 (18.1%), 862 (26.9%), and 1144 (35.7%). Results suggest that the flooded areas in the floodplains upstream of PP (green rectangle in **Figure 4-11f**) also decrease significantly under all flow alteration scenarios. Third, no significant change in water occurrence can be observed within the main body of TSL, suggesting the presence of permanent water under all flow alteration scenarios, which could partly be attributed to a simple treatment of lake bed elevations owing to the inherent limitations in DEM data that provide only the water surface elevation over water bodies and the lack of spatially-explicit bathymetry data. Thus, these results should be interpreted with caution.

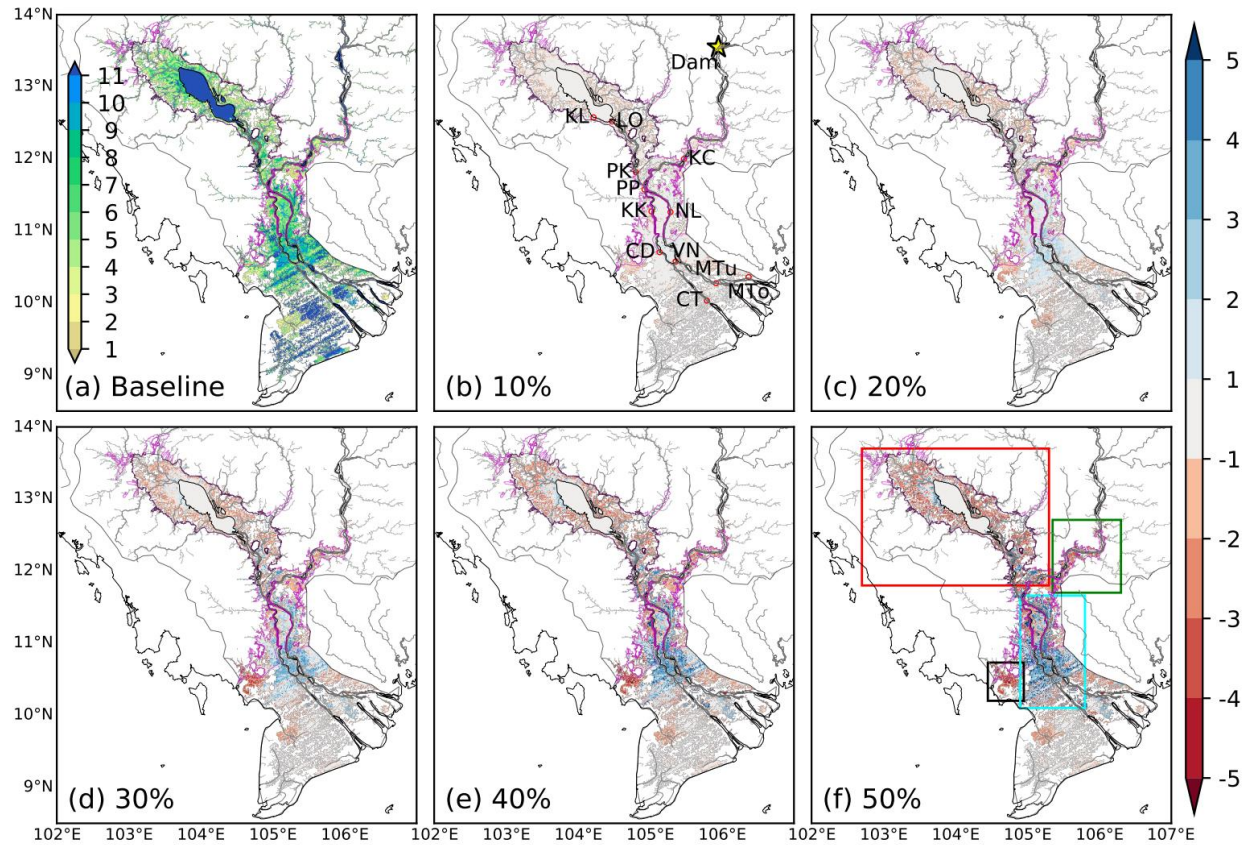


Figure 4-11 Flood occurrence and the effects of flow regulation on it. (a) Same as in Figure 4-4 but based on the baseline simulation with 1981-2010 mean runoff. (b-f) Change in flood occurrence (number of months) for change in peak flow by different degree as indicated with reference to the baseline flood occurrence (a). The star in (b) shows the Stung Treng station where flow is altered. Rectangles in (f) show regions in the LMRB discussed in the text. For magenta and black lines, see description in **Figure 4-4** caption.

Fourth, in the Mekong Delta region, a large increase in flood occurrence can be seen in the middle reach (post-flooding agricultural areas; cyan rectangle in **Figure 4-11f**) for >30% flow regulation. Again, this results from a relatively small impact on the mainstream flow during flood season as less water enters the TSL and an increase in low because of dam release (**Figure 4-9f,i,l**). Farther from the mainstream channels in the lower portion of the delta, flood occurrence mostly reduces because lowered water levels (**Figure 4-10j,k**) in the mainstream channels prevent frequent overtopping to the floodplains. Fifth, no changes in flood occurrence can be seen in mainstream Mekong and Bassac Rivers as well as other distributaries near the river

mouth. In these regions, the magnitude and timing of water levels are simulated differently under different scenarios, but the water occurrence remains unchanged because of permanent water occurrence in the model. Finally, our results indicate that while the areas flooded for ~6 months are least impacted by flow regulation during average years, the areas flooded for ~1 (~12) months could decrease (increase) significantly under all flow alteration scenarios and both in the TSL region as well as the entire Lower Mekong domain (**Figure 4-12**). This is a direct consequence of the reduced flood peak and increased low flow under all flow regulation scenarios. In terms of the impacts of changed flood peak timing, the effects tend to become smaller with increased duration of flood occurrence; in general, regions that are flooded over nine months are minimally impacted both in the Lower Mekong and TSL regions (**Figure 4-12**). Similar patterns were reported in a previous study (Arias, Piman, et al., 2014) in that the reductions in peak and increases in low flows are amplified for higher degrees of flow regulation. Similarities are found also in terms of the least impacted flood occurrence (in general, 40-60%, which is similar to ~6 months in a year). These comparisons are summarized in **Table 4-4**, but it is noted that the results are not directly comparable because of the differences in simulation settings (see footnotes in **Table 4-4**), which results in considerably different baseline simulations (Two-sample K-S test, $p=0.11$, $\alpha=0.05$).

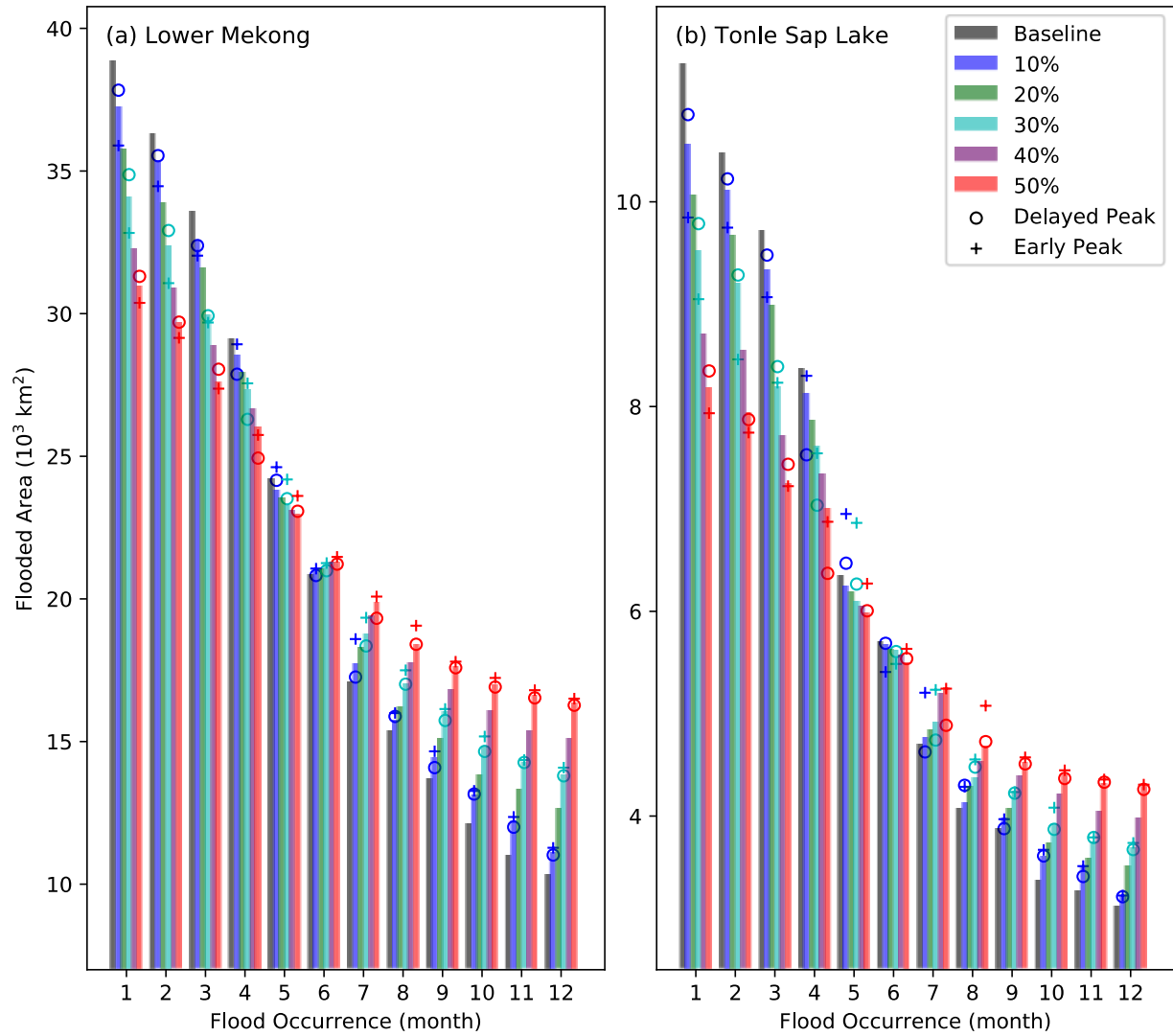


Figure 4-12 Flooded areas having different flood occurrence estimated from the baseline simulation results presented in Figure 4-11 and their changes under different flow regulation scenarios for (a) the entire domain shown in Figure 4-11, and (b) the TSL region marked by thick black line within the red rectangle in Figure 4-11f. Plus signs and open circles show the results from the early and delayed peak flood timing by one month, respectively.

Table 4-4 A summary of the results of potential changes in flooded area around Tonle Sap Lake under different flow regulation scenarios from this study and those from Arias, Piman, et al. (2014). Flooded days with the smallest change are marked by grey shading. As noted in the text, the results are not directly comparable due to differences in simulation settings between the two studies.

Flood occurrence ^c (%)	Flooded area (km ²) and its change from baseline simulations in km ² (% in parentheses) ^a														
	Arias, Piman, et al. (2014)			This study											
	Baseline	DF ^b	DF+3S ^b	Baseline	10%	10% Delay	10% Early	20%	30%	30% Delay	30% Early	40%	50%	50% Delay	50% Early
≤ 10	16670	-94 (-0.6)	-120 (-0.7)	11129	-729 (-4.4)	74 (0.4)	-1404 (-8.4)	-1206 (-7.2)	-1627 (-9.8)	-1258 (-7.5)	-2180 (-13.1)	-2117 (-12.7)	-2891 (-17.3)	-2770 (-16.6)	-3147 (-18.9)
≤ 20	14912	-271 (-1.8)	-404 (-2.7)	10637	-433 (-2.9)	-249 (-1.7)	-1048 (-7.0)	-888 (-6.0)	-1434 (-9.6)	-1230 (-8.2)	-2191 (-14.7)	-2229 (-14.9)	-2759 (18.5)	-2669 (-17.9)	-2987 (-20.0)
≤ 30	13495	-322 (-2.4)	-569 (-4.2)	9729	-382 (-2.8)	-538 (-4.0)	-477 (-3.5)	-784 (-5.8)	-1408 (-10.4)	-1538 (-11.4)	-1543 (-11.4)	-1888 (-14.0)	-2411 (-17.9)	-2451 (-18.2)	-2563 (-19.0)
≤ 40	12074	-262 (-2.2)	-423 (-3.5)	7905	-208 (-1.7)	-352 (-2.9)	-12 (-0.1)	-448 (-3.7)	-692 (-5.7)	-814 (6.7)	-478 (-4.0)	-918 (-7.6)	-1148 (-9.5)	-1566 (-13.0)	-1101 (-9.1)
≤ 50	10407	-149 (-1.4)	-236 (-2.3)	6187	-63 (-0.6)	-124 (-1.2)	149 (1.4)	-147 (-1.4)	-236 (-2.3)	-323 (-3.1)	-18 (-0.2)	-301 (-2.9)	-427 (-4.1)	-470 (-4.5)	-251 (-2.4)
≤ 60	8874	-36 (-0.4)	-52 (-0.6)	4827	53 (0.6)	6 (0.1)	361 (4.1)	292 (3.3)	325 (3.7)	163 (1.8)	468 (5.3)	376 (4.2)	421 (-4.7)	399 (4.5)	527 (5.9)
≤ 70	7483	126 (1.7)	321 (4.3)	4186	74 (1.0)	91 (1.2)	171 (2.3)	171 (2.3)	270 (3.6)	261 (3.5)	365 (4.9)	383 (5.1)	515 (6.9)	491 (6.6)	619 (8.3)
≤ 80	6552	191 (2.9)	290 (4.4)	3631	125 (1.9)	143 (2.2)	186 (2.8)	248 (3.8)	506 (7.7)	456 (7.0)	584 (8.9)	685 (10.5)	839 (12.8)	833 (12.7)	895 (13.7)
≤ 90	5603	199 (3.6)	354 (6.3)	3244	57 (1.0)	69 (1.2)	242 (4.3)	410 (7.3)	569 (10.1)	543 (9.7)	634 (11.3)	911 (16.3)	1097 (19.6)	1096 (19.6)	1151 (20.5)
≤ 100	4910	278 (5.7)	424 (8.6)	3103	73 (1.5)	61 (1.2)	67 (1.4)	240 (4.9)	587 (11.9)	575 (11.7)	619 (12.6)	843 (17.2)	1171 (23.9)	1153 (23.5)	1211 (24.7)

^a Spatial domain of Tonle Sap Lake region is exactly same as in Arias, Piman, et al. (2014)

^b DF: Water infrastructure development plan up to 2015; DF+3S: Cumulative impact of the DF 42 dams in the main tributaries and 3S rivers (see Arias, Piman, et al. (2014) for details).

^c To calculate flood occurrence, Arias, Piman, et al. (2014) used 15-years of simulations for 1986-2000 period, but this study uses 1-year of simulations driven by the climatological mean daily runoff for 1981-2010 period.

4.3.3.3. Potential Effects of Flow Regulation on Drying and Wet Seasons' River Discharge and Flood Occurrence in the LMRB

Because the effects of flow regulation on downstream flood patterns can vary significantly during dry and wet years, we examine the results for 1998 and 2000 (**Figure 4-13** and **Figure 4-14**), which represent the historical dry and wet years, respectively (Arias et al., 2012; Kummu & Sarkkula, 2008) (**Figure 4-4**, **Figure 4-7**). Although the broad spatial patterns of changes in flood occurrence during dry and wet years appear similar to those during the

average year (**Figure 4-11**), magnitudes vary, and some interesting features emerge. Substantially smaller (larger) flooded areas and occurrence can be seen during dry (wet) years (**Figure 4-13a,e**) compared to that in an average year (**Figure 4-11a**). Specifically, during the high flood season (August-October), 51.3% (36.9%) more (less) areas are flooded in wet (dry) years compared to the average year. Similarly, during the dry season (April-June), 17.1% (1.4%) more (less) areas are flooded in wet (dry) years. Further, for the 10% flow alteration scenario, marked differences are not found in downstream flood occurrence between dry, normal, and wet years. However, varying patterns of change in flood occurrence become readily discernable between dry and wet years for the 30%, and even more so for the 50% scenario. In the wet year, substantial areas in the western vicinity of the TSL experience an increase in flood occurrence by up to 6 months for 50% scenario, but the same region experiences a notable decline in flood occurrence during the dry year (**Figure 4-13d,h**). As in normal year (**Figure 4-11f**), a marked reduction in flood occurrence is seen in the outer extents of the major flooded areas around TSL (shown by magenta line) in both dry and wet years (**Figure 4-13d,h**). No change in flood occurrence that can be seen northwest of the TSL flooded areas in 50% scenario for 1998 (**Figure 4-13d**) is in fact due to no flood occurrence in all scenarios including the baseline (**Figure 4-13a**).

The effects of flow regulation on the seasonal flood dynamics (similar to **Figure 4-8**) during dry and wet years are presented in the **Figure 4-15** and **Figure 4-16**, along with the changes in different flood characteristics (**Table 4-5**, **Table 4-6**) for all flow alteration scenarios. Evidently, the peak flood magnitude decreases and the low flow increases, resulting in significantly dampened flood pulse amplitude in all Lower Mekong stations (**Table 4-6**). Notably, the TSR flow reversal tends to completely cease under 50% peak reduction scenario

during dry year (**Figure 4-15d-e**, **Table 4-5d-e**), which is likely also during the wet year if the flow under 50% peak reduction scenario is delayed by one month (**Figure 4-16 d-e**, **Table 4-6d-e**). The onset of TSR flow reversal tends to shift in the same direction and by a comparable duration to the duration of altered peak timing (i.e., one month) for 10% scenario but the effects are varying for 30% and 50% scenarios (**Table 4-3**, **Table 4-5**, **Table 4-6**). The other flood characteristics (e.g., duration and volume of reversed flow) are also affected to a considerably varying extent due to the alteration of timing under different scenarios of peak flow reduction (**Table 4-3**, **Table 4-5**, **Table 4-6**).

In the downstream of PP station (cyan rectangle in **Figure 4-13h**), as in the average year, substantial increase in flood occurrence is seen during the wet year (especially for >30% peak alteration scenarios) which is primarily due to a longer retention of water in these flat areas caused by increased low flow (**Figure 4-8g,h**) and higher dry-season water levels (**Figure 4-10g,h**). On the contrary, a significant reduction in flood occurrence can be seen in the upper portion of this region in the dry year because the relatively small increase in baseflow does not lead to a sustained flood water during the low flow season. In the areas upstream of PP station (green rectangle in **Figure 4-13h**), flooding is primarily caused by water overtopping river banks during wet season, thus the reduced flood peak causes a marked decline in flood extents and occurrence under all scenarios during both dry and wet years. Finally, within the region shown by a black rectangle (**Figure 4-13h**), a large decline in flood occurrence seen during a normal year (**Figure 4-11 b-f**) is not evident during the wet year (**Figure 4-13f-h**) because of significantly larger flows in the wet year even in the 50% regulation scenario (see **Figure 4-8** and **Figure 4-16**); in the dry year no change can be seen because this region is rarely flooded (**Figure 4-13a**).

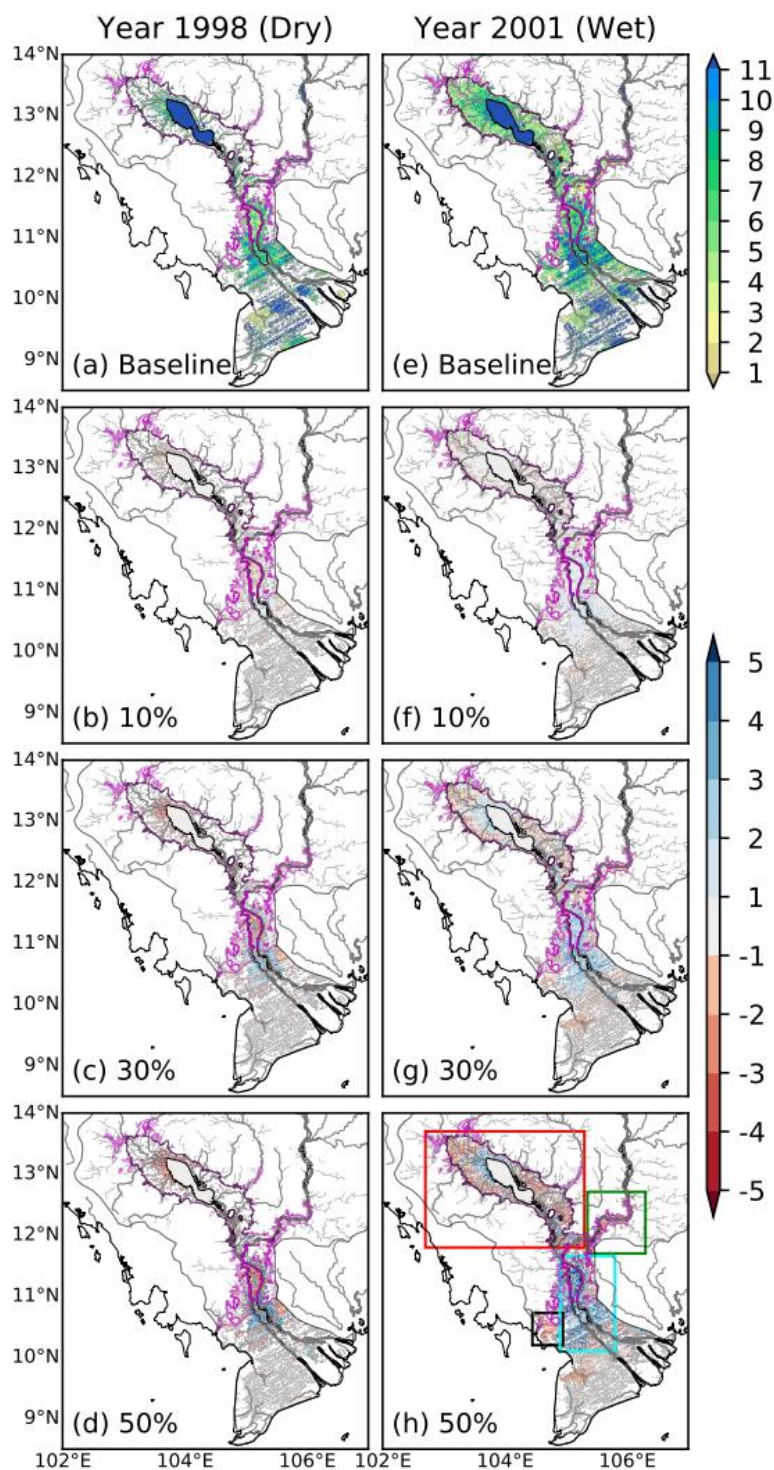


Figure 4-13 Same as in Figure 4-11 but for dry (1998) and wet (2000) years. For the altered flow scenarios, results for only 10, 30, and 50% alterations are shown. Rectangles in (h) show regions in the LMRB discussed in the text. For magenta and black lines, see description in Figure 4-4 caption.

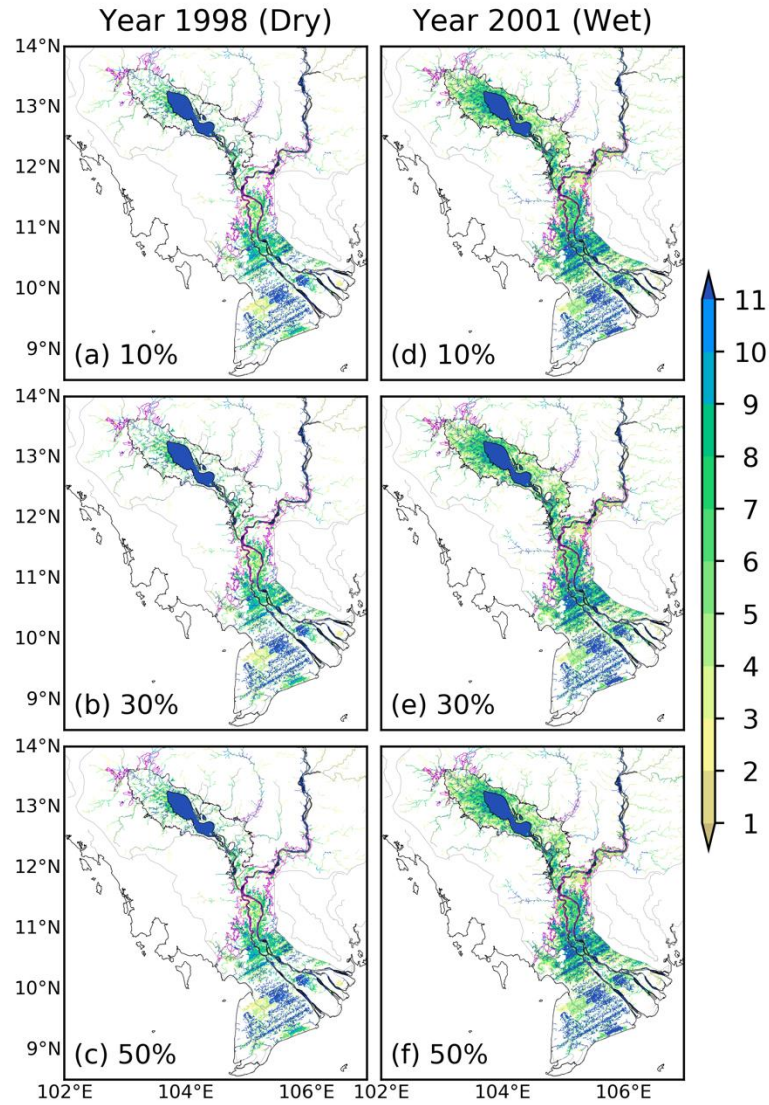


Figure 4-14 Simulated flood occurrence in dry and wet years for different flow regulation scenarios, i.e., the actual flood occurrence corresponding to the difference with the baseline shown in **Figure 4-13 b-d (1998) and **Figure 4-13 f-h** (2000).**

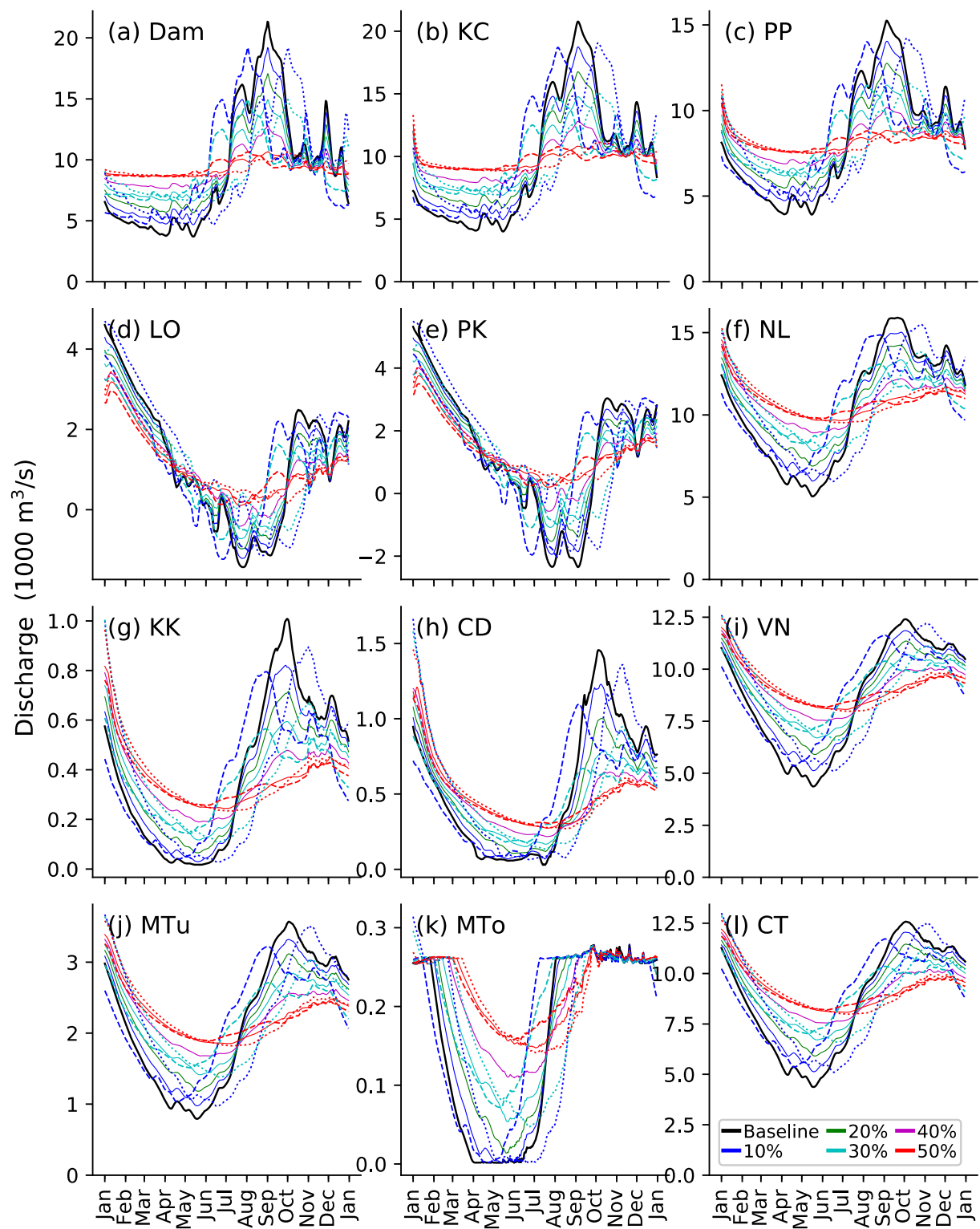


Figure 4-15 Same as in Figure 4-9 but for 1998 (dry year).

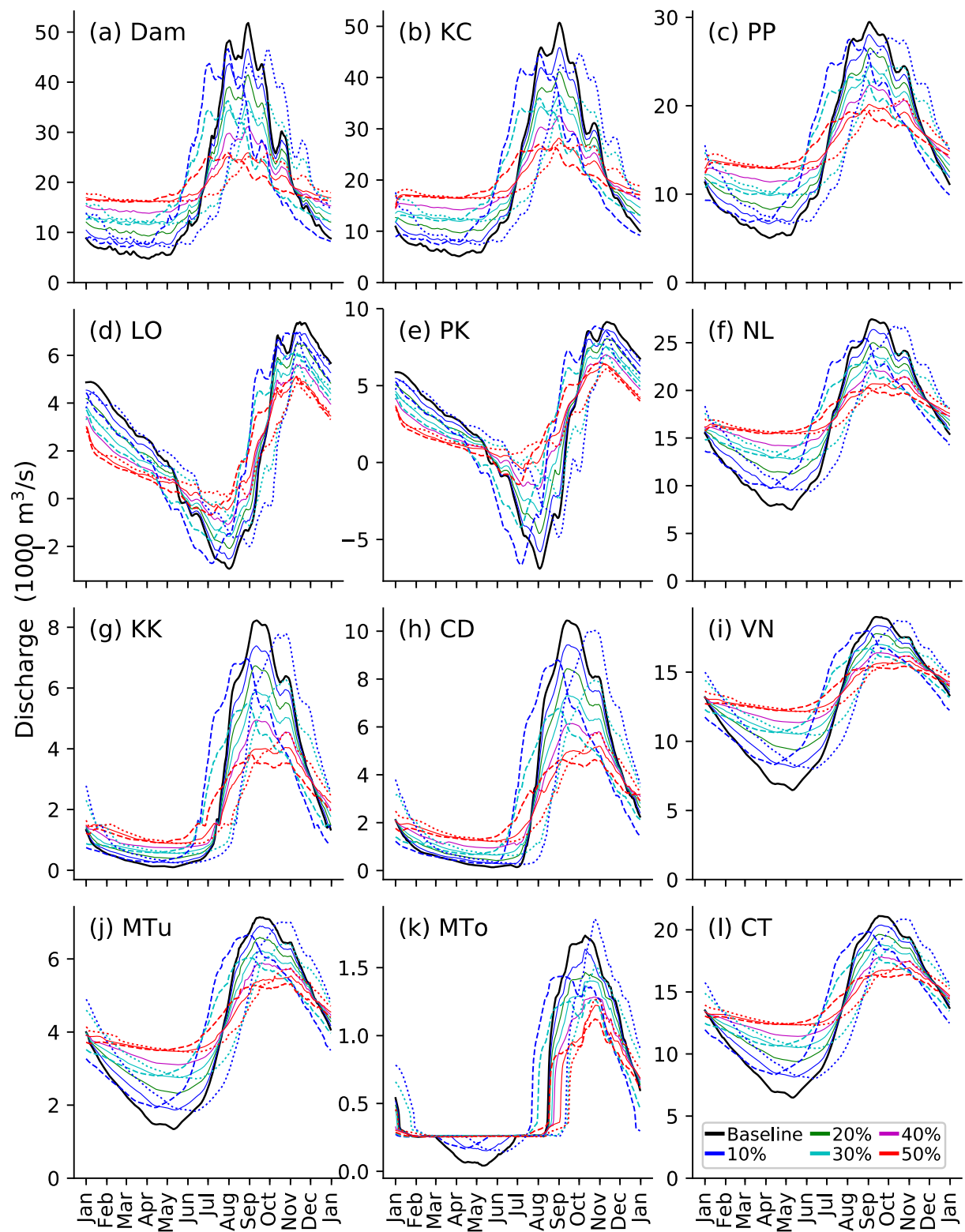


Figure 4-16 Same as in Figure 4-9 but for 2000 (wet year).

Table 4-5 Same as Table 4-3 but for dry year (1998). Blank fields in (d) and (e) denote no flow reversal.

(a) Q_{\max} in baseline (m ³ /s) and ΔQ_{\max} (%)													(b) Q_{\min} in baseline (m ³ /s) and ΔQ_{\min} (m ³ /s)												
Station	Baseline (m ³ /sec)	10%	10% Delay	10% Early	20%	30%	30% Delay	30% Early	40%	50%	50% Delay	50% Early	Station	Baseline (m ³ /sec)	10%	10% Delay	10% Early	20%	30%	30% Delay	30% Early	40%	50%	50% Delay	50% Early
Dam	21,327	-10	-10	-10	-20	-30	-30	-30	-40	-50	-50	-50	Dam	3,694	980	980	980	1,961	2,941	2,941	2,941	3,921	4,901	4,901	4,901
KC	20,775	-10	-8	-10	-19	-29	-27	-29	-38	-40	-36	-42	KC	4,005	955	933	996	1,916	2,886	2,860	2,921	3,848	4,826	4,800	4,876
PP	15,249	-8	-7	-8	-16	-25	-23	-25	-33	-29	-24	-31	PP	3,915	764	741	771	1,478	2,173	2,163	2,212	2,864	3,559	3,536	3,618
LO	4,597	-7	2	-16	-14	-21	-12	-28	-26	-31	-25	-36	LO	-1,429	220	286	197	455	708	777	691	1,017	1,529	1,591	1,560
PK	5,318	-7	3	-16	-13	-20	-10	-27	-25	-29	-24	-34	PK	-2,351	(-15%)	(-20%)	(-14%)	(-32%)	(-50%)	(-54%)	(-48%)	(-71%)	(-107%)	(-111%)	(-109%)
															407	506	317	827	1,270	1,384	1,257	1,785	2,552	2,663	2,598
															(-17%)	(-22%)	(-14%)	(-35%)	(-54%)	(-59%)	(-53%)	(-76%)	(-109%)	(-113%)	(-111%)
NL	15,904	-6	-3	-7	-11	-13	-5	-18	-10	-9	-4	-11	NL	5,045	933	898	1,184	1,840	2,785	2,677	3,219	3,858	4,601	4,479	4,743
KK	1,008	-19	-1	-21	-29	-27	0	-40	-22	-19	-4	-24	KK	16	13	12	24	49	101	93	128	174	228	218	240
CD	1,457	-16	14	-25	-26	-21	8	-39	-18	-17	0	-22	CD	29	40	36	53	78	122	106	150	189	244	241	269
VN	12,402	-4	2	-6	-7	-6	1	-12	-4	-3	0	-6	VN	4,359	764	735	990	1,544	2,339	2,233	2,649	3,176	3,707	3,615	3,829
MTu	3,571	-7	3	-10	-11	-9	2	-17	-7	-5	0	-9	MTu	792	185	178	242	390	622	591	719	887	1,061	1,029	1,102
MT0	278	0	13	-1	0	0	6	0	0	0	-1	0	MT0	2	0	0	0	12	52	45	70	108	146	140	156
CT	12,575	-4	3	-7	-7	-6	2	-11	-4	-3	1	-6	CT	4,367	762	734	988	1,541	2,342	2,232	2,647	3,179	3,706	3,615	3,833

(c) Q_{\max} - Q_{\min} in baseline (m ³ /s) and $\Delta(Q_{\max}$ - $Q_{\min})$ (%)													(d) Onset of reversed flow in baseline (day of year) and its change (day)												
Station	Baseline (m ³ /sec)	10%	10% Delay	10% Early	20%	30%	30% Delay	30% Early	40%	50%	50% Delay	50% Early	Station	Baseline (DOY)	10%	10% Delay	10% Early	20%	30%	30% Delay	30% Early	40%	50%	50% Delay	50% Early
Dam	17,634	-18	-18	-18	-35	-53	-53	-53	-71	-88	-88	-88	LO	159	2	32	-27	4	30	62	0	32	-	-	-
KC	16,770	-18	-16	-18	-35	-53	-51	-53	-71	-78	-73	-81	PK	162	0	30	-30	2	28	59	-1	30	-	-	-
PP	11,334	-17	-15	-18	-35	-52	-50	-53	-69	-70	-64	-74	(e) Duration of reversed flow in baseline (day) and its change (day)												
LO	6,026	-9	-3	-16	-18	-28	-22	-33	-37	-49	-46	-53	Station	Baseline (Days)	10%	10% Delay	10% Early	20%	30%	30% Delay	30% Early	40%	50%	50% Delay	50% Early
PK	7,669	-10	-4	-15	-20	-30	-25	-35	-40	-54	-51	-58	LO	103	-6	-9	-7	-15	-31	-32	-29	-48	-	-	-
NL	10,858	-17	-12	-20	-32	-45	-32	-56	-51	-55	-47	-60	PK	96	-5	-8	-3	-13	-27	-33	-25	-45	-	-	-
KK	992	-20	-2	-24	-34	-37	-10	-53	-39	-42	-26	-49	(f) Volume of reversed flow in baseline (10 ⁶ m ³) and its change (%)												
CD	1,428	-19	12	-29	-32	-30	1	-51	-31	-34	-17	-41	Station	Baseline (Mm ³)	10%	10% Delay	10% Early	20%	30%	30% Delay	30% Early	40%	50%	50% Delay	50% Early
VN	8,043	-16	-7	-22	-30	-38	-26	-51	-46	-51	-44	-56	LO	7,245	-22	-27	-16	-43	-65	-69	-60	-86	-100	-100	-100
MTu	2,779	-16	-3	-21	-29	-34	-19	-48	-41	-45	-37	-51	PK	12,180	-23	-30	-18	-46	-68	-74	-63	-89	-100	-100	-100
MT0	277	0	13	-1	-5	-19	-10	-26	-39	-53	-51	-57													
CT	8,208	-16	-4	-22	-30	-37	-24	-50	-45	-50	-43	-56													

Table 4-6 Same as Table 4-3 but for wet year (2000). Blank fields in (d) and (e) denote no flow reversal.

(a) Q_{\max} in baseline (m³/s) and ΔQ_{\max} (%)													(b) Q_{\min} in baseline (m³/s) and ΔQ_{\min} (m³/s)												
Station	Baseline (m³/sec)	10%	10% Delay	10% Early	20%	30%	30% Delay	30% Early	40%	50%	50% Delay	50% Early	Station	Baseline (m³/sec)	10%	10% Delay	10% Early	20%	30%	30% Delay	30% Early	40%	50%	50% Delay	50% Early
Dam	51,826	-10	-10	-10	-20	-30	-30	-30	-40	-50	-50	-50	Dam	4,733	2,266	2,266	2,266	4,532	6,798	6,798	6,798	9,065	11,331	11,331	11,331
KC	50,684	-10	-12	-12	-19	-28	-29	-29	-36	-44	-46	-47	KC	5,107	2,247	2,258	2,287	4,569	6,817	6,814	6,627	9,055	10,160	11,286	9,451
PP	29,477	-5	-6	-7	-10	-17	-17	-20	-24	-32	-30	-34	PP	5,042	1,610	1,555	1,776	3,233	4,794	4,760	4,898	6,338	7,835	7,806	7,313
LO	7,396	-6	-11	-6	-12	-18	-24	-17	-24	-31	-35	-31	LO	-2,935	410	931	226	850	1,349	1,787	1,174	1,852	2,461	3,007	2,247
PK	9,135	-6	-10	-3	-12	-18	-24	-15	-23	-30	-33	-29	PK	-6,902	(-14%)	(-30%)	(-4%)	(-29%)	(-46%)	(-61%)	(-40%)	(-63%)	(-84%)	(-102%)	(-77%)
NL	27,471	-4	-3	-7	-9	-14	-12	-16	-19	-25	-22	-26	NL	7,473	1,090	2,052	248	2,294	3,701	4,510	2,702	5,167	6,497	7,444	5,481
KK	8,222	-10	-5	-15	-18	-28	-24	-33	-40	-51	-45	-54	KK	99	(-16%)	(-30%)	(-4%)	(-33%)	(-54%)	(-65%)	(-39%)	(-75%)	(-94%)	(-108%)	(-79%)
CD	10,441	-10	-4	-16	-19	-30	-24	-35	-41	-50	-45	-56	CD	138	139	116	166	286	502	489	533	804	1,083	1,063	1,136
VN	18,999	-3	-1	-5	-6	-10	-8	-12	-14	-17	-15	-19	VN	6,466	1,652	1,546	1,862	2,914	4,047	3,980	4,153	4,889	5,685	5,668	5,756
MTu	7,140	-3	-2	-7	-8	-13	-10	-16	-18	-22	-20	-25	MTu	1,342	522	487	590	982	1,406	1,379	1,452	1,763	2,123	2,113	2,155
MTo	1,737	-6	7	-17	-16	-19	-13	-27	-26	-30	-27	-35	MTo	41	111	102	125	213	213	213	214	214	213	213	213
CT	21,128	-3	-1	-6	-7	-11	-9	-13	-16	-20	-17	-22	CT	6,484	1,654	1,542	1,857	2,904	4,032	3,959	4,146	4,932	5,858	5,837	5,900
(c) $Q_{\max} - Q_{\min}$ in baseline (m³/s) and $\Delta(Q_{\max} - Q_{\min})$ (%)													(d) Onset of reversed flow in baseline (day of year) and its change (day)												
Station	Baseline (m³/sec)	10%	10% Delay	10% Early	20%	30%	30% Delay	30% Early	40%	50%	50% Delay	50% Early	Station	Baseline (DOY)	10%	10% Delay	10% Early	20%	30%	30% Delay	30% Early	40%	50%	50% Delay	50% Early
Dam	47,094	-16	-16	-16	-32	-47	-47	-47	-63	-79	-79	-79	LO	141	6	32	-21	7	11	35	-17	14	34	-	6
KC	45,577	-16	-18	-18	-31	-46	-48	-47	-60	-72	-76	-73	PK	143	5	33	-21	7	10	41	-18	14	36	-	5
PP	24,436	-12	-14	-15	-25	-40	-40	-45	-55	-70	-68	-71	(e) Duration of reversed flow in baseline (day) and its change (day)												
LO	10,332	-8	-17	-7	-17	-26	-35	-24	-35	-46	-54	-44	Station	Baseline (Days)	10%	10% Delay	10% Early	20%	30%	30% Delay	30% Early	40%	50%	50% Delay	50% Early
PK	16,037	-10	-19	-3	-21	-33	-42	-25	-45	-58	-66	-51	LO	114	-8	-7	-6	-12	-21	-32	-14	-28	-66	-	-45
NL	19,998	-16	-14	-21	-31	-46	-44	-50	-60	-74	-70	-76	PK	111	-7	-13	-7	-13	-23	-57	-14	-53	-80	-	-60
KK	8,123	-12	-7	-17	-22	-34	-29	-40	-48	-61	-55	-64	(f) Volume of reversed flow in baseline (10 ⁶ m³) and its change (%)												
CD	10,303	-11	-5	-18	-22	-35	-29	-41	-50	-61	-56	-67	Station	Baseline (Mm³)	10%	10% Delay	10% Early	20%	30%	30% Delay	30% Early	40%	50%	50% Delay	50% Early
VN	12,532	-18	-15	-23	-33	-48	-44	-51	-60	-71	-68	-74	LO	15,181	-18	-40	-7	-38	-57	-75	-46	-75	-92	-100	-86
MTu	5,798	-13	-11	-19	-26	-40	-36	-44	-52	-64	-61	-69	PK	31,642	-20	-49	-3	-42	-63	-85	-46	-82	-99	-100	-89
MTo	1,696	-12	1	-25	-29	-32	-26	-41	-39	-43	-40	-49													
CT	14,644	-16	-12	-21	-30	-43	-40	-47	-56	-68	-65	-72													

4.4. Summary and Conclusion

River-floodplain water storage is found to play a crucial role in modulating the hydrology of the MRB. Potential upstream flow regulations could disrupt the natural flood dynamics in the TSL region and Mekong Delta. Results indicate that the river-floodplain water explains ~26% of the total storage dynamics in the MRB and ~49% in the LMRB, suggesting that the potential flow alterations can largely modify the natural regime of the Lower Mekong hydrology. It is found that the reduction in the peak of flood pulse by more than 20% near Stung Treng gauging station could cause a significant alteration on the water balance of the TSL, potentially ceasing the flow reversal in the TSR and disrupting the lake flood dynamics, if the flood peak at the same location is dampened by 50% and delayed by one-month. During average and wet years, flood occurrence is likely to increase at the outer fringe of the permanent water in the TSL and post-flooding agricultural regions in the middle reach of the Mekong Delta; however, during dry years flood occurrence could reduce by up to 5 months or more around the outer edge of the flooded areas in the TSL region, in the flood-recession agricultural region at the vicinity of the Mekong upstream of Phnom Penh, and downstream portion of the Mekong delta. Further, while areas flooded for less than five months and over six months are likely to be impacted significantly by flow regulations, areas flooded for 5-6 months could be impacted the least. These results provide new insights about how the downstream flood dynamics could change under different levels of upstream flow regulation by proposed dams, which have important implications for sustainable hydropower development to ensure food security and ecological integrity in the Mekong region.

Chapter 5. Impact of Manmade Reservoirs on Mekong River Basin Hydrology over the Past Years

5.1. Introduction

In this chapter, historical flood dynamics of the entire Mekong River Basin (MRB) is simulated at fine resolution grids (i.e., ~5km) with explicit representation of inundation dynamics of individual reservoirs. While Chapter 4 mainly dealt with the investigation of the cumulative effect of upstream flow regulation on the flood dynamics in the specific regions, i.e., the Mekong Delta and Tonle Sap Lake (TSL), the goal in this chapter is to model the operation of individual reservoirs and the consequent changes in flood dynamics over the entire MRB.

The understanding of flood inundation dynamics in the entire MRB is currently limited. Studies based on observations have identified that there are shifts in flow patterns after some dams have been built (e.g., Arias, Cochrane, et al., 2014; Räsänen et al., 2012; Sabo et al., 2017; W. Wang et al., 2017); however, these studies have not considered the inundation extent dynamics due to data limitations. There has been an increase in model-based studies in the past decade; however, these studies have focused on some parts of the MRB such as the UMRB (e.g., Räsänen et al., 2012), LMRB (e.g., Dang et al., 2018; Trung et al., 2018), 3S-river basin (e.g., Wild & Loucks, 2014), Mun river basin (e.g., Akter & Babel, 2012), and TSL and the Mekong Delta region (Minh et al., 2019; A. Smajgl et al., 2015). There are some modeling studies for the entire MRB (e.g., Lauri et al., 2012; Piman et al., 2013; Sridhar et al., 2019; W. Wang et al., 2016), but to the author's best knowledge, none of those have simulated the inundation dynamics of both natural river-floodplain and manmade-reservoirs over the entire MRB. A recent and notable study is by Bonnema and Hossain (2017) that used a 0.1° VIC model over the MRB to derive the time series inflow into some reservoirs in the MRB. The inundation of individual

reservoirs was of interest in their study, hence the inundation over the other parts of natural river-floodplain was not simulated.

As such, while there is an increasing body of literature on the hydrologic changes in different parts of the MRB, there is a lack of an integrated study that holistically and explicitly simulates the natural and human-induced changes in flood dynamics over the entire basin. The goal of this study is to fill this gap by using a newly integrated river-floodplain-reservoir hydrodynamics model for the entire MRB. We address the following research questions:

“Q5. How have the flood dynamics and surface water storage in the MRB changed over the past four decades?”

“Q6. Are the effects of dams significant compared to that of climate variability?”

“Q7. What will be the role of existing reservoirs in modulating surface water storage and inundation dynamics over the MRB in the future?”

We answer these questions by simulating the historical dynamics of river-floodplain-reservoir storages over the entire MRB for the period of 1979-2016 and at a spatial resolution of 3-arcmin (5 km). The simulated flood extent is downscaled to a further finer resolution of 3-arcsec (90 m) to investigate the fine-scale inundation extent and patterns. Such high-resolution and large-scale modeling is accomplished by integrating a newly developed reservoir scheme (Chapter 3) into a global river-floodplain hydrodynamics model CaMa-Flood (D. Yamazaki et al., 2013) over the MRB. Simulations of river discharge and water level are validated with ground-based observations and those of river-floodplain-reservoir inundation dynamics with state-of-the-art remote sensing products. The newly integrated model simulates reservoirs as an integral part of river-floodplain systems in high-resolution and over large domains, making it

suitable for investigating the changing hydrology of the Mekong river where natural hydrologic processes currently dominate river-floodplain hydrodynamics but the influence of dams is increasing at an unprecedented rate.

5.2. Materials and Methods

5.2.1. CaMa-Flood and HiGW-MAT models

In the Chapter 5, we use CaMa-Flood version-3.94 which includes major updates to the previous version used in Chapter 4. The spatial resolution is set to 3-arcmin (5km) with the capability to downscale simulated flood depth to 3-arcsec (90m) resolution. For an improved representation of channel bifurcation and the processes therein (D. Yamazaki et al., 2014)—which are critically important in the LMRB—the maximum number of bifurcation channels is increased from 6 to 10 compared to that in Chapter 4. The previously used SRTM DEM (Shuttle Radar Topography Mission DEM) has been suggested to have multiple errors including absolute bias, stripe noise, speckle noise, and tree height bias (D. Yamazaki et al., 2017). Here we use MERIT DEM (Multi-Error-Removed Improved-Terrain DEM; Yamazaki et al., 2017) and MERIT Hydro (D. Yamazaki et al., 2019) in which those errors have been resolved such that the stripe-like artifacts in simulated flood extents found in low-relief areas, specifically in the Mekong Delta region (Chapter 4), are eliminated. These advancements are essential for a more realistic simulation of river-floodplain dynamics in the MRB. In addition, a new reservoir inundation and release scheme has been incorporated into the modeling framework (details in Chapter 5.2.4 and 5.2.5).

CaMa-Flood is fed by the runoff simulated by HiGW-MAT (Y. N. Pokhrel et al., 2015), which is a global hydrological model based on the land surface model (LSM) called the MATSIRO (Takata et al., 2003). HiGW-MAT simulates both the natural water cycle and human activities from canopy to bedrock including evapotranspiration, infiltration, irrigation, flow regulation, and groundwater pumping on a full physical basis. In this study, we use HiGW-MAT in the natural setting (i.e., the human impact schemes are turned off) as done in Chapter 4

because the objective is to provide runoff as input to CaMa-Flood and reservoirs are simulated within CaMa-Flood (see Chapter 5.2.6).

5.2.2. Dams and Reservoirs database

The specifications (e.g., location, dam purpose, commissioned year, dam dimensions, storage capacity, power generation capacity, etc.) of existing, under construction, and planned dams (455 in total) within the MRB are obtained from the Research Program on Water, Land, and Ecosystem (WLE; <https://wle-mekong.cgiar.org/>). However, the WLE database contains significant omissions (e.g., missing attributes), and sometimes, errors. For example, of the 455 dams, only 128 and 173 include information on storage capacity and height, respectively. Since the direct employment of erroneous dam specifications results in erroneous hydrodynamics modeling, all missing and erroneous specifications should be carefully curated to yield reasonable model results for validation against satellite-based datasets such as the Global Surface Water (GSW) data (Pekel et al., 2016).

In this study, the dams that existed as of 2016 (end of simulation period constrained by the availability of WFDEI forcing data; see Chapter 5.2.6) are imported to the CaMa-Flood modeling framework when they satisfy at least one of the following criteria: (1) dam height $\geq 15\text{m}$, (2) storage capacity $> 1 \text{ million m}^3$ (Mm^3), and (3) installed hydropower capacity > 100 Mega Watts (MW). The first criterion is commonly used to classify large dams (e.g., International Commission on Large Dams (ICOLD); (Binnie, 1987; Greathouse et al., 2006; Räsänen et al., 2017). The second criterion is set since small inundation extents are found in satellite images for dams having a height of $< 15 \text{ m}$ and a storage capacity $< 1 \text{ Mm}^3$. When the first and second criteria are applied, most of hydropower dams, even those with installed

hydropower capacity in the single-digit (in MW), are included. However, there were some large hydropower dams (in terms of installed capacity) for which dam height and storage values were missing, hence we additionally set the third criterion of 100MW. We fill the missing values from various resources including published reports from the Mekong River Commission (MRC; <http://www.mrcmekong.org>), Project Design Documents (PDD) provided by Clean Development Mechanism (CDM) of United Nations Framework Convention on Climate Change (UNFCCC) (<https://cdm.unfccc.int>), documents from construction and design companies, and other peer-reviewed literature. These resources are also used to correct any erroneous records in the dam specification database. As a result, 86 dams are selected (Figure 5-1).

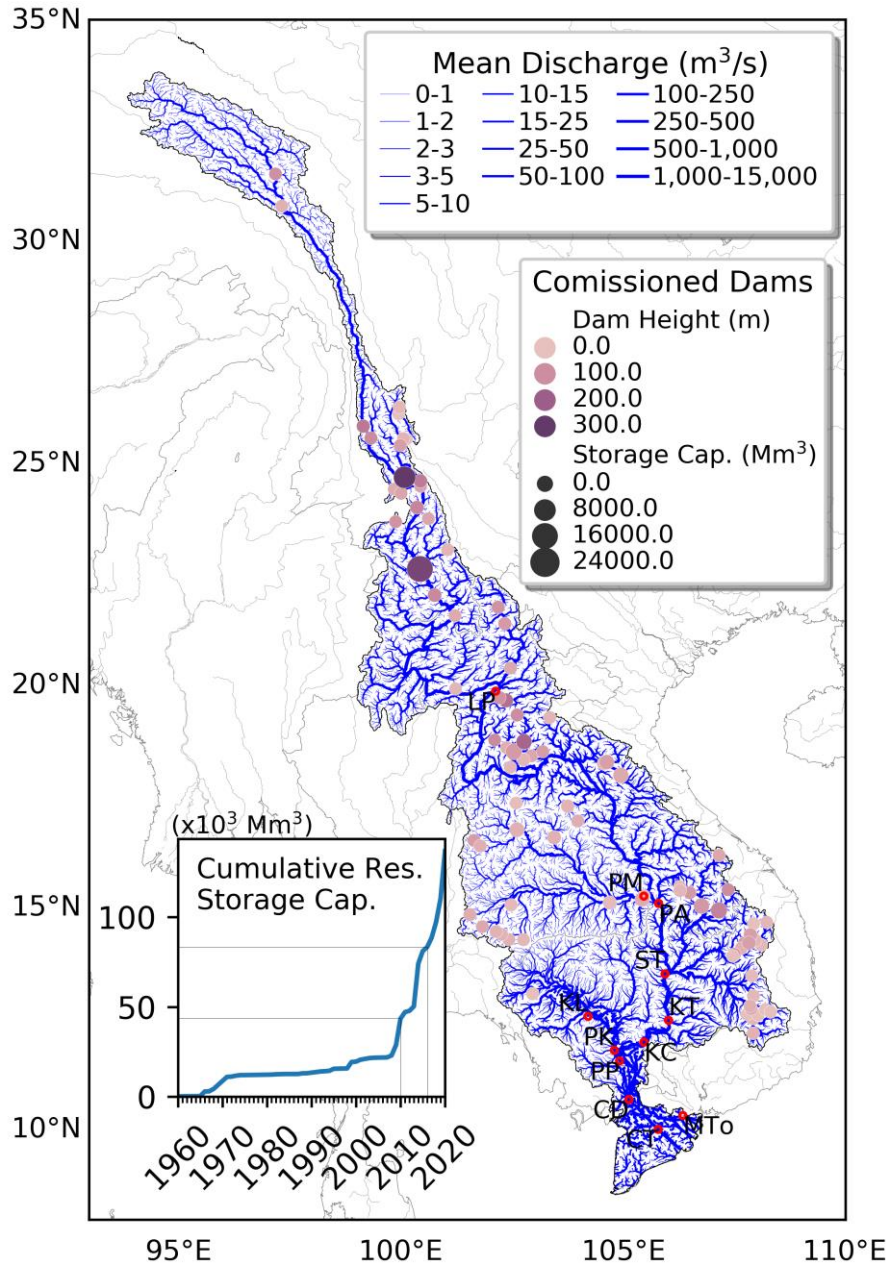


Figure 5-1 The spatial distribution of river discharge and commissioned dams (as of 2016) over the MRB. The background shows the simulated long-term mean river discharge (1979-2016; 5-km grids). The filled circles show the height and storage capacity of 86 dams with varying color and size, respectively. The cumulative reservoir storage capacity from 1960 through 2020 is shown as a subplot on the lower-left corner with the highlights on the values of 2010 and 2016. The hydrological gauging stations are displayed as red hollow circles. Station names are: LP (Luang Prabang), PM (Pak Mun), PA (Pakse), ST (Stung Treng), KT (Kratie), KC (Kampong Cham), PK (Prek Kdam), PP (Phnom Penh Port), CD (Chau Doc), CT (Can Tho), KL (Kompong Luong), and MT (My Tho).

5.2.3. Observed Data for Model Validation

The MRC provides the observation data for river discharge and water level. Among the observation stations, 10 stations for each variable either having several years of record or those located near river confluences are selected (**Table 5-1**). For the validation of inundation extent, we use two remote sensing products: Global Surface Water (GSW) data (Pekel et al., 2016) based on Landsat imagery and our own water body detection products from Sentinel-1. For the selected regions that include the TSL, natural river-floodplain regions, and top 16 reservoirs (selected by considering top 10 reservoirs in height, storage capacity, and surface inundation area, respectively), the remote-sensing based flood occurrence is used to validate the simulated flood occurrence. The GSW flood occurrence data are provided for the 1984-2018 period, which is different from CaMa-Flood simulation period, i.e., 1979-2016; however, the discrepancy is expected to be acceptable since 38- and 35-years timespans of CaMa-Flood simulation and GSW data overlap for 33 years. For the Sentinel-1 based products, the comparison is done only for the overlapping period (i.e., 2014-2016). To validate the simulated flooded areas over the entire basin, we also utilize the GSW monthly water extent; specifically, the time series of total flooded areas over the entire MRB from GSW and CaMa-Flood are compared.

Table 5-1 Observation stations of the Mekong River Commission

Names		Use for validation		Location	
Abbreviation	Full Name	Discharge	Elevation	Latitude	Longitude
LP	Luang Prabang	O	O	19.892	102.137
PM	Pak Mun	O	O	15.282	105.468
PA	Pakse	O	O	15.117	105.800
ST	Stung Treng	O	O	13.533	105.945
KT	Kratie	O	O	12.487	106.024
KC	Kompong Cham	O	O	11.997	105.470
KL	Kompong Luong		O	12.575	104.215
PK	Prek Kdam	O		11.813	104.804
PP	Phnom Penh Port	O	O	11.575	104.923
CD	Chau Doc	O		10.705	105.133
CT	Can Tho	O	O	10.033	105.790
MTo	My Tho		O	10.345	106.347

5.2.4. Incorporation of Reservoirs into CaMa-Flood

When it comes to importing dams into a gridded hydrodynamic model, there are two important issues to be considered. First, the maximum water depth can be lower than the dam height provided in the dam database. It can be because of prevalent errors in the database or due to the mixed definition and usage of dam height (i.e., dam structure height or the maximum water storage depth). Second, as discussed in detail in Chapter 2, DEM grid elevations represent the water surface level, not the river-reservoir bed elevation. When the pre-existing water depth is large, the deviations between the bed elevation and the DEM-based elevation can be too large to be ignored (Chapter 2.2.2). Specifically, when large dams are constructed before the DEM is produced, such discrepancies can be relatively large. The above-mentioned issues exist even when a high-resolution DEM (e.g., MERIT DEM) is used. Our examination of the dams in the MRB using two 3-arcsec global DEMs, namely the MERIT and HydroSHEDS, reveals that most of reservoirs need considerably lower level of water impoundment than their dam heights (**Figure 5-2**). The MERIT DEM, which is employed in this study, shows less deviations from the recorded dam height than the HydroSHEDS DEM does (vertical lines in **Figure 5-2**), likely

owing to more realistic representations of ground elevations by multiple errors corrections in MERIT DEM.

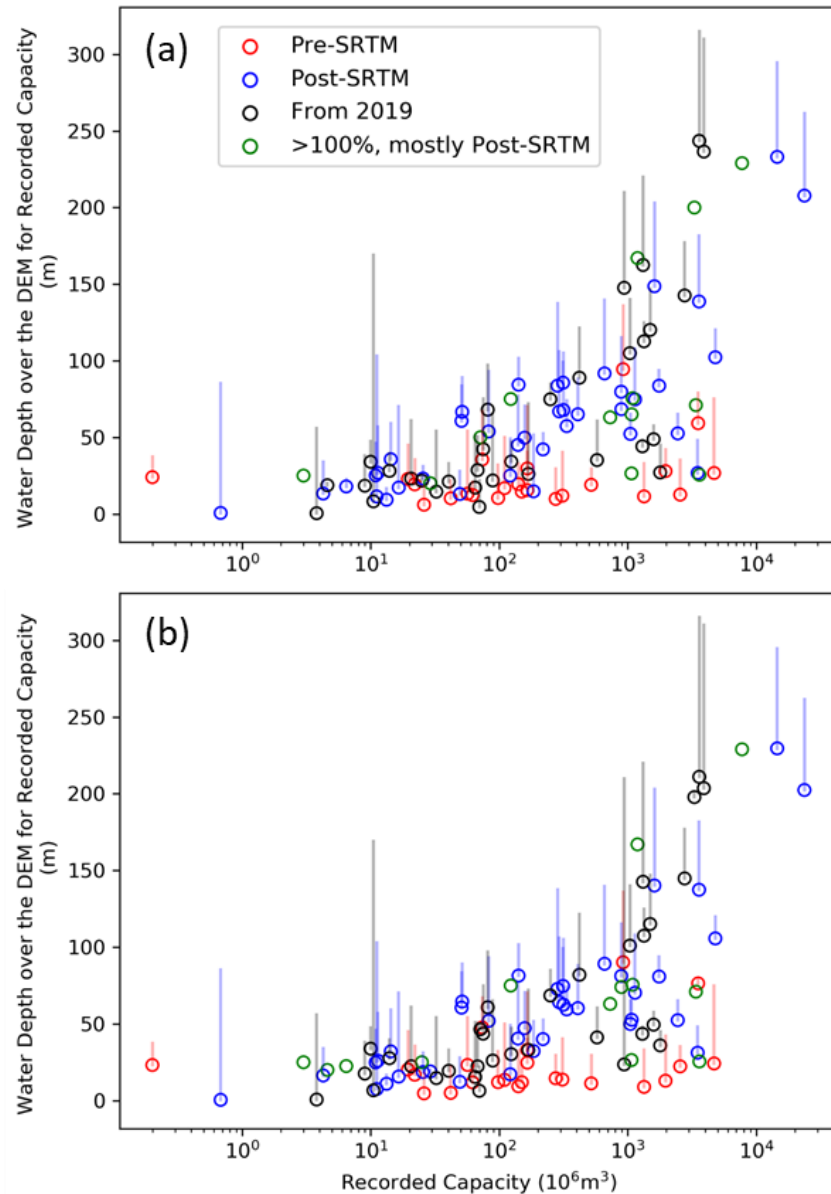


Figure 5-2 Deviation at 3-arcsec grids from dam crest level to water level to achieve recorded storage capacity for (a) the MERIT and (b) HydroSHEDS DEMs. Vertical lines indicate the deviations.

When dams are located on the river network of raster model grids, a simple conversion of the latitude and longitude information into the model grid coordinates can cause a dislocation of dams that can lead to erroneous modeling results; for example, some dams in the tributaries can be wrongly located in the mainstem which may cause an unusually high dam inflow and outflow, and vice versa (Chapter 2.2.2). Accurately locating dams is also important for realistic representation of inundation patterns since the upstream inundation starts from dam locations. The approach in Chapter 2.2.2, i.e., fine-tuning the reservoir location in the model grid to the grid cell having the most similar upstream basin area to the known value, cannot be used since the reference data for reservoir's upstream basin area is not available. To overcome the limitation, dam locations in 3-arcsec river network are first determined as the nearest river cells from the given latitude and longitude. Then, the upstream basin area in 3-arcsec grid DEM is used as a reference for locating the dams into 3-arcmin model grid.

Of the 86 selected dams, dam height and storage capacity information was missing for 9 and 17 dams, respectively. For the other 60 dams having both attributes, we find the ratio between database dam height and the maximum water level (i.e., water depth at the dam location to achieve recorded storage capacity) to be ~70% (**Figure 5-3**). Based on this finding, the maximum water level for the 9 dams is set at 70% of the dam height reported in the database. The storage capacities of the 17 dams are estimated as the storage when the water level at the dam location reaches 70% of the reported dam height. The inundation extents at those levels are found to be reasonable in the visual inspections with GSW data.

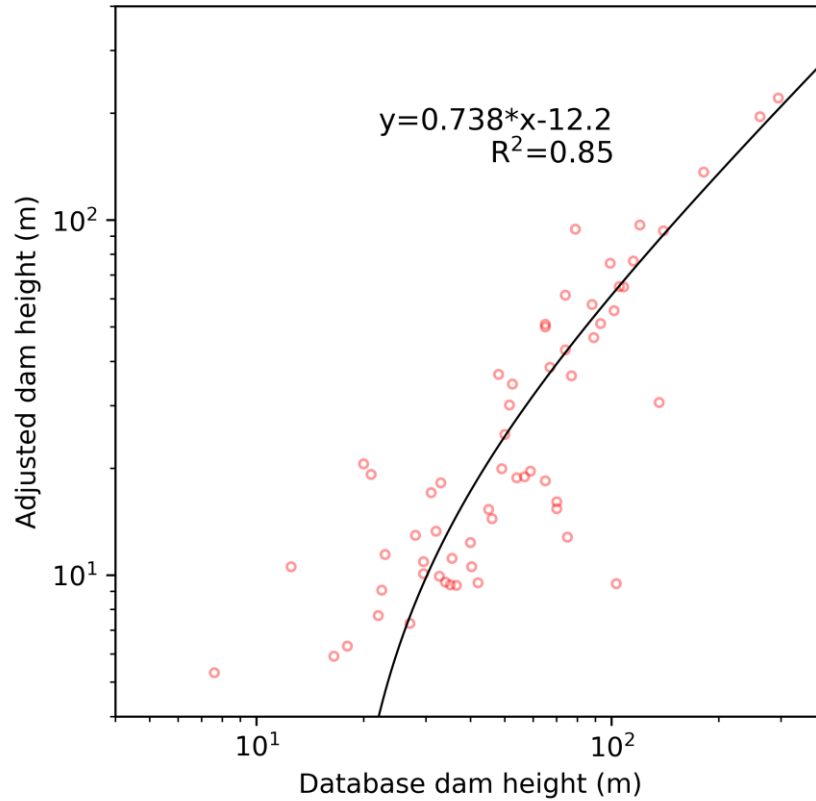


Figure 5-3 Relationship between dam height in the database and adjusted dam height at 3-arcmin CaMa-Flood modeling grids based on the MERIT DEM

5.2.5. Reservoir Operation Scheme

The 86 selected dams in the MRB can be classified into three general categories based on their purpose reported in the database: irrigation (22), hydropower (62), and multi-purpose (2). We use the reservoir operation scheme in Chapter 3.2.1 for irrigation dams, which determines the seasonality of reservoir release by utilizing the water demand in a region and an optimization scheme that maximizes hydropower generation for hydropower and multi-purpose dams. Details about the demand-driven scheme can be found in Chapter 3.2.1.

The reservoir operation scheme in Chapter 3.2.1 can also be applied for reservoirs with any other purposes than irrigation if the seasonal water demands for that purpose are available. However, since the seasonal water demand data or proxies are not available for hydropower

production in the MRB, we use an optimization approach for hydropower reservoirs. Hydropower reservoir operation can be formulated as an optimization problem that maximizes hydropower benefit, F [\$] as:

$$F = \sum_{t=0}^T P(t) \cdot W(t) \cdot \Delta t = \sum_{t=0}^T P(t) \cdot \eta \cdot \gamma \cdot \min(Q(t), Q_{turbine}) \cdot H(t) \cdot \Delta t \quad (1)$$

where $P(t)$ is electricity price [\$/Watts-hour], $W(t)$ is the generated electrical energy [Watts] during unit time span of Δt [hr], η is efficiency [-], γ is specific weight of water [kg/m³], $Q(t)$ is the reservoir release (m³/s), $Q_{turbine}$ is the turbine design flow (m³/s), and $H(t)$ is turbine head [m]. Since no data are available on $P(t)$, which is a rather complicated function of demand and supply and various other variables (Aggarwal et al., 2009; Weron, 2014), we assume constant $P(t)$ over time. Consequently, the optimization problem is simplified to maximize the total energy production. Such simplification can ignore the inundation variability in small time scales (e.g., diurnal and weekly), specifically near local reservoir areas; however, such small-scale variations are expected to be averaged out as the size of the domain of interest (i.e., the entire MRB) and the time scale (i.e., monthly) become greater.

In addition to the maximization of F , we also consider a common practice in hydropower management that stores as much as water in low-demand and wet seasons and releases water gradually to be prepared for high-demand and dry seasons. Such practice can be formulated to minimize the variation of reservoir storage (σ_{STOR}). In achieving two objectives of hydropower reservoir operation, the maximization of F is assumed to precede the minimization of σ_{STOR} . In other words, after estimating the total discharge amount through turbine (i.e.,

$\sum_{t=0}^T \min(Q(t), Q_{turbine}))$ that maximizes F , the identical amount is redistributed without additional

spillway discharge to make σ_{STOR} the minimum under the constraints of reservoir storage capacity and time-varying inflow $In(t)$. To avoid the excessive computational cost in the optimization from the iterative hydrodynamic model running, we optimize the reservoir operation using the approach in Chapter 3.2.3 that employs simulated river discharge without considering dams in optimization (or calibration) of parameters in reservoir operation scheme. Using the approach in Chapter 3.2.3, the optimized reservoir releases are sequentially calculated from the uppermost to lowermost reservoirs, firstly to maximize F , and secondly to minimize σ_{STOR} .

From the aforementioned data sources (Chapter 5.2.3), $Q_{turbine}$ for 12 dams are obtained. The WLE database does not provide information on $Q_{turbine}$, but the installed energy capacity W_{max} is available. For a given W_{max} , $Q_{turbine}$ can be calculated as $W_{max} / (\eta \cdot \gamma \cdot Q_{turbine} \cdot H_{max})$, where H_{max} is the maximum available head. The only available proxy of H_{max} is the dam height, however, equating the dam height to H_{max} could yield too large $Q_{turbine}$ since, in many cases, turbines are located at further downstream (i.e., lower) locations from dam locations to obtain high water heads (**Figure 5-4**). For this reason, we employ the streamflow with 30% probability of exceedance (i.e., Q_{30}) as $Q_{turbine}$, which has been widely employed in the previous global studies (Gernaat et al., 2017; Hoes et al., 2017; Y. Zhou et al., 2015). To examine the uncertainty caused by the choice of exceedance probability, the simulations using Q_{20} and Q_{40} are also set up (Chapter 5.2.6) for a sensitivity analysis purpose. Those three flow exceedances are found to

reasonably approximate $Q_{turbine}$ (Figure 5-5) and are also closely related to the long-term average flow (Figure 5-6).

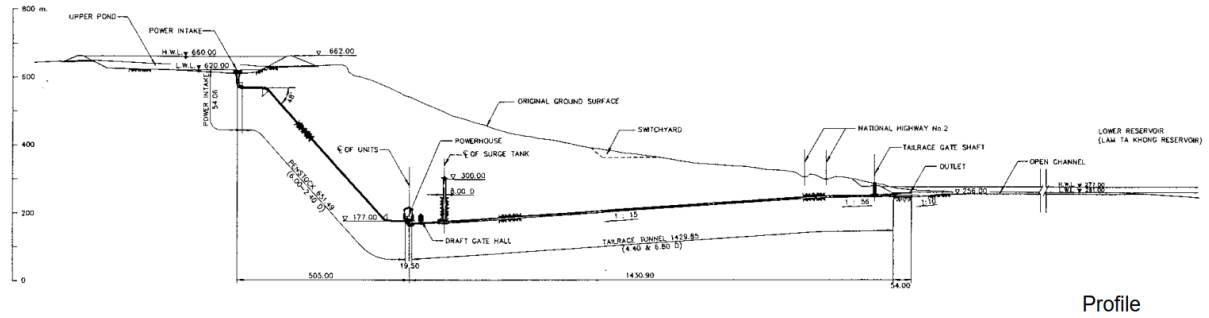


Figure 5-4 The profile of Lam Ta Khong P.S. dam. The dam height and maximum water depth are 42 m and 40 m, respectively, and the head difference before and after turbine is 360 m.

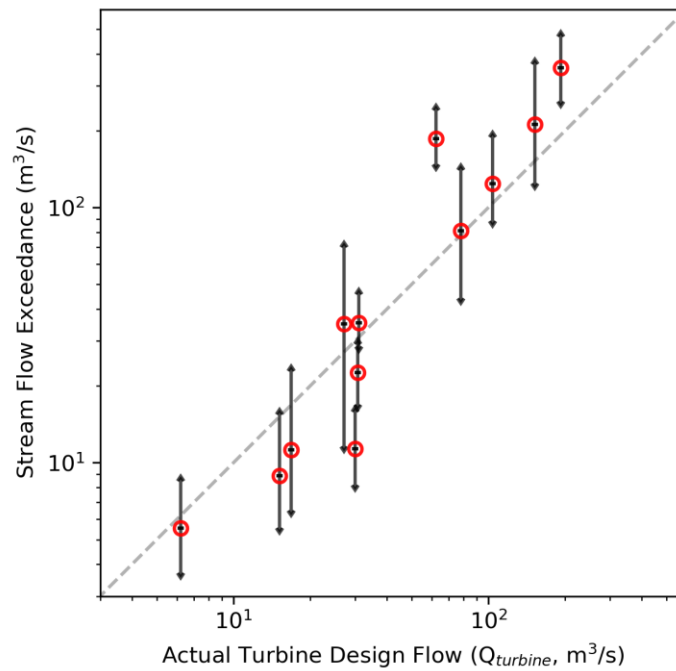


Figure 5-5 Comparison of turbine design flow and 20% (Q_{20}), 30% (Q_{30}), and 40% (Q_{40}) stream flow exceedances for 12 reservoirs. Red circles indicate Q_{30} , and the upper and lower bounds indicate Q_{20} and Q_{40} , respectively. A diagonal dashed line represents 1:1 line.

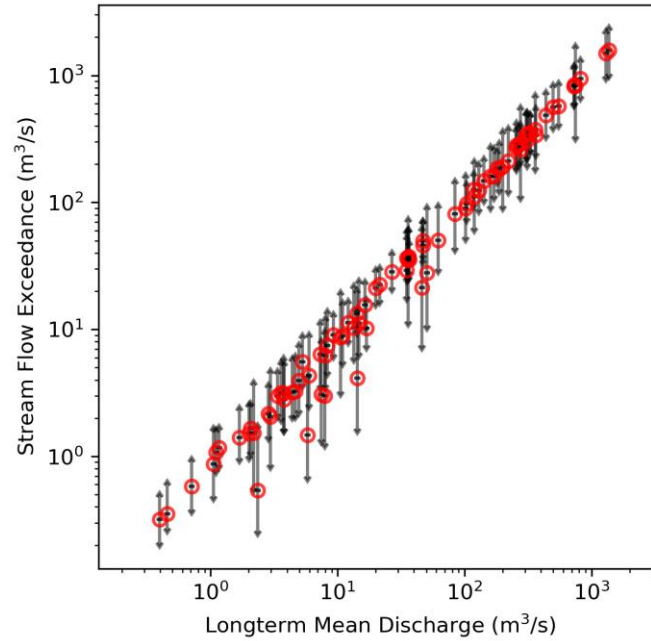


Figure 5-6 Mean discharge and stream flow exceedances for 86 reservoirs. Red circles indicate Q_{30} , and the upper and lower bounds indicate Q_{20} and Q_{40} , respectively.

While the real-world reservoir operation rule can be complicated, no information is publicly available for any of the reservoirs in the MRB; hence any model development in the MRB has to rely on a generic reservoir scheme that may not fully account for the complex dynamics in the actual operation rules. Another challenge is the validation of reservoir release and storage because observed river discharge is generally not available at locations immediate downstream of many of the reservoirs, and storage measurements are not available for any of the reservoirs in the MRB. Thus, to consider the uncertainties in reservoir operation schemes and data, we additionally consider two hypothetical hydropower reservoir operation modes, following a similar approach employed by Piman et al. (2013): full-level and low-level. Full-level operation maintains the water level up to the maximum level and releases the surplus water through turbines or spillway. Low-level operation releases $Q_{turbine}$, which can be Q_{20} , Q_{30} , or Q_{40} ,

so long as the reservoir water level is above the minimum level. From the contrasting operation policies of these two extremes, we intend to simulate the probable maximum changes in inundation extent (full-level operation) and river discharge (low-level operation). Conversely, the probable minimum changes in inundation extent and river discharge are simulated by low-level and full-level operations, respectively.

5.2.6. Simulation Settings

HiGW-MAT is run for 1979-2016 period for which the WFDEI forcing data are available, and the runoff from HiGW-MAT is used as the input for CaMa-Flood model. With different settings for reservoirs, 15 simulations are conducted that are categorized into three groups: NAT, HIST, and ALL (**Table 5-2**). NAT is a simulation with natural river-floodplain settings that simulates surface water dynamics without considering reservoirs. To assess the impact of reservoirs on MRB hydrology, NAT is compared with the historical simulations of river-reservoir-floodplain dynamics (HIST). HIST simulations use the reservoir operation scheme of Chapter 3.2.1 for irrigation reservoirs and optimized (opt), full-level (full), and low-level (low) operation schemes (details in Chapter 5.2.5) for hydropower reservoirs. The use of different hydropower operation schemes is intended to provide the upper and lower bounds of changes under the uncertainty in reservoir operation. HIST simulations are grouped into HIST-opt, HIST-full, and HIST-low, and are further detailed according to the setting of $Q_{turbine}$ using Q_{20} , Q_{30} , and Q_{40} . In addition, to estimate the probable impact of the existing 86 dams, we set up ALL simulations, which is designed to investigate the difference in hydrodynamic responses of the Mekong river with and without the newly built reservoirs. To make ALL simulations comparable to NAT and HIST simulations, the same WFDEI forcing data and HiGW-MAT runoff are used for ALL simulations as well. The main difference is the start timing of reservoir

operation in which all 86 dams are assumed to exist from 1979. That is, in ALL simulations the operation of all 86 dams begins from 1979 regardless of the year each dam is historically commissioned. Other than the start year of reservoir operation, the modeling settings of ALL simulations (e.g., runoff time series; reservoir operation modes; $Q_{turbine}$) are identical to those of HIST simulations.

Table 5-2 Simulation settings

	Reservoir operation	Irrigation reservoir operation scheme	Start year of reservoir operation	Hydropower reservoir operation scheme	$Q_{turbine}$
NAT	X	-	-	-	-
HIST-opt-Q20	O	Chapter 3.2.1	Individual dam's historical commissioned year	Optimized level	Q_{20}
HIST-opt-Q30					Q_{30}
HIST-opt-Q40					Q_{40}
HIST-low-Q20				Low level	Q_{20}
HIST-low-Q30					Q_{30}
HIST-low-Q40					Q_{40}
HIST-full				Full level	-
ALL-opt-Q20			The start year of simulation (1979)	Optimized level	Q_{20}
ALL-opt-Q30					Q_{30}
ALL-opt-Q40					Q_{40}
ALL-low-Q20				Low level	Q_{20}
ALL-low-Q30					Q_{30}
ALL-low-Q40					Q_{40}
ALL-full				Full level	-

5.3. Results and Discussion

5.3.1. River Discharge and Water Level

Figure 5-7 and **Figure 5-8** present the evaluation of simulated river discharge and water level, respectively, at the selected stations (**Table 5-2**) in the mainstem and tributaries of the Mekong river. The high fluctuations in the observations in the delta region (e.g., Can Tho) are due to the tidal effect, which is not yet considered in the current version of the model. In terms of the monthly variability of inundation extents that this study mainly focuses on, the tidal effect in a sub-monthly time scale is expected to be averaged out in a monthly time scale. The total reservoir storage capacities have been doubled in 2010 and 2016, respectively, compared to the total capacities of their preceding decades (**Figure 5-1**), hence the impacts of reservoirs are investigated for two periods, i.e., before and after 2010. Overall, the reservoir operation dampens peak flow (level) and increases low flow (level), and the impact of reservoir operation on river discharge and water level is smaller than that of inter-annual climate variability. The reservoir operation has exerted a limited influence on the variations of discharge and water level during 1979-2009, except for the Mun river basin (Pak Mun station) where many reservoirs were already built before or early in the simulation period. As more dams are built in 2010, especially the mega-sized dams built after 2014, the impacts on reservoir operation on river discharge and water level become more pronounced such that the difference between NAT and HIST simulations is noticeable in the 2014-2016 period. From these results, we conclude that climate variability has dominated the flood dynamics over the reservoir operation in the past. Nonetheless, the potential impact of existing 86 dams is found to be considerable as found in the ALL simulations where the river discharge and water level are significantly dampened by the 86 dams that are assumed to be in operation from 1979 (**Figure 5-9** and **Figure 5-10**). Since the

number of dams and their storage capacities are increasing in a rapid pace (**Figure 5-1**), the impact of reservoirs on the future MRB hydrology is expected to be accelerated.

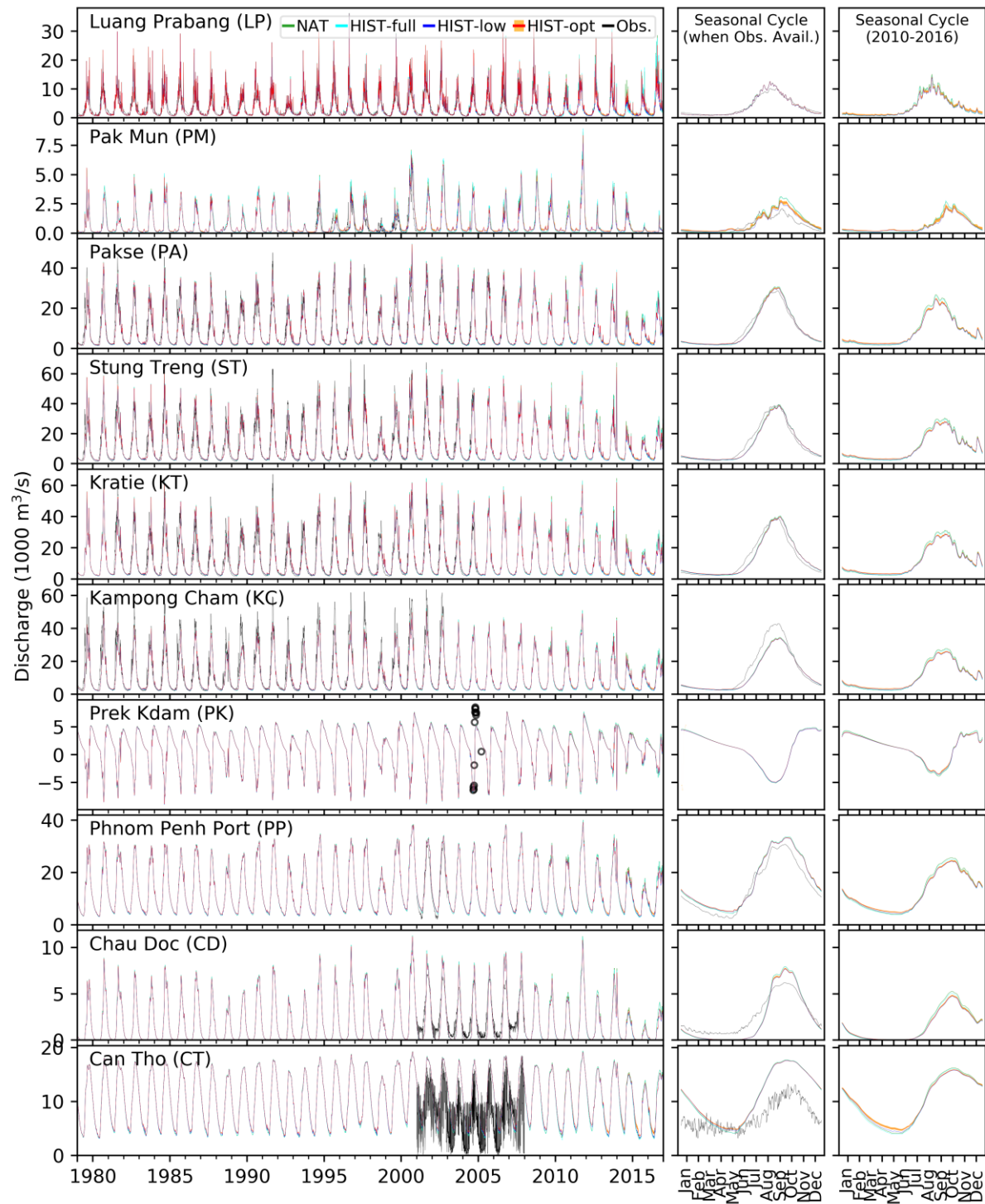


Figure 5-7 Validation of simulated river discharge. The orange shading indicates the level of uncertainty in the optimized hydropower operation. Daily time series, seasonal cycle for the time span when the observations are available, and seasonal cycle for 2010-2016 are presented in three columns from left to right, respectively. The locations of stations are shown in **Figure 5-1**.

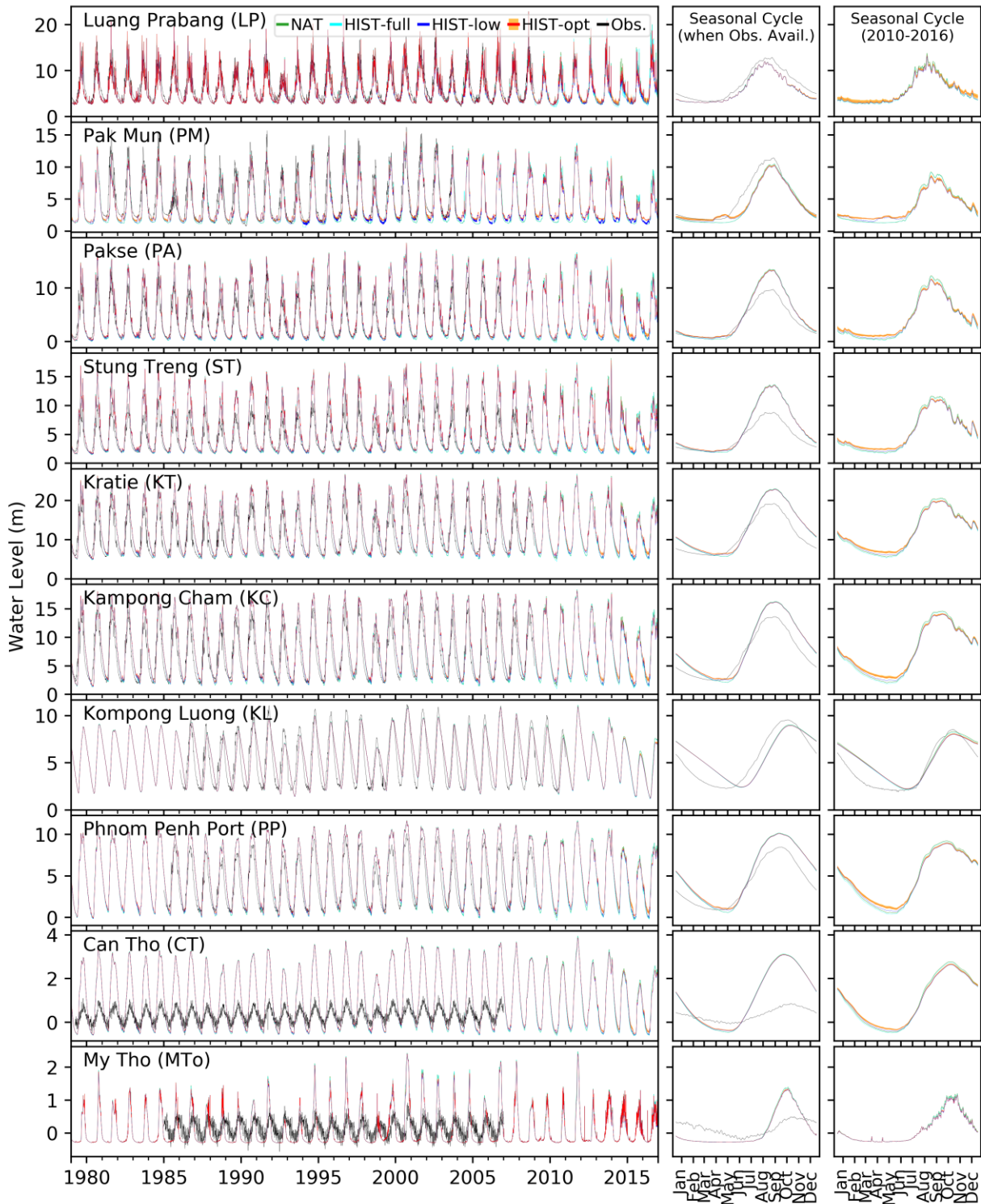


Figure 5-8 Validation of simulated water level. The orange shading indicates the level of uncertainty in the optimized hydropower operation. Daily time series, seasonal cycle for the time span when the observations are available, and seasonal cycle for 2010-2016 are presented in three columns from left to right, respectively. The locations of stations are shown in **Figure 5-1**.

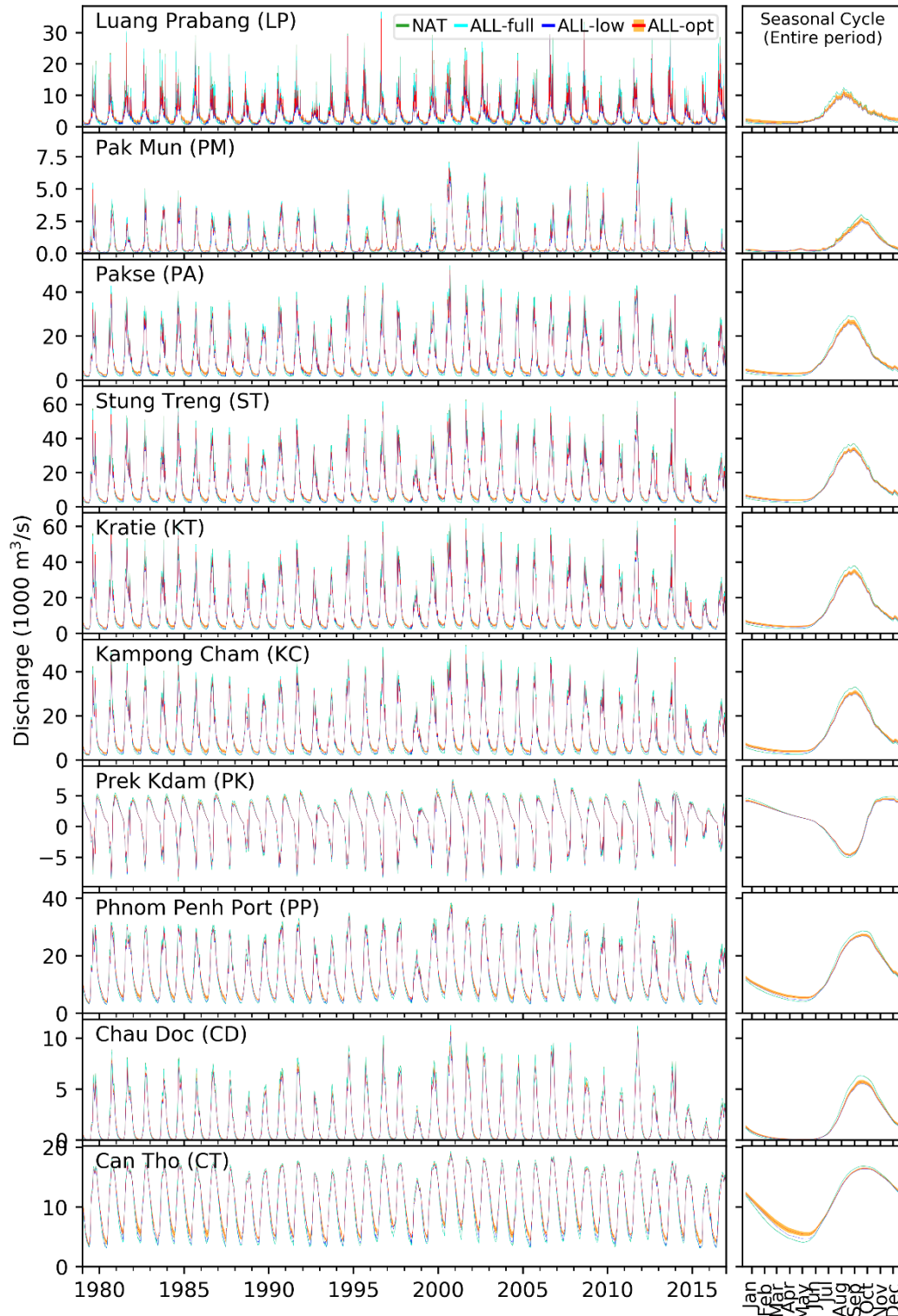


Figure 5-9 Potential changes in river discharge by the existing 86 dams estimated from the ALL simulations. In the ALL simulations, the 86 dams are modeled to be operated from the beginning (i.e., 1979) through the ending (i.e., 2016) years for the given climate conditions, which are identical to those given to the HIST (historical) simulations.

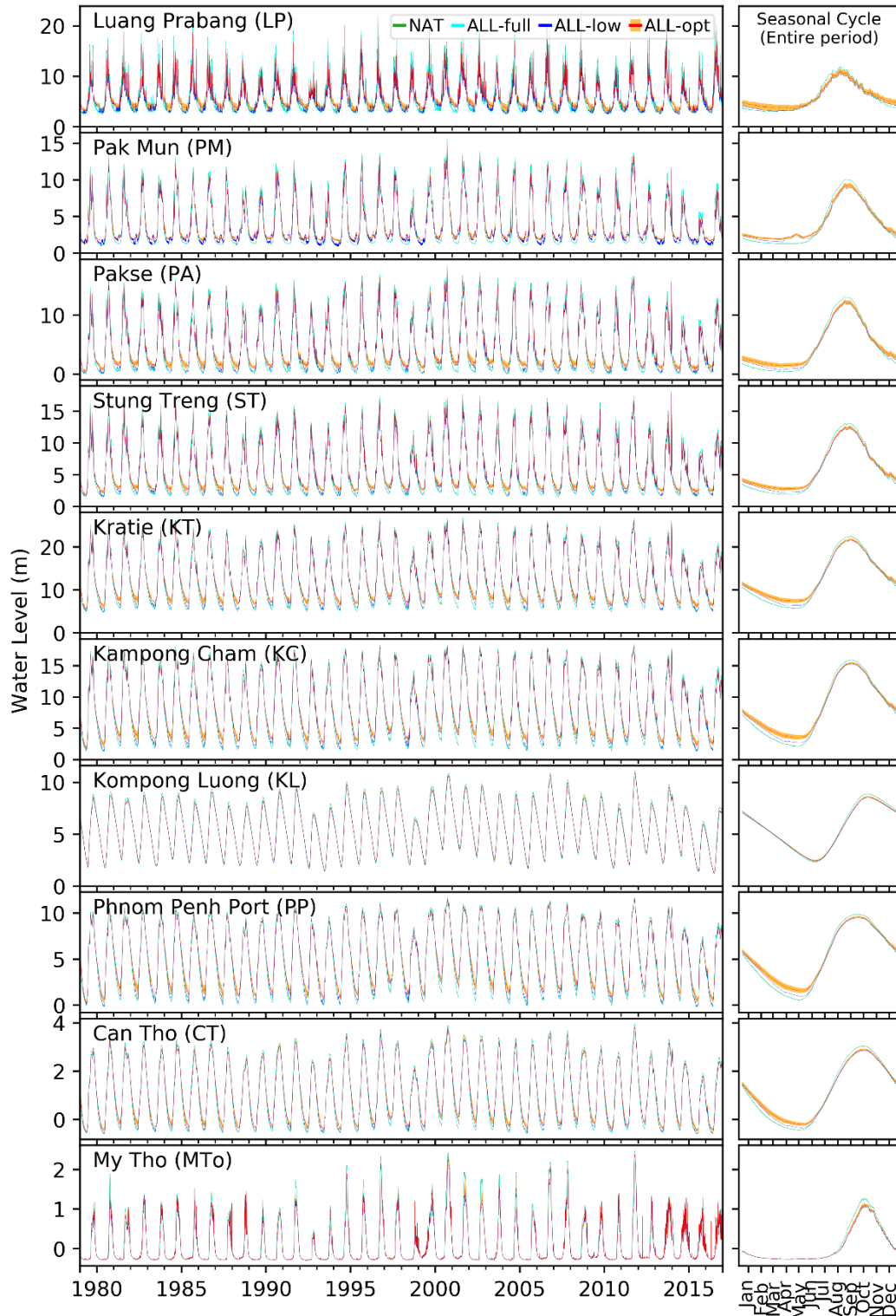


Figure 5-10 Potential changes in water level by the existing 86 dams estimated from the ALL simulations. In the ALL simulations, the 86 dams are modeled to be operated from the beginning (i.e., 1979) through the ending (i.e., 2016) years for the given climate conditions, which are identical to those given to the HIST (historical) simulations.

5.3.2. Flood Occurrence

Figure 5-11 presents the 90-m (3-arcsec) grid flood occurrence (i.e., flood frequency in percentile) for the period of 1979-2016 over the entire MRB, which is derived by downscaling the monthly-average flood depth simulated by CaMa-Flood. Flood occurrence in the major lakes, natural river channels, and reservoirs (**Figure 5-1**) is broadly reproduced by the model. Because no ground-based observations exist to evaluate the flooded extents and storages in the Mekong, we evaluate the results with remote sensing-based products from Landsat (GSW data; Pekel et al., 2016) and Sentinel-1. It is worth noting that the GSW data has a spatial resolution of 0.00025° , hence the data is upscaled data to four-times coarser resolution (i.e., 0.00100°) for a consistent comparison with CaMa-Flood results at 0.00083° resolution **Figure 5-12**. The results at the original resolution of 0.00025° are also provided in **Figure 5-13**. A reprojection of GSW data to the identical resolution of model results is avoided since it adds distortions, specifically for the number of pixels having small non-zero flood occurrence that delineates the maximum inundation extent.

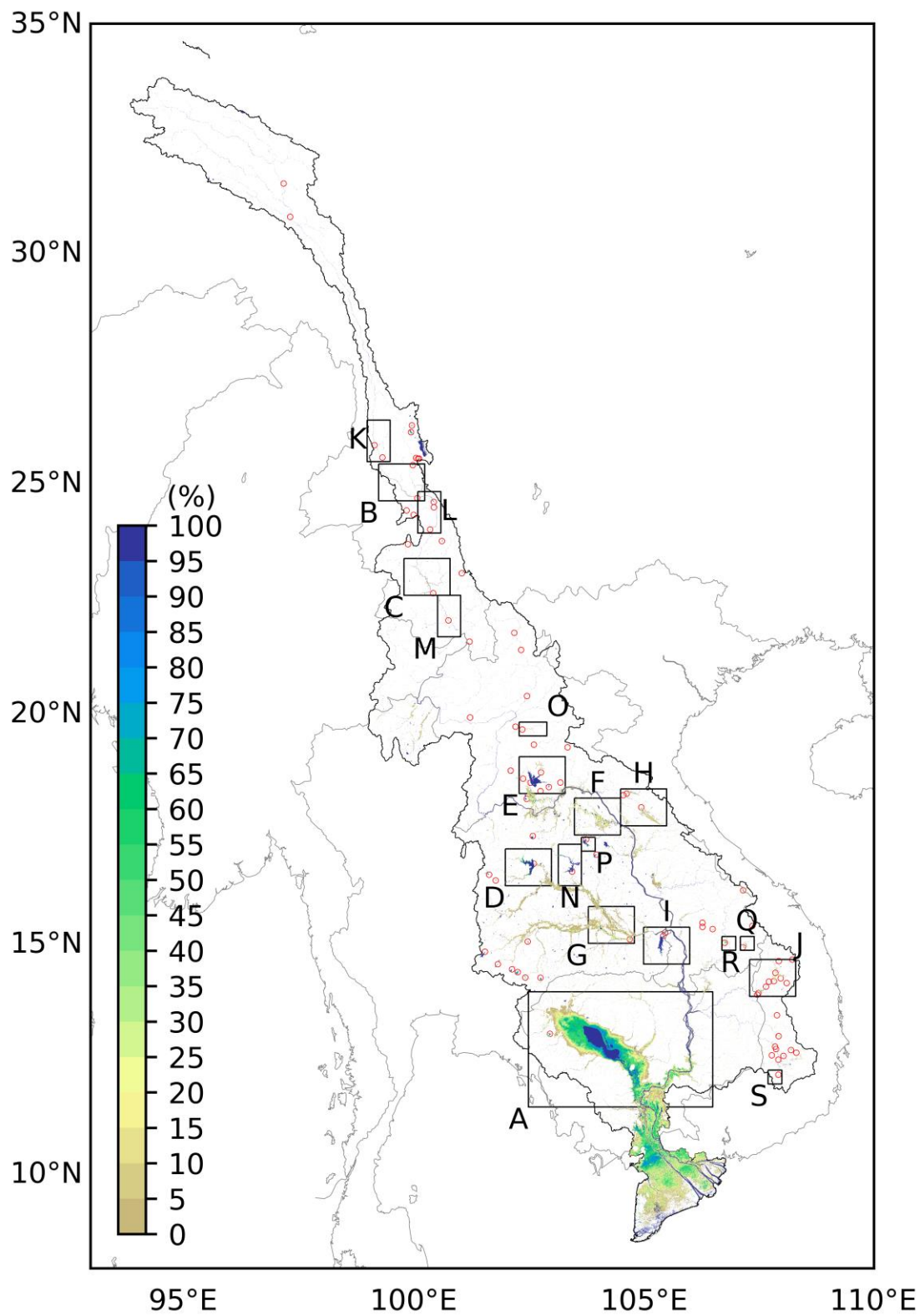


Figure 5-11 Simulated flood occurrence in 3-arcsec (90 m) over the MRB. Black boxes indicate the regions used to validate the simulated spatial inundation dynamics.

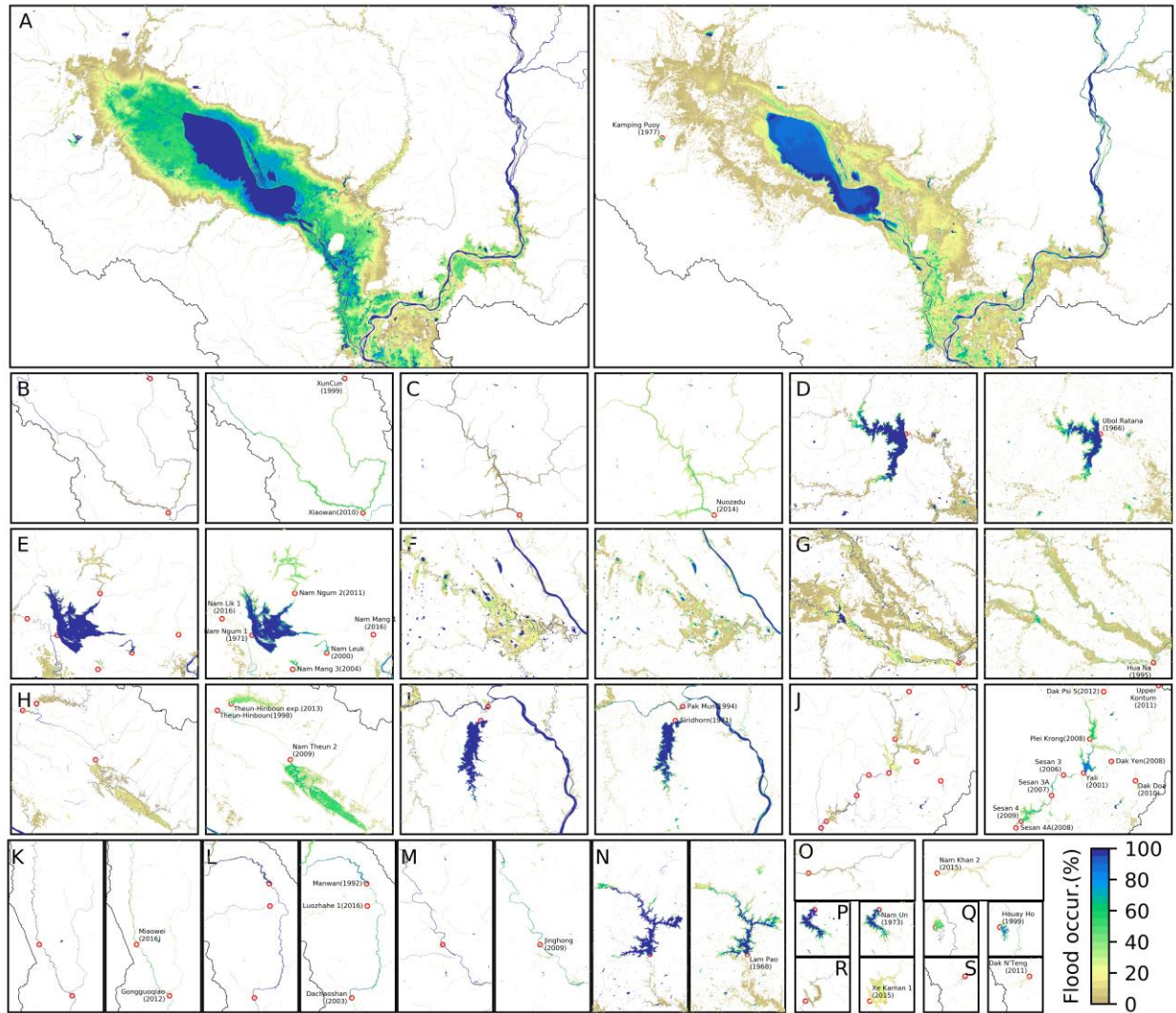


Figure 5-12 Spatial validation of simulated inundation dynamics with 0.00100° resolution GSW flood occurrence data. Simulated flood occurrence (left; CaMa-Flood) for 1979-2016 is compared with the GSW flood occurrence (right; Pekel et al. 2016) for 1984-2018. The locations of sub-panels are shown in **Figure 5-11**. The resolution of CaMa-Flood is 0.00083°.

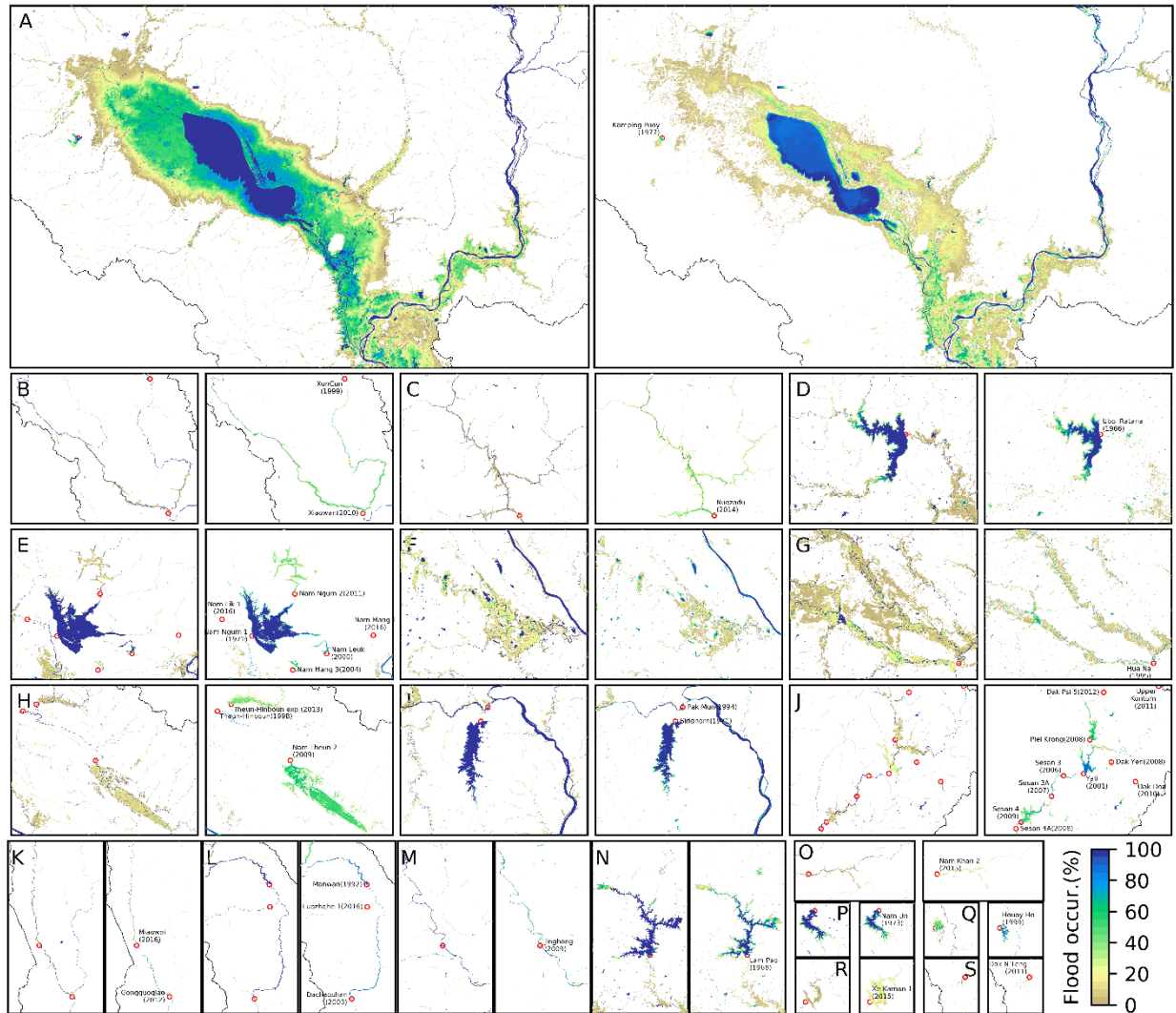


Figure 5-13 Spatial validation of simulated inundation dynamics with 0.00025° resolution GSW flood occurrence data. Simulated flood occurrence (left; CaMa-Flood) for 1979-2016 is compared with the GSW flood occurrence (right; Pekel et al. 2016) for 1984-2018. The locations of sub-panels are shown in **Figure 5-11**. The resolution of CaMa-Flood is 0.00083°.

In general, the patterns of simulated and satellite-based flood occurrences are similar for both natural river-floodplain-lake and manmade reservoir systems (**Figure 5-12** and **Figure 5-13**; hereafter only **Figure 5-12** is mentioned). First, the main body of TSL is accurately simulated to be always flooded (dark blue; 100% flood occurrence) in the CaMa-Flood, but it is sometimes wrongly represented not to be flooded (light blue; <100%) in the GSW data. Second, the

variations from the center of TSL to the maximum extents are smooth and continuous in the CaMa-Flood result while they are abrupt and sometimes intermittent (i.e., no flood areas in white) in the GSW data. Those differences are similarly found in other natural river-floodplain regions (**Figure 5-12FG**), which can be attributed to either a model overestimation or satellite product underestimation. The model can overestimate the flood occurrence due to uncertainties in meteorological (e.g., errors in the magnitude and spatio-temporal distribution of precipitation), topographic data (e.g., overrepresentation of flat areas; underrepresentation of natural and artificial riverbank), and model parameterization (e.g., under- and over-estimations of evapotranspiration and runoff). The underestimation in satellite products can be the case since Landsat imagery cannot penetrate the interfering objects over the water body, e.g., clouds, debris, and vegetations. Due to such limitation, the number of cloud-free images is limited especially in monsoon season, which can lead to the underrepresentation of flood occurrence in satellite products. Such limitation can be complemented by using the advanced remote sensing data. For example, Sentinel-1 in short-wavelength (5.5 cm) can penetrate clouds so that the flood extent in flooding season can be better represented, but the penetration of Sentinel-1 is still limited, specifically for very dense vegetation canopy at high biomass (**Figure 5-14**). For the vegetation dense regions, L-band remote sensing products can be useful (Urbazaev et al., 2018). The stripes-like noises in Sentinel-1 product are due to the processing issues from IPF of ESA, which should be removed for further quantitative analysis.

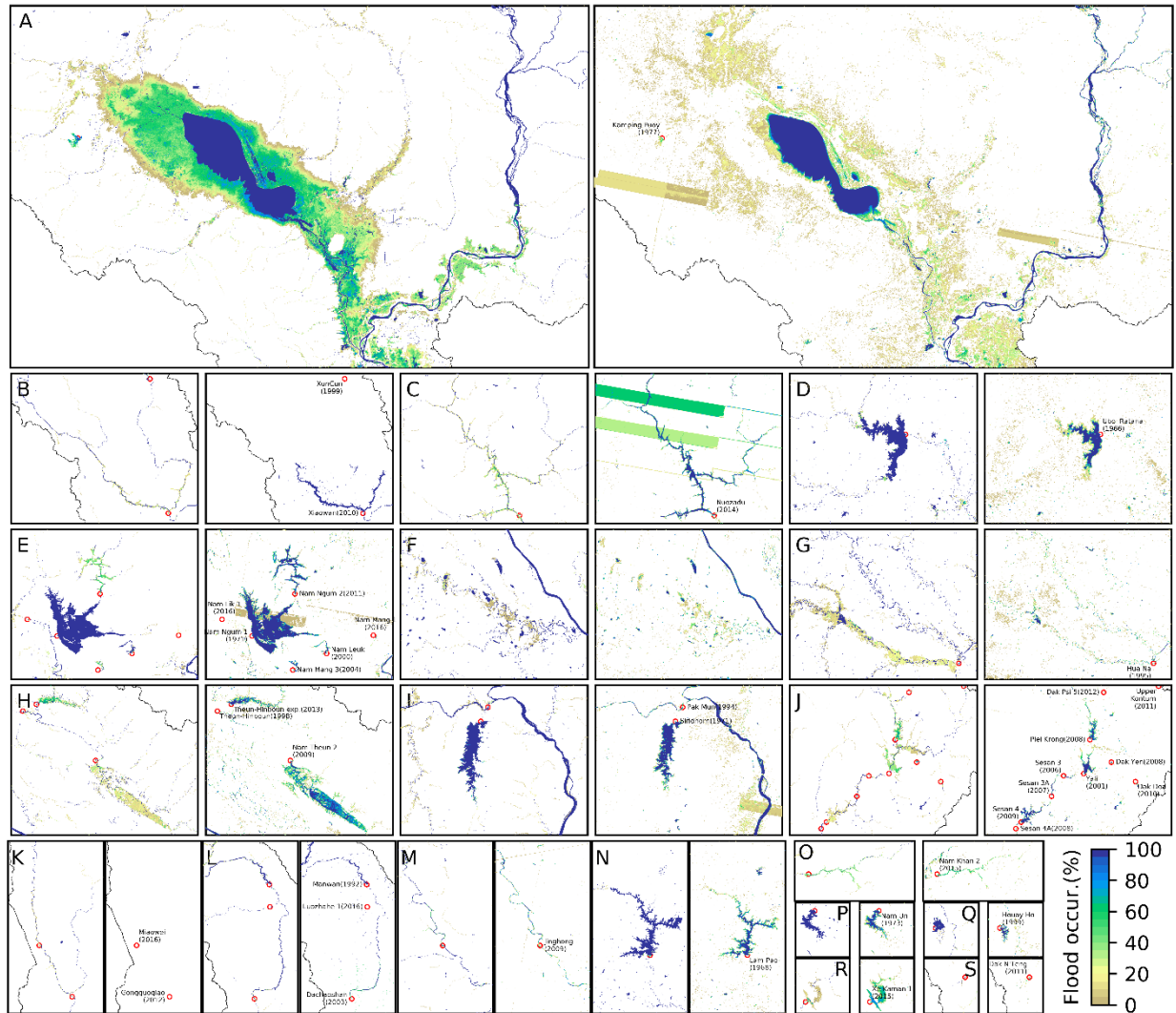


Figure 5-14 Spatial validation of simulated inundation dynamics with the Sentinel-1 product. Simulated flood occurrence (left; CaMa-Flood) for 2014-2016 is compared with the Sentinel-1 occurrence (right) for 2014-2016. The locations of sub-panels are shown in **Figure 5-11**. The resolutions of CaMa-Flood and GSW data are identical to 0.00083° .

For the reservoir inundation (**Figure 5-12B-E;H-S**), the similarity in the inundation extent and patterns between the simulation and remote sensing product demonstrates that the issues of high uncertainties in the dam and reservoir dataset (Chapter 5.2.2) are reasonably curated; if not, e.g., the erroneous dam specifications are employed, the simulated inundation extents can be too smaller or larger than the satellite-based inundation extents. The core-part of

reservoirs built before 1979 and 1984 for CaMa-Flood and GSW data, respectively, have large permanent water bodies ($\approx 100\%$). In CaMa-Flood results, those reservoirs show smaller seasonal variation of inundation near the reservoir boundaries. It is attributed to the flat areas within reservoirs in the SRTM data, which is the main source of MERIT DEM that we employed. When the SRTM was launched on February 2000, if the reservoirs already impounded water in their upstream, the water surface elevation that is flat over the reservoir are measured. The water body portion is not yet removed while many other errors and noises are removed (D. Yamazaki et al., 2017, 2019). The grid cells within the flat area are simulated to be inundated all at once, hence the CaMa-Flood simulates the permanent reservoir water body portions of the reservoirs built before 2000 to be larger and less seasonally varying compared to the GSW data represents. On the contrary, the bathymetries of reservoirs built after 2000 can be parameterized to have more spatially varying elevations, hence flood occurrences change within reservoir extents. There are some reservoirs whose new permanent water area (i.e., yellow-to-green color) is shown in a different color in different products and results of CaMa-Flood, GSW data, and Sentinel-1 data (e.g., Xiaowan, Nuozadu, and Nam Ngum 2 in **Figure 5-12B, C, E**, respectively). It could be because the time period of the remote sensing product is different from the period of the model (GSW data), the limited images availability due to the atmosphere condition (GSW data), or the time period is set to too early from the launching date to regularly and stably acquire the remote sensing products (Sentinel-1).

While the inundation pattern starts from the location of a dam, the dam location can be located at any positions within a modeling grid. Hence, the downscaled flood extent can contain the errors in the inundation pattern starting point in the degree of less than 5-km scale. For example, the inundations near the dam locations initiate slightly at downstream of dams (e.g.,

Nuozadu, Miaowei, and Nam Khan 2 in Figure 5C, K, and O, respectively) or at upstream of dams (e.g., Theun-Hinboun exp., Yali, and Manwan in Figure 5H, J, and L, respectively). Such issues cannot be completely eliminated, but they can be alleviated by increasing the spatial resolution. Additionally, to better simulate spatial variation of inundation extent of the reservoirs built before the SRTM lunch, the more realistic reservoir bathymetry can be produced by utilizing other credible data or local data (van Bemmelen et al., 2016; Busker et al., 2018; Li et al., 2019).

Overall, the maximum inundation extents are found to be reasonably well simulated, and the recent reservoirs show more spatially varying flood depth within the reservoirs. As such, the modeling approach used in this study is promising in terms of modeling future dams as well as existing dams.

5.3.3. Flooded Area and Surface Water Storage

Figure 5-15 shows the historical surface water storage and extent dynamics over the MRB simulated by CaMa-Flood in terms of the changes in seasonal variation for entire period for 1979-2016 (**Figure 5-15a**) and at decadal intervals (**Figure 5-15b-e**) and intra-annual variability of the selected years (1998 and 2015 for dry years; 2000 for wet years; **Figure 5-15f-h**), along with the comparison of GSW monthly flooded area. The daily time series for the entire period of 1979-2016 are presented in **Figure 5-16**. Overall, the flooded area accounts for 3-8% (24,000-64,000 km²) and less than 1% (<800km²) of the MRB area in wet and dry seasons, respectively, according to CaMa-Flood results. Evidently, large deviations are found between the flooded area of CaMa-Flood and GSW data, specifically in the years before 2000 and flooding seasons (**Figure 5-15** and **Figure 5-16**). The deviations are partly attributed to the model

overestimation as discussed in Chapter 5.3.2; however, considering many of Landsat image pixels in the MRB regions are classified as “No Data” in the GSW monthly data and those “No Data” area becomes easily more than half of the entire MRB area specifically in the years before 2000 and flooding seasons (**Figure 5-17**), the large deviations are likely attributed to the underestimation of GSW data. This assertion is partly supported by the decreased deviations in the months that have small number of “No Data” pixels (**Figure 5-16; Figure 5-17**).

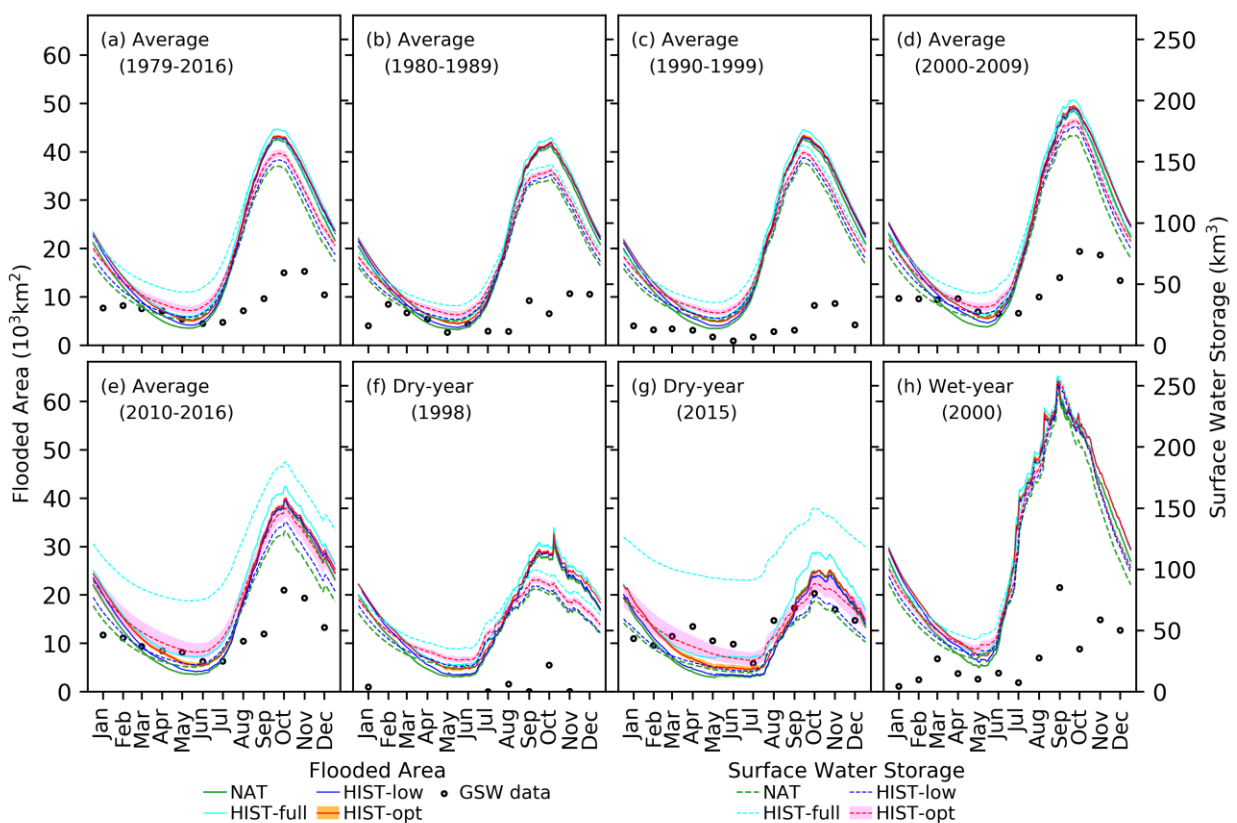


Figure 5-15 Historical flooded area and surface water storage dynamics over the MRB. The seasonal average and daily time series are presented for (a-e) the selected periods and (f-h) dry- and wet-years, respectively. The orange and pink shadings indicate the level of uncertainty in the optimized hydropower operation for the flooded area and surface water storage, respectively. The monthly GSW flooded area for 1984-2016 is presented for the periods and years wherever available.

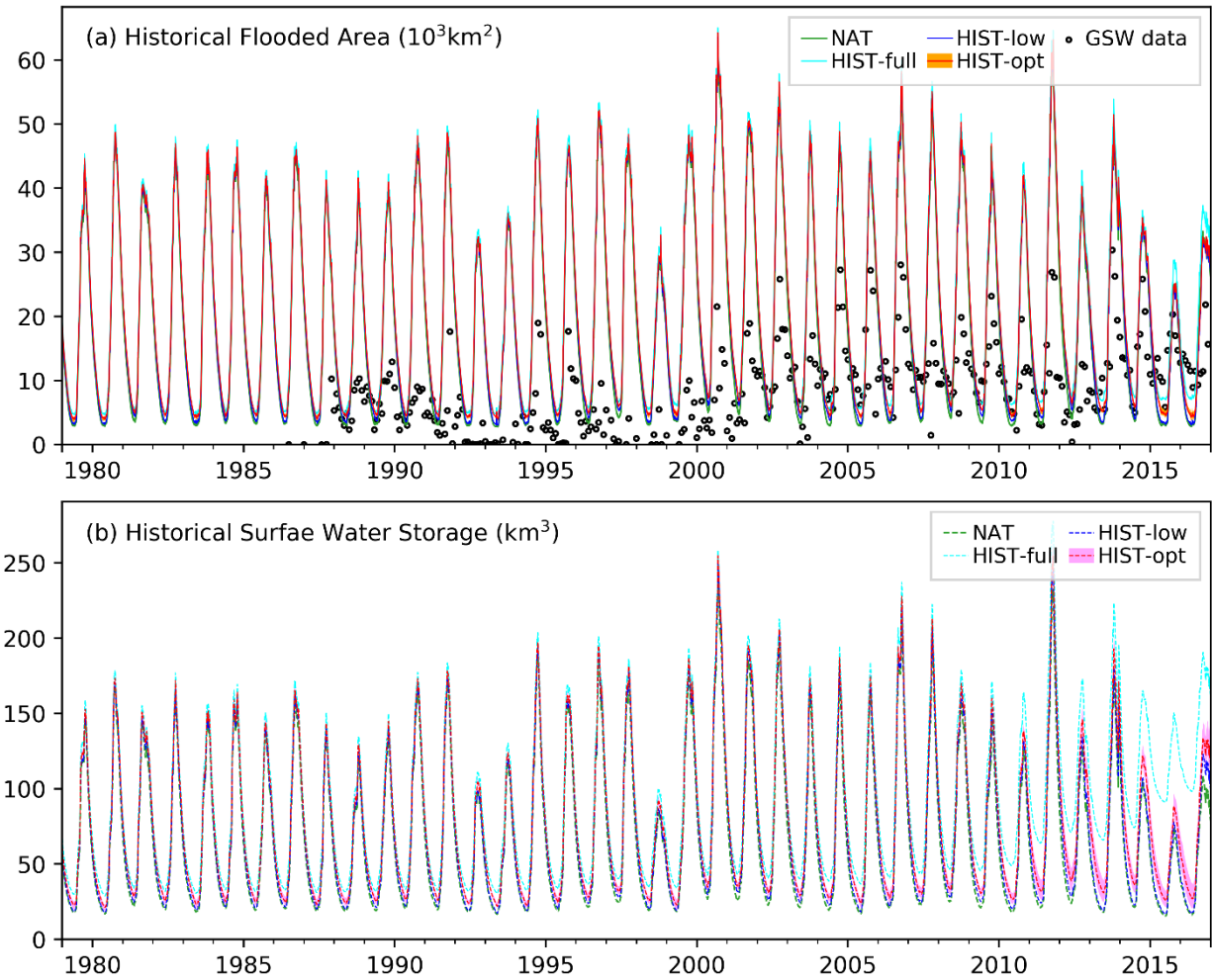


Figure 5-16 Historical flooded area and surface water storage dynamics over the MRB for 1979-2016. The orange and pink shadings indicate the level of uncertainty in the optimized hydropower operation for the flooded area and surface water storage, respectively. The monthly GSW flooded area for 1984-2016 is presented for the periods and years wherever available.

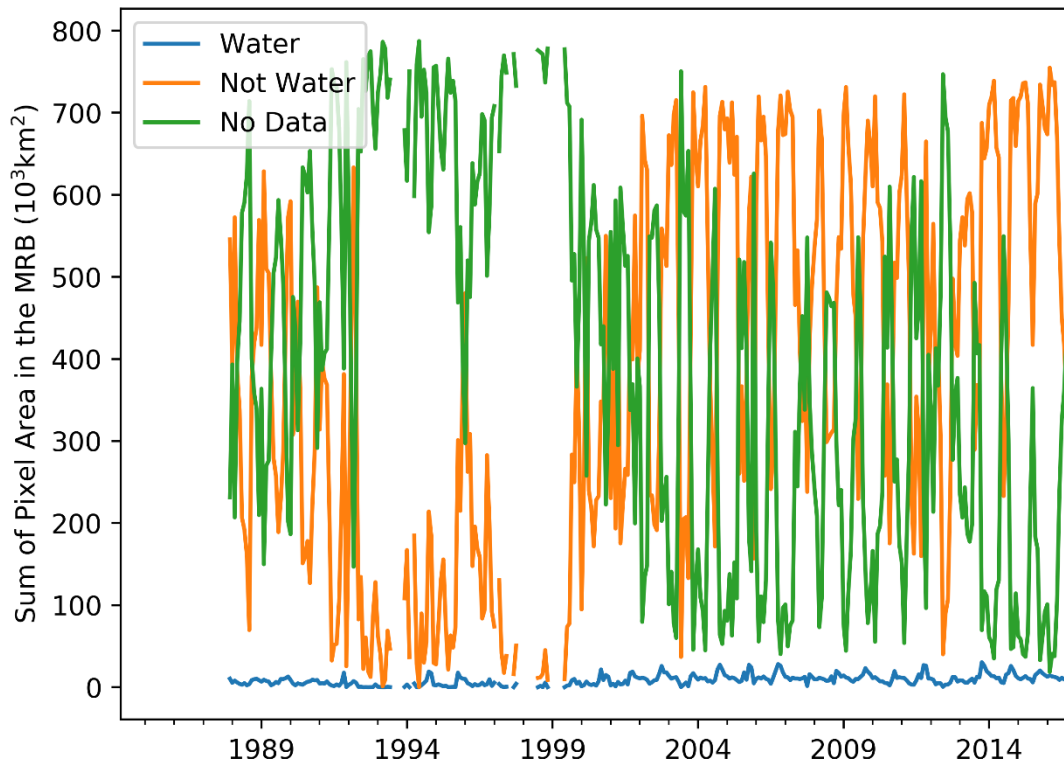


Figure 5-17 The monthly GSW flooded area for 1984-2016. Pixels are classified to either “Water” (blue), “Not Water” (orange), or “No Data” (green). For visualization purpose, the records of a month are masked out (i.e., no lines or broken lines) when the entire pixels in the MRB for the month have the “No Data” value.

While the inter-annual variability is evident in the surface water storage and extent dynamics, no significant inter-annual trend is found in the NAT simulation for the minimum, maximum, mean, standard deviation, and the maximum amplitude of flooded area (Mann-Kendall test, $p > 0.31$ for all variables, $\alpha = 0.05$; hereafter only the minimum p-value is provided) and surface water storage ($p > 0.42$), respectively. For the HIST simulations, except for HIST-low-Q20 that is designed to provide the lowest bound in flooded area and storage water change by dams (Chapter 5.2.6), all HIST simulations show increasing trends in the minimum value of

flooded area and minimum surface water storage, respectively ($p < 0.01$). Meanwhile, none of HIST simulations shows significant trends in standard deviations and the maximum amplitudes ($p > 0.39$). Results suggest that the reservoirs are likely to have exerted influence on the surface water storage and extent dynamics over the MRB in dry season while the inter-annual climate variability has dominated the inter-annual variability of surface water storage and extent dynamics, specifically for wet season.

As the number and storage capacities of reservoirs increase, the response of surface water storage and extent dynamics can be considerably different from the past even if the identical climate condition is given. In HIST simulations, two dry-year of 1998 and 2015 are similarly dry, but the variation of change by reservoirs is evidently greater in 2015 than that in 1998. The continuing impacts of existing 86 dams (as of 2016) on the future MRB hydrology can be found in ALL simulations, where the all existing dams are simulated to be operated since 1979 (Chapter 5.2.6). Compared to HIST simulations, ALL simulations show higher variability in the surface water storage and extent dynamics over the entire simulation period (**Figure 5-18; Figure 5-19**). It is noted that the ALL simulations show no significant trends in both flooded area and surface storage for any of the attributes of the minimum, maximum, mean, standard deviation, and the maximum amplitude ($p > 0.4$) since the meteorological forcing of HIST simulation is also used for ALL simulation. The result should be interpreted with caution since different results can be obtained when other climate projections having wetter or drier trend are used.

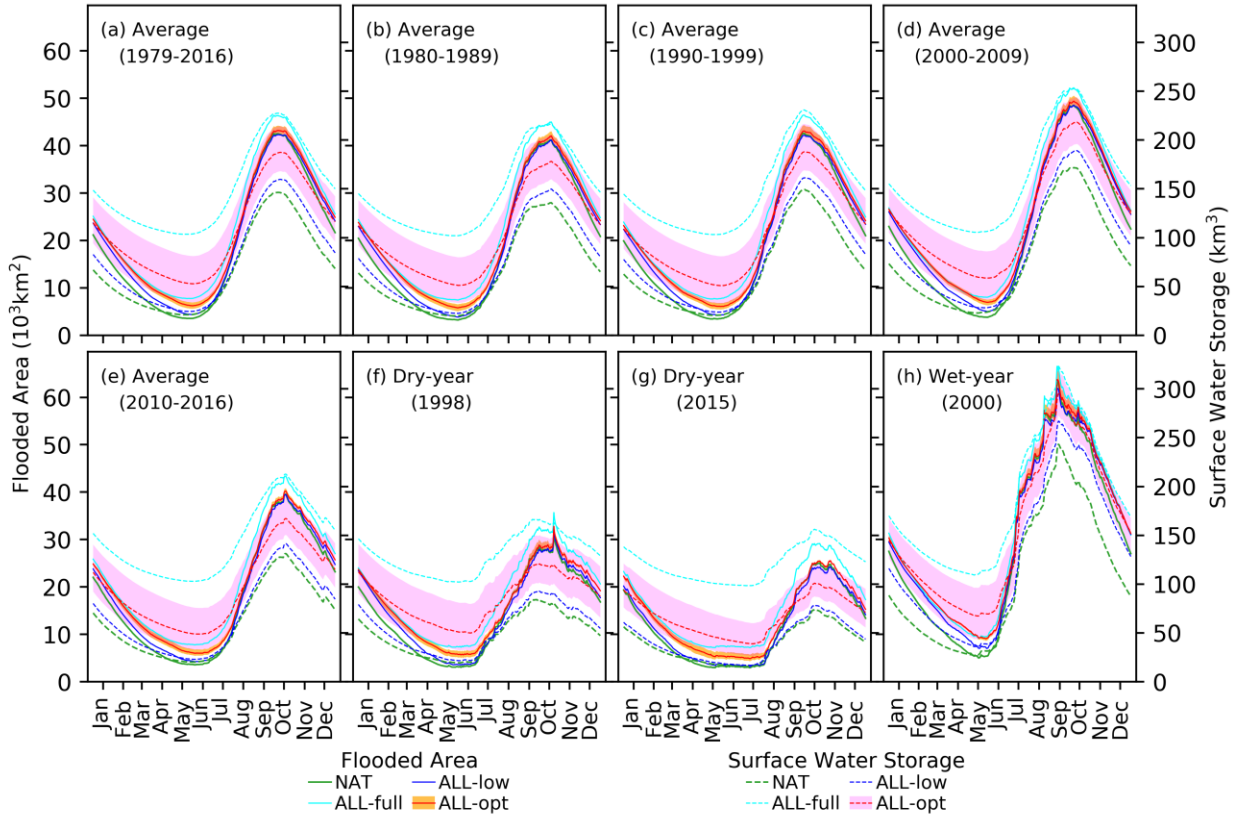


Figure 5-18 The potential impacts of existing 86 dams on surface water dynamics estimated from the ALL simulations for selected periods and years. In the ALL simulations, the 86 dams are modeled to be operated from the beginning (i.e., 1979) through the ending (i.e., 2016) years for the given climate conditions, which are identical to those given to the HIST (historical) simulations.

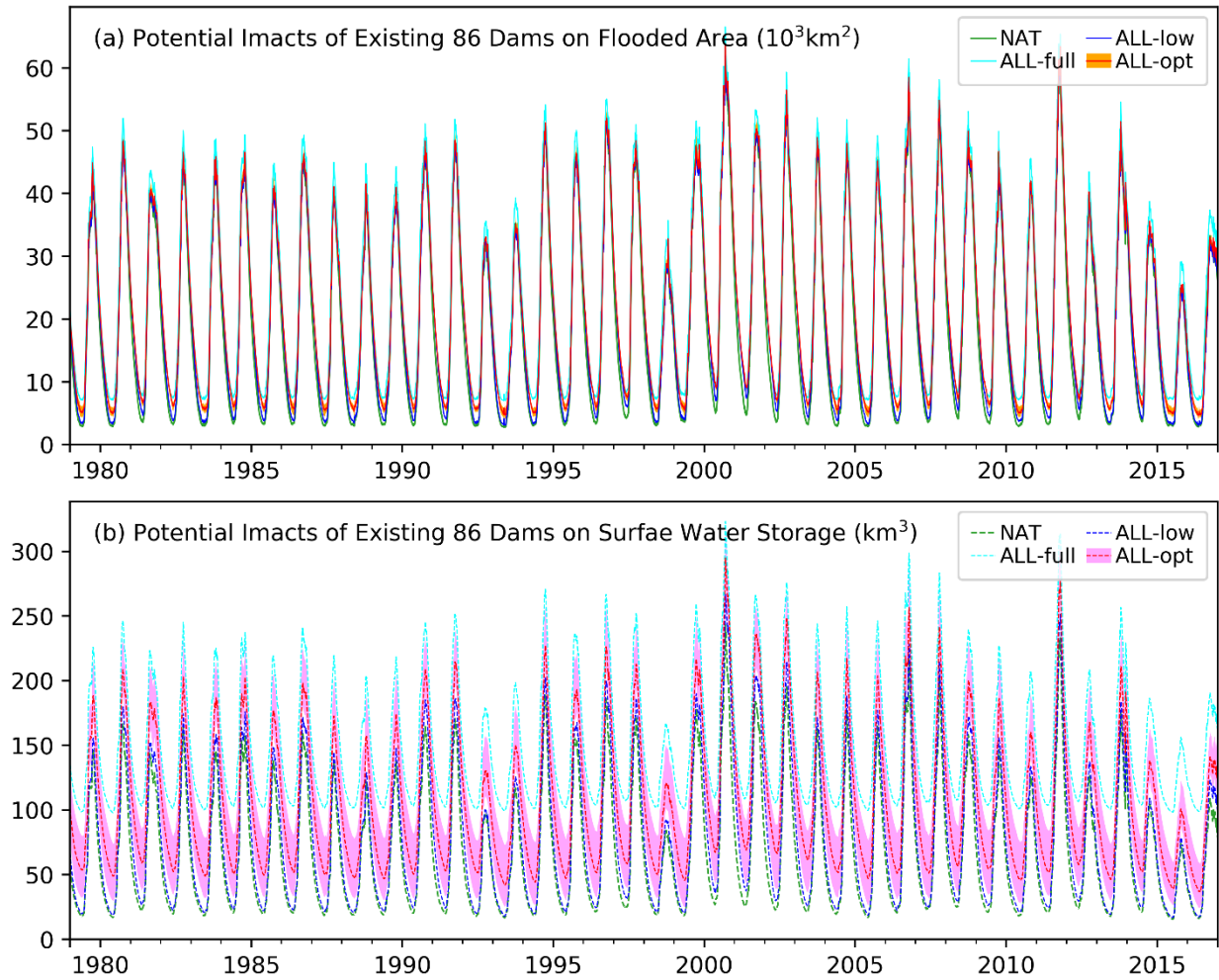


Figure 5-19 The potential impacts of existing 86 dams on surface water dynamics estimated from the ALL simulations for the entire simulation period. In the ALL simulations, the 86 dams are modeled to be operated from the beginning (i.e., 1979) through the ending (i.e., 2016) years for the given climate conditions, which are identical to those given to the HIST (historical) simulations.

5.4. Results and Discussion

In this chapter, the historical dynamics of surface water storage and extent dynamics over the entire MRB are simulated for the period of 1979-2016 (HIST simulations). Through the modeling of the natural river-floodplain-lake system and manmade reservoirs in an integral manner, the natural and human-induced changes in flood dynamics over the entire basin are investigated altogether. To do so, the newly developed reservoir scheme (Chapters 2 and 3) is incorporated into a global river-floodplain hydrodynamics model (CaMa-Flood; Yamazaki et al. 2013). For reservoir operation schemes, the demand-driven operation scheme (Chapter 3.2.1) and optimized operation scheme are used for irrigation and hydropower reservoirs, respectively. By using wide range of turbine designed flow Q_{turbine} (Q_{20} , Q_{30} , and Q_{40}) and various operation modes (opt, low, and full), the uncertainties in reservoir operations are considered. The results are validated with the ground-based observations for discharge and water level and with the remote sensing products (Landsat and Sentinel-1 derived products) for spatial inundation dynamics. Along with the historical (HIST) simulations, the probable future impact of the existing 86 dams (as of 2016) is estimated from ALL simulations, where the same meteorological data and reservoir operation schemes are used yet the all existing dams are assumed to be operated from the beginning of the modeling period (i.e., 1979). Results suggest that the inter-annual flood dynamics of surface water storage in the MRB have been mainly controlled by climate variability over the past four decades. Compared to the climate variability, the reservoir impacts are small in the past, specifically before 2010; however, the surface water dynamics is found to be already significantly altered by the reservoirs, and results also suggest that the surface water storage dynamics in the future would be likely different from that in the past even without additional dam constructions. As a greater number of mega-sized are

proposed, planned, and under construction, the impacts of reservoirs on the MRB hydrology is expected to be accelerated. As the change of surface water storage and extent dynamics is simulated to highly depend on the reservoir operation policy, the “Good design” (Sabo et al., 2017) of hydropower reservoir operation rule would be desirable for the sustainable hydro-ecological system of the MRB.

Chapter 6. Summary and Conclusion

Manmade reservoirs are important components of the terrestrial water cycle. Considering the importance of manmade reservoirs in mediating processes in both local and global scales, improving reservoir modeling is an indispensable effort in hydrologic and climate modeling; however, reservoirs have been poorly modeled by treating them as separated entities from natural river-floodplain system not only in coarse-resolution models but also in recently developed high-resolution models.

In Chapters 2 and 3, the new high-resolution continental-scale reservoir storage dynamics and release scheme is presented by enhancing existing schemes and adding critical novel parameterizations to improve reservoir storage and release simulations. The new scheme simulates river-floodplain-reservoir storages in an integrated manner considering their spatial and temporal variations. A new calibration scheme is also incorporated to better simulate reservoir dynamics considering cascade-reservoir effects. Further, since no reservoir bathymetry data are available over large domains, a state-of-the-art digital elevation model and reservoir extent data are used to derive reservoir bed elevation. The new scheme can be used as a standard-alone surface water model (e.g., CaMa-Flood) that digests runoff outputs from Land Surface Models (e.g., HiGW-MAT) or can be integrated within the river-floodplain routing scheme of hydrological models (e.g., LEAF-Hydro-Flood and Community Land Model). The new modeling framework for integrated simulation of river, reservoirs, and floodplain is first tested for the Contiguous US having abundant data. Comparison of results with satellite-based surface water data shows that the model accurately reproduces the large-scale patterns of reservoir-floodplain inundation extents, and the results of reservoir release and storage are also found to be improved.

In Chapters 4, the potential disruption of flood dynamics in the Tonle Sap River (TSR) and Mekong Delta by upstream flow regulation is investigated in the form of sensitivity analysis. It is found that the effects of flow regulation on downstream river-floodplain dynamics are relatively predictable along the mainstem of Mekong river, but flow regulations could potentially disrupt the flood dynamics in the TSR and small distributaries in the Mekong Delta. Modeling results suggest that TSR flow reversal could cease if the Mekong flood pulse is dampened by 50% and delayed by one-month. As the upstream regulation is intensified, flood occurrence near Tonle Sap Lake and Mekong river reaches is increased while other regions are less flooded.

In Chapter 5, the historical dynamics of surface water storage and extent dynamics over the entire MRB are simulated for the period of 1979-2016. The optimized reservoir operation scheme is newly incorporated to the modeling framework with the consideration of uncertainties in reservoir operations. Results suggest that the inter-annual flood dynamics of surface water storage in the MRB have been mainly controlled by climate variability over the past four decades. Compared to the climate variability, the reservoir impacts are small in the past, specifically before 2010; however, the surface water dynamics is found to be already significantly altered by the reservoirs, and results also suggest that the surface water storage dynamics in the future would be likely different from that in the past even without additional dam constructions.

It is expected that the new modeling framework presented in this study will inform the incorporation of reservoirs in hyper-resolution models to improve simulations of terrestrial water storage and flow and examine reservoir-atmosphere interactions over large domains.

REFERENCES

REFERENCES

- Adam, J. C., Haddeland, I., Su, F., & Lettenmaier, D. P. (2007). Simulation of reservoir influences on annual and seasonal streamflow changes for the Lena, Yenisei, and Ob' rivers. *Journal of Geophysical Research Atmospheres*, 112(24), 1–22. <https://doi.org/10.1029/2007JD008525>
- Aggarwal, S. K., Saini, L. M., & Kumar, A. (2009). Electricity price forecasting in deregulated markets: A review and evaluation. *International Journal of Electrical Power & Energy Systems*, 31(1), 13–22. <https://doi.org/10.1016/j.ijepes.2008.09.003>
- Akter, A., & Babel, M. S. (2012). Hydrological modeling of the Mun River basin in Thailand. *Journal of Hydrology*, 452–453, 232–246. <https://doi.org/10.1016/j.jhydrol.2012.05.059>
- Allison, M. A., Demas, C. R., Ebersole, B. A., Kleiss, B. A., Little, C. D., Meselhe, E. A., et al. (2012). A water and sediment budget for the lower Mississippi-Atchafalaya River in flood years 2008-2010: Implications for sediment discharge to the oceans and coastal restoration in Louisiana. *Journal of Hydrology*, 432–433, 84–97. <https://doi.org/10.1016/j.jhydrol.2012.02.020>
- Arias, M. E., Cochrane, T. A., Piman, T., Kumm, M., Caruso, B. S., & Killeen, T. J. (2012). Quantifying changes in flooding and habitats in the Tonle Sap Lake (Cambodia) caused by water infrastructure development and climate change in the Mekong Basin. *Journal of Environmental Management*, 112, 53–66. <https://doi.org/10.1016/j.jenvman.2012.07.003>
- Arias, M. E., Cochrane, T. A., Norton, D., Killeen, T. J., & Khon, P. (2013). The Flood Pulse as the Underlying Driver of Vegetation in the Largest Wetland and Fishery of the Mekong Basin. *AMBIO*, 42(7), 864–876. <https://doi.org/10.1007/s13280-013-0424-4>
- Arias, M. E., Piman, T., Lauri, H., Cochrane, T. A., & Kumm, M. (2014). Dams on Mekong tributaries as significant contributors of hydrological alterations to the Tonle Sap Floodplain in Cambodia. *Hydrology and Earth System Sciences*, 18(12), 5303–5315. <https://doi.org/10.5194/hess-18-5303-2014>
- Arias, M. E., Cochrane, T. A., Kumm, M., Lauri, H., Holtgrieve, G. W., Koponen, J., & Piman, T. (2014). Impacts of hydropower and climate change on drivers of ecological productivity of Southeast Asia's most important wetland. *Ecological Modelling*, 272, 252–263. <https://doi.org/10.1016/j.ecolmodel.2013.10.015>
- Babbitt, B. (2002). What Goes Up, May Come Down Learning from our experiences with dam construction in the past can guide and improve dam removal in the future. *BioScience*, 52(8), 656–658. <https://doi.org/10.1641/0006-3568>
- Baran, E., & Myschowoda, C. (2009). Dams and fisheries in the Mekong Basin. *Aquatic Ecosystem Health & Management*, 12(3), 227–234. <https://doi.org/10.1080/14634980903149902>

- Bates, P. D., Horritt, M. S., & Fewtrell, T. J. (2010). A simple inertial formulation of the shallow water equations for efficient two-dimensional flood inundation modelling. *Journal of Hydrology*, 387(1–2), 33–45. <https://doi.org/10.1016/j.jhydrol.2010.03.027>
- van Beek, L. P. H., Wada, Y., & Bierkens, M. F. P. (2011). Global monthly water stress: 1. Water balance and water availability. *Water Resources Research*, 47(7), 1–25. <https://doi.org/10.1029/2010WR009791>
- Bellman, R. (1961). *Adaptive control processes: a guided tour*. Princeton University Press.
- van Bemmelen, C. W. T., Mann, M., de Ridder, M. P., Rutten, M. M., & van de Giesen, N. C. (2016). Determining water reservoir characteristics with global elevation data. *Geophysical Research Letters*, 43(21), 11,278–11,286. <https://doi.org/10.1002/2016GL069816>
- Benedict, I., Van Heerwaarden, C. C., Weerts, A. H., Hazeleger, W., & Benedict, I. (2017). An evaluation of the importance of spatial resolution in a global climate and hydrological model based on the Rhine and Mississippi basin. *Hydrol. Earth Syst. Sci. Discuss.*, 2017(September), 1–28. <https://doi.org/10.5194/hess-2017-473>
- Beven, K., Cloke, H., Pappenberger, F., Lamb, R., & Hunter, N. (2015). Hyperresolution information and hyperresolution ignorance in modelling the hydrology of the land surface. *Science China Earth Sciences*, 58(1). <https://doi.org/10.1007/s11430-014-5003-4>
- Biemans, H., Haddeland, I., Kabat, P., Ludwig, F., Hutjes, R. W. A., Heinke, J., et al. (2011). Impact of reservoirs on river discharge and irrigation water supply during the 20th century. *Water Resources Research*, 47(3). <https://doi.org/10.1029/2009WR008929>
- Bierkens, M. F. P. (2015). Global hydrology 2015: State, trends, and directions. *Water Resources Research*, 51(7). <https://doi.org/10.1002/2015WR017173>
- Bierkens, M. F. P., Bell, V. A., Burek, P., Chaney, N., Condon, L. E., David, C. H., et al. (2015). Hyper-resolution global hydrological modelling: What is next?: “Everywhere and locally relevant.” *Hydrological Processes*, 29(2), 310–320. <https://doi.org/10.1002/hyp.10391>
- Binnie, G. M. (1987). Masonry and Concrete Dams 1880–1941. *Industrial Archaeology Review*, 10(1), 41–58. <https://doi.org/10.1179/iar.1987.10.1.41>
- Bohannon, J. (2010). The Nile delta’s sinking future. *Science*, 327(5972), 1444–1447. <https://doi.org/10.1126/science.327.5972.1444>
- Bonheur, N., & Lane, B. D. (2002). Natural resources management for human security in Cambodia’s Tonle Sap Biosphere Reserve. *Environmental Science and Policy*, 5(1), 33–41.
- Bonnema, M., & Hossain, F. (2017). Inferring reservoir operating patterns across the Mekong Basin using only space observations. *Water Resources Research*, 53(5), 3791–3810. <https://doi.org/10.1002/2016WR019978>

- Brownell, R. L., Reeves, R. R., Thomas, P. O., Smith, B. D., & Ryan, G. E. (2017). Dams threaten rare Mekong dolphins. *Science*, 355(6327), 805.1–805. <https://doi.org/10.1126/science.aam6406>
- Buccola, N. L., Turner, D. F., & Rounds, S. A. (2016). *Water temperature effects from simulated dam operations and structures in the Middle Fork Willamette River, western Oregon* (p. 49). Reston, VA. <https://doi.org/10.3133/ofr20161159>
- Bunn, S. E., & Arthington, A. H. (2002). Basic principles and ecological consequences of altered flow regimes for aquatic biodiversity. *Environmental Management*, 30(4), 492–507. <https://doi.org/10.1007/s00267-002-2737-0>
- Busker, T., de Roo, A., Gelati, E., Schwatke, C., Adamovic, M., Bisselink, B., et al. (2018). A global lake and reservoir volume analysis using a surface water dataset and satellite altimetry. *Hydrology and Earth System Sciences Discussions*, 1–32. <https://doi.org/10.5194/hess-2018-21>
- Chao, B. F., Wu, Y. H., & Li, Y. S. (2008). Impact of artificial reservoir water impoundment on global sea level. *Science*, 320(5873), 212 LP – 214. Retrieved from <http://science.sciencemag.org/content/320/5873/212.abstract>
- Chaudhari, S., Felfelani, F., Shin, S., & Pokhrel, Y. (2018). Climate and anthropogenic contributions to the desiccation of the second largest saline lake in the twentieth century. *Journal of Hydrology*, 560, 342–353. <https://doi.org/10.1016/j.jhydrol.2018.03.034>
- Clark, M. P., Bierkens, M. F. P., Samaniego, L., Woods, R. A., Uijlenhoet, R., Bennett, K. E., et al. (2017). The evolution of process-based hydrologic models: Historical challenges and the collective quest for physical realism. *Hydrology and Earth System Sciences*, 21(7), 3427–3440. <https://doi.org/10.5194/hess-21-3427-2017>
- Cleveland, W. S. (1979). Robust Locally Weighted Regression and Smoothing Scatterplots. *Journal of the American Statistical Association*, 74(368), 829–836. <https://doi.org/10.1080/01621459.1979.10481038>
- Coe, M. T. (2000). Modeling terrestrial hydrological systems at the continental scale: Testing the accuracy of an atmospheric GCM. *Journal of Climate*, 13(4), 686–704. [https://doi.org/10.1175/1520-0442\(2000\)013<0686:MTHSAT>2.0.CO;2](https://doi.org/10.1175/1520-0442(2000)013<0686:MTHSAT>2.0.CO;2)
- Cook, B. I., Ault, T. R., & Smerdon, J. E. (2015). Unprecedented 21st century drought risk in the American Southwest and Central Plains. *Science Advances*, 1(1). Retrieved from <http://advances.sciencemag.org/content/1/1/e1400082.abstract>
- Costa-Cabral, M. C., Richey, J. E., Goteti, G., Lettenmaier, D. P., Feldkötter, C., & Snidvongs, A. (2008). Landscape structure and use, climate, and water movement in the Mekong River basin. *Hydrological Processes*, 22(12), 1731–1746. <https://doi.org/10.1002/hyp.6740>

- Dang, T. D., Cochrane, T. A., Arias, M. E., & Tri, V. P. D. (2018). Future hydrological alterations in the Mekong Delta under the impact of water resources development, land subsidence and sea level rise. *Journal of Hydrology: Regional Studies*, 15, 119–133. <https://doi.org/10.1016/j.ejrh.2017.12.002>
- Degu, A. M., Hossain, F., Niyogi, D., Pielke, R., Shepherd, J. M., Voisin, N., & Chronis, T. (2011). The influence of large dams on surrounding climate and precipitation patterns. *Geophysical Research Letters*, 38(4). <https://doi.org/10.1029/2010GL046482>
- Döll, P., Kaspar, F., & Lehner, B. (2003). A global hydrological model for deriving water availability indicators: Model tuning and validation. *Journal of Hydrology*, 270(1–2), 105–134. [https://doi.org/10.1016/S0022-1694\(02\)00283-4](https://doi.org/10.1016/S0022-1694(02)00283-4)
- Doyle, M. W., Stanley, E. H., Orr, C. H., Selle, A. R., Sethi, S. A., & Harbor, J. M. (2005). Stream ecosystem response to small dam removal: Lessons from the Heartland. *Geomorphology*, 71(1–2), 227–244. <https://doi.org/10.1016/j.geomorph.2004.04.011>
- Dynesius, M., & Nilsson, C. (1994). Fragmentation and flow regulation of river systems in the northern third of the world. *Science*, 266. <https://doi.org/10.1126/science.266.5186.753>
- Ehsani, N., Fekete, B. M., Vörösmarty, C. J., & Tessler, Z. D. (2016). A neural network based general reservoir operation scheme. *Stochastic Environmental Research and Risk Assessment*, 30(4), 1151–1166. <https://doi.org/10.1007/s00477-015-1147-9>
- Eiríksdóttir, E. S., Oelkers, E. H., Hardardóttir, J., & Gislason, S. R. (2017). The impact of damming on riverine fluxes to the ocean: A case study from Eastern Iceland. *Water Research*, 113, 124–138. <https://doi.org/10.1016/j.watres.2016.12.029>
- Fan, Y., & Miguez-Macho, G. (2011). A simple hydrologic framework for simulating wetlands in climate and earth system models. *Climate Dynamics*, 37(1), 253–278. <https://doi.org/10.1007/s00382-010-0829-8>
- Fan, Y., Miguez-Macho, G., Weaver, C. P., Walko, R., & Robock, A. (2007). Incorporating water table dynamics in climate modeling: 1. Water table observations and equilibrium water table simulations. *Journal of Geophysical Research Atmospheres*, 112(10), D10125. <https://doi.org/10.1029/2006JD008111>
- Fan, Y., Miguez-Macho, G., Jobbágy, E. G., Jackson, R. B., & Otero-Casal, C. (2017). Hydrologic regulation of plant rooting depth. *Proceedings of the National Academy of Sciences*, 114(40), 10572 LP – 10577. Retrieved from <http://www.pnas.org/content/114/40/10572.abstract>
- Fatichi, S., Vivoni, E. R., Ogden, F. L., Ivanov, V. Y., Mirus, B., Gochis, D., et al. (2016). An overview of current applications, challenges, and future trends in distributed process-based models in hydrology, 537, 45–60. <https://doi.org/10.1016/j.jhydrol.2016.03.026>
- Fawthrop, T. (2018). *Leaked report warns Cambodia's biggest dam could "literally kill" Mekong river.* London. Retrieved from

<https://www.theguardian.com/environment/2018/may/16/leaked-report-warns-cambodias-biggest-dam-could-literally-kill-mekong-river>

- Fearnside, P. M., & Pueyo, S. (2012). Greenhouse-gas emissions from tropical dams. *Nature Climate Change*, 2(6), 382–384. <https://doi.org/10.1038/nclimate1540>
- Felfelani, F., Wada, Y., Longuevergne, L., & Pokhrel, Y. (2017). Natural and human-induced terrestrial water storage change: A global analysis using hydrological models and GRACE. *Journal of Hydrology*, 553, 105–118. <https://doi.org/10.1016/j.jhydrol.2017.07.048>
- Fleischmann, A., Paiva, R., & Collischonn, W. (2019). Can regional to continental river hydrodynamic models be locally relevant? A cross-scale comparison. *Journal of Hydrology X*, 3, 100027. <https://doi.org/10.1016/j.hydroa.2019.100027>
- Frappart, F., Minh, K. D., L’Hermitte, J., Cazenave, A., Ramillien, G., Le Toan, T., & Mognard-Campbell, N. (2006). Water volume change in the lower Mekong from satellite altimetry and imagery data. *Geophysical Journal International*, 167(2), 570–584. <https://doi.org/10.1111/j.1365-246X.2006.03184.x>
- Gao, H. (2015). Satellite remote sensing of large lakes and reservoirs: from elevation and area to storage. *Wiley Interdisciplinary Reviews: Water*, 2(2), 147–157. <https://doi.org/10.1002/wat2.1065>
- Gernaat, D. E. H. J., Bogaart, P. W., Vuuren, D. P. van, Biemans, H., & Niessink, R. (2017). High-resolution assessment of global technical and economic hydropower potential. *Nature Energy*, 2(10), 821–828. <https://doi.org/10.1038/s41560-017-0006-y>
- Gong, L., Halldin, S., & Xu, C. Y. (2011). Global-scale river routing-an efficient time-delay algorithm based on HydroSHEDS high-resolution hydrography. *Hydrological Processes*, 25(7), 1114–1128. <https://doi.org/10.1002/hyp.7795>
- Graf, W. L. (1999). Dam nation: A geographic census of american dams and their large-scale hydrologic impacts. *Water Resources Research*, 35(4), 1305–1311. <https://doi.org/10.1029/1999WR900016>
- Gran, K. B., Belmont, P., Day, S. S., Jennings, C., Johnson, A., Perg, L., & Wilcock, P. R. (2009). Geomorphic evolution of the Le Sueur River, Minnesota, USA, and implications for current sediment loading. In L. A. James, S. L. Rathburn, & G. R. Whittecar (Eds.), *Management and Restoration of Fluvial Systems with Broad Historical Changes and Human Impacts*. Geological Society of America. Retrieved from [https://doi.org/10.1130/2009.2451\(08\)](https://doi.org/10.1130/2009.2451(08))
- Greathouse, E. A., Pringle, C. M., & Holmquist, J. G. (2006). Conservation and management of migratory fauna: dams in tropical streams of Puerto Rico. *Aquatic Conservation: Marine and Freshwater Ecosystems*, 16(7), 695–712. <https://doi.org/10.1002/aqc.804>

- Grumbine, R. E., & Xu, J. (2011). Mekong Hydropower Development. *Science*, 332(6026), 178 LP – 179. Retrieved from <http://science.sciencemag.org/content/332/6026/178.abstract>
- Gupta, H., Kao, S. J., & Dai, M. (2012). The role of mega dams in reducing sediment fluxes: A case study of large Asian rivers. *Journal of Hydrology*, 464–465, 447–458. <https://doi.org/10.1016/j.jhydrol.2012.07.038>
- Haddeland, I., Skaugen, T., & Lettenmaier, D. P. (2006). Anthropogenic impacts on continental surface water fluxes. *Geophysical Research Letters*, 33(8), L08406. <https://doi.org/10.1029/2006GL026047>
- Hanasaki, N., Kanae, S., & Oki, T. (2006). A reservoir operation scheme for global river routing models. *Journal of Hydrology*, 327(1–2), 22–41. <https://doi.org/10.1016/j.jhydrol.2005.11.011>
- Hanasaki, N., Yoshikawa, S., Pokhrel, Y., & Kanae, S. (2018). A global hydrological simulation to specify the sources of water used by humans. *Hydrol. Earth Syst. Sci.*, 22(1), 789–817. <https://doi.org/10.5194/hess-22-789-2018>
- Hejazi, M. I., Voisin, N., Liu, L., Bramer, L. M., Fortin, D. C., Hathaway, J. E., et al. (2015). 21st century United States emissions mitigation could increase water stress more than the climate change it is mitigating. *Proceedings of the National Academy of Sciences*, 112(34), 10635–10640. <https://doi.org/10.1073/pnas.1421675112>
- Hoes, O. A. C., Meijer, L. J. J., van der Ent, R. J., & van de Giesen, N. C. (2017). Systematic high-resolution assessment of global hydropower potential. *PLOS ONE*, 12(2), e0171844. <https://doi.org/10.1371/journal.pone.0171844>
- Holdren, G. C., & Turner, K. (2010). Characteristics of Lake Mead, Arizona-Nevada. *Lake and Reservoir Management*, 26(4), 230–239. <https://doi.org/10.1080/07438141.2010.540699>
- Hossain, F. (2010). Empirical Relationship between Large Dams and the Alteration in Extreme Precipitation. *World*, 11(3), 97–101. [https://doi.org/10.1061/\(asce\)nh.1527-6996.0000013](https://doi.org/10.1061/(asce)nh.1527-6996.0000013)
- Hossain, F., Jeyachandran, I., & Pielke, R. (2010). Dam safety effects due to human alteration of extreme precipitation. *Water Resources Research*, 46(3). <https://doi.org/10.1029/2009WR007704>
- Hossain, F., Degu, A. M., Yigzaw, W., Burian, S., Niyogi, D., Shepherd, J. M., & Pielke, R. (2012). Climate Feedback–Based Provisions for Dam Design, Operations, and Water Management in the 21st Century. *Journal of Hydrologic Engineering*, 17(8), 837–850. [https://doi.org/10.1061/\(ASCE\)HE.1943-5584.0000541](https://doi.org/10.1061/(ASCE)HE.1943-5584.0000541)
- Huang, W.-C., Yuan, L.-C., & Lee, C.-M. (2002). Linking genetic algorithms with stochastic dynamic programming to the long-term operation of a multireservoir system. *Water Resources Research*, 38(12), 40–1–40–9. <https://doi.org/10.1029/2001WR001122>

- Hung, N. N., Delgado, J. M., Tri, V. K., Hung, L. M., Merz, B., Bárdossy, A., & Apel, H. (2012). Floodplain hydrology of the Mekong Delta, Vietnam. *Hydrological Processes*, 26(5), 674–686. <https://doi.org/10.1002/hyp.8183>
- Inomata, H., & Fukami, K. (2008). Restoration of historical hydrological data of Tonle Sap Lake and its surrounding areas. *Hydrological Processes*, 22(9), 1337–1350. <https://doi.org/10.1002/hyp.6943>
- Junk, W. J., Bayley, P. B., & Sparks, R. E. (1989). The flood-pulse concept in river-floodplain systems. In D. P. Dodge (Ed.), *Proceedings of the International Large River Symposium (LARS)* (pp. 110–127). Canadian Special Publication of Fisheries and Aquatic Sciences 106.
- Kemenes, A., Forsberg, B. R., & Melack, J. M. (2007). Methane release below a tropical hydroelectric dam. *Geophysical Research Letters*, 34(12), 1–5. <https://doi.org/10.1029/2007GL029479>
- Kesel, R. H., Dunne, K. C., McDonald, R. C., Allison, K. R., & Spicer, B. E. (1974). Lateral erosion and overbank deposition on the Mississippi River in Louisiana caused by 1973 flooding. *Geology*, 2(9), 461–464. [https://doi.org/10.1130/0091-7613\(1974\)2<461:LEAODO>2.0.CO;2](https://doi.org/10.1130/0091-7613(1974)2<461:LEAODO>2.0.CO;2)
- Kummu, M., & Sarkkula, J. (2008). Impact of the Mekong River flow alteration on the Tonle Sap flood pulse. *Ambio*, 37(3), 185–192. [https://doi.org/10.1579/0044-7447\(2008\)37\[185:IOTMRF\]2.0.CO;2](https://doi.org/10.1579/0044-7447(2008)37[185:IOTMRF]2.0.CO;2)
- Labadie, J. W. (2004). Optimal Operation of Multireservoir Systems: State-of-the-Art Review. *Journal of Water Resources Planning and Management*, 130(2), 93–111. [https://doi.org/10.1061/\(ASCE\)0733-9496\(2004\)130:2\(93\)](https://doi.org/10.1061/(ASCE)0733-9496(2004)130:2(93))
- Lauri, H., de Moel, H., Ward, P. J., Räsänen, T. A., Keskinen, M., & Kummu, M. (2012). Future changes in Mekong River hydrology: impact of climate change and reservoir operation on discharge. *Hydrology and Earth System Sciences*, 16(12), 4603–4619. <https://doi.org/10.5194/hess-16-4603-2012>
- Lehner, B., & Döll, P. (2004). Development and validation of a global database of lakes, reservoirs and wetlands. *Journal of Hydrology*, 296(1–4), 1–22. <https://doi.org/10.1016/j.jhydrol.2004.03.028>
- Lehner, B., Verdin, K., & Jarvis, A. (2008). New Global Hydrography Derived From Spaceborne Elevation Data. *Eos, Transactions American Geophysical Union*, 89(10), 93–94. <https://doi.org/10.1029/2008EO100001>
- Lehner, B., Reidy Liermann, C., Revenga, C., Vorosmarty, C., Fekete, B., Crouzet, P., et al. (2011a). Global Reservoir and Dam Database, Version 1 (GRanDv1): Dams, Revision 01. NASA Socioeconomic Data and Applications Center (SEDAC). Retrieved from <http://dx.doi.org/10.7927/H4N877QK>

- Lehner, B., Reidy Liermann, C., Revenga, C., Vorosmarty, C., Fekete, B., Crouzet, P., et al. (2011b). High-Resolution Mapping of the World's Reservoirs and Dams for Sustainable River-Flow Management. *Frontiers in Ecology and the Environment*, 9, 494–502. Retrieved from <http://dx.doi.org/10.1890/100125>
- Li, Y., Gao, H., Jasinski, M. F., Zhang, S., & Stoll, J. D. (2019). Deriving High-Resolution Reservoir Bathymetry From ICESat-2 Prototype Photon-Counting Lidar and Landsat Imagery. *IEEE Transactions on Geoscience and Remote Sensing*, 1–11. <https://doi.org/10.1109/TGRS.2019.2917012>
- Liebe, J., van de Giesen, N., & Andreini, M. (2005). Estimation of small reservoir storage capacities in a semi-arid environment: A case study in the Upper East Region of Ghana. *Integrated Water Resource Assessment*, 30(6), 448–454. <https://doi.org/10.1016/j.pce.2005.06.011>
- Ligon, F. K., Dietrich, W. E., & Trush, W. J. (1995). Downstream Ecological Effects of Dams. *BioScience*, 45(3), 183–192. <https://doi.org/10.2307/1312557>
- Mateo, C. M., Hanasaki, N., Komori, D., Tanaka, K., Kiguchi, M., Champathong, A., et al. (2014). Assessing the impacts of reservoir operation to floodplain inundation by combining hydrological, reservoir management, and hydrodynamic models. *Water Resources Research*, 50(9), 7245–7266. <https://doi.org/10.1002/2013WR014845>
- Maupin, M. A., Kenny, J. F., Hutson, S. S., Lovelace, J. K., Barber, N. L., & Linsey, K. S. (2014). *Estimated use of water in the United States in 2010: U.S. Geological Survey Circular 1405* (p. 56). Retrieved from <https://dx.doi.org/10.3133/cir1405>
- Mccabe, M. F., Aragon, B., Houborg, R., & Mascaro, J. (2017). CubeSats in Hydrology: Ultrahigh-Resolution Insights Into Vegetation Dynamics and Terrestrial Evaporation. *Water Resources Research*, in review. <https://doi.org/10.1002/2017WR022240>
- McCully, P. (2001). *Silenced rivers: the ecology and politics of large dams* (Enl. and u). New York;London; Zed Books.
- Meigh, J. R., McKenzie, A. A., & Sene, K. J. (1999). A grid-based approach to water scarcity estimates for eastern and southern Africa. *Water Resources Management*, 13(2), 85–115. <https://doi.org/10.1023/A:1008025703712>
- Mekong River Commission. (2005). *Overview of the Hydrology of the Mekong Basin*. Vientiane.
- Mekong River Commission. (2010). *Impacts on the Tonle Sap Ecosystem*. Vientiane.
- Mesinger, F., DiMego, G., Kalnay, E., Mitchell, K., Shafran, P. C., Ebisuzaki, W., et al. (2006). North American Regional Reanalysis. *Bulletin of the American Meteorological Society*, 87(3), 343–360. <https://doi.org/10.1175/BAMS-87-3-343>

- Miguez-Macho, G., & Fan, Y. (2012a). The role of groundwater in the Amazon water cycle: 1. Influence on seasonal streamflow, flooding and wetlands. *Journal of Geophysical Research Atmospheres*, 117(15). <https://doi.org/10.1029/2012JD017539>
- Miguez-Macho, G., & Fan, Y. (2012b). The role of groundwater in the Amazon water cycle: 2. Influence on seasonal soil moisture and evapotranspiration. *Journal of Geophysical Research Atmospheres*, 117(15), D15114. <https://doi.org/10.1029/2012JD017540>
- Miguez-Macho, G., Fan, Y., Weaver, C. P., Walko, R., & Robock, A. (2007). Incorporating water table dynamics in climate modeling: 2. Formulation, validation, and soil moisture simulation. *Journal of Geophysical Research Atmospheres*, 112(13), 1–16. <https://doi.org/10.1029/2006JD008112>
- Minh, H. V. T., Kurasaki, M., Ty, T. V., Tran, D. Q., Le, K. N., Avtar, R., et al. (2019). Effects of Multi-Dike Protection Systems on Surface Water Quality in the Vietnamese Mekong Delta. *Water*, 11(5), 1010. <https://doi.org/10.3390/w11051010>
- Neal, J., Schumann, G., & Bates, P. (2012). A subgrid channel model for simulating river hydraulics and floodplain inundation over large and data sparse areas. *Water Resources Research*, 48(11). <https://doi.org/10.1029/2012WR012514>
- Nilsson, C., Reidy, C. A., Dynesius, M., & Revenga, C. (2005). Fragmentation and flow regulation of the world's large river systems. *Science*, 308. <https://doi.org/10.1126/science.1107887>
- Null, S. E., Medellín-Azuara, J., Escrivá-Bou, A., Lent, M., & Lund, J. R. (2014). Optimizing the dammed: Water supply losses and fish habitat gains from dam removal in California. *Journal of Environmental Management*, 136, 121–131. <https://doi.org/10.1016/j.jenvman.2014.01.024>
- Oki, T., & Kanae, S. (2006). Global Hydrological Cycles and World Water Resources. *Science*, 313(5790), 1068–1072. <https://doi.org/10.1126/science.1128845>
- Oki, Taikan, & Sud, Y. C. (1998). Design of Total Runoff Integrating Pathways (TRIP)—A Global River Channel Network. *Earth Interactions*, 2(1), 1–37. [https://doi.org/10.1175/1087-3562\(1998\)002<0001:DOTRIP>2.3.CO;2](https://doi.org/10.1175/1087-3562(1998)002<0001:DOTRIP>2.3.CO;2)
- Pekel, J.-F., Cottam, A., Gorelick, N., & Belward, A. S. (2016). High-resolution mapping of global surface water and its long-term changes. *Nature*, 540(7633), 418–422. <https://doi.org/10.1038/nature20584>
- Piman, T., Lennaerts, T., & Southalack, P. (2013). Assessment of hydrological changes in the lower Mekong Basin from Basin-Wide development scenarios. *Hydrological Processes*, 27(15), 2115–2125. <https://doi.org/10.1002/hyp.9764>
- Poff, N. L., Allan, J. D., Bain, M. B., Karr, J. R., Prestegard, K. L., Richter, B. D., et al. (1997). The natural flow regime. *BioScience*, 47(11). <https://doi.org/10.2307/1313099>

- Pohl, M. M. (2002). Bringing Down Our Dams: Trends in American Dam Removal Rationales. *Journal of the American Water Resources Association*, 38(6), 1511–1519. <https://doi.org/10.1111/j.1752-1688.2002.tb04361.x>
- Pokhrel, Y., Hanasaki, N., Koirala, S., Cho, J., Yeh, P. J.-F., Kim, H., et al. (2012). Incorporating Anthropogenic Water Regulation Modules into a Land Surface Model. *Journal of Hydrometeorology*, 13(1), 255–269. <https://doi.org/10.1175/JHM-D-11-013.1>
- Pokhrel, Y., Hanasaki, N., Yeh, P. J. F., Yamada, T. J., Kanae, S., & Oki, T. (2012). Model estimates of sea-level change due to anthropogenic impacts on terrestrial water storage. *Nature Geoscience*, 5(6), 389–392. <https://doi.org/10.1038/ngeo1476>
- Pokhrel, Y., Fan, Y., Miguez-Macho, G., Yeh, P. J. F., & Han, S. C. (2013). The role of groundwater in the Amazon water cycle: 3. Influence on terrestrial water storage computations and comparison with GRACE. *Journal of Geophysical Research Atmospheres*, 118(8), 3233–3244. <https://doi.org/10.1002/jgrd.50335>
- Pokhrel, Y., Fan, Y., & Miguez-Macho, G. (2014). Potential hydrologic changes in the Amazon by the end of the 21st century and the groundwater buffer. *Environmental Research Letters*, 9(8), 084004. <https://doi.org/10.1088/1748-9326/9/8/084004>
- Pokhrel, Y., Koirala, S., Yeh, P. J.-F., Hanasaki, N., Longuevergne, L., Kanae, S., & Oki, T. (2015). Incorporation of groundwater pumping in a global Land Surface Model with the representation of human impacts. *Water Resources Research*, 51(1), 78–96. <https://doi.org/10.1002/2014WR015602>
- Pokhrel, Y., Hanasaki, N., Wada, Y., & Kim, H. (2016). Recent progresses in incorporating human land–water management into global land surface models toward their integration into Earth system models. *Wiley Interdisciplinary Reviews: Water*, 3(4), 548–574. <https://doi.org/10.1002/wat2.1150>
- Pokhrel, Y., Felfelani, F., Shin, S., Yamada, T. J., & Satoh, Y. (2017). Modeling large-scale human alteration of land surface hydrology and climate. *Geoscience Letters*, 4(1), 10. <https://doi.org/10.1186/s40562-017-0076-5>
- Pokhrel, Y., Burbano, M., Roush, J., Kang, H., Sridhar, V., & Hyndman, D. (2018). A Review of the Integrated Effects of Changing Climate, Land Use, and Dams on Mekong River Hydrology. *Water*, 10(3), 266. <https://doi.org/10.3390/w10030266>
- Pokhrel, Y. N., Koirala, S., Yeh, P. J.-F., Hanasaki, N., Longuevergne, L., Kanae, S., & Oki, T. (2015). Incorporation of groundwater pumping in a global Land Surface Model with the representation of human impacts. *Water Resources Research*, 51(1), 78–96. <https://doi.org/10.1002/2014WR015602>
- Postel, S. L., Daily, G. C., & Ehrlich, P. R. (1996). Human appropriation of renewable fresh water. *Science*, 271(5250), 785–788. <https://doi.org/10.1126/science.271.5250.785>

- Rajagopalan, B., Nowak, K., Prairie, J., Hoerling, M., Harding, B., Barsugli, J., et al. (2009). Water supply risk on the Colorado River: Can management mitigate? *Water Resources Research*, 45(8), 1–7. <https://doi.org/10.1029/2008WR007652>
- Räsänen, T. A., Koponen, J., Lauri, H., & Kummu, M. (2012). Downstream Hydrological Impacts of Hydropower Development in the Upper Mekong Basin. *Water Resources Management*, 26(12), 3495–3513. <https://doi.org/10.1007/s11269-012-0087-0>
- Räsänen, T. A., Someth, P., Lauri, H., Koponen, J., Sarkkula, J., & Kummu, M. (2017). Observed river discharge changes due to hydropower operations in the Upper Mekong Basin. *Journal of Hydrology*, 545, 28–41. <https://doi.org/10.1016/j.jhydrol.2016.12.023>
- Renwick, W. H., Smith, S. V., Bartley, J. D., & Buddemeier, R. W. (2005). The role of impoundments in the sediment budget of the conterminous United States. *Geomorphology*, 71(1–2), 99–111. <https://doi.org/10.1016/j.geomorph.2004.01.010>
- Sabo, J. L., Ruhi, A., Holtgrieve, G. W., Elliott, V., Arias, M. E., Ngor, P. B., et al. (2017). Designing river flows to improve food security futures in the Lower Mekong Basin. *Science*, 358(6368), eaao1053. <https://doi.org/10.1126/science.aao1053>
- Sakamoto, T., Van Nguyen, N., Kotera, A., Ohno, H., Ishitsuka, N., & Yokozawa, M. (2007). Detecting temporal changes in the extent of annual flooding within the Cambodia and the Vietnamese Mekong Delta from MODIS time-series imagery. *Remote Sensing of Environment*, 109(3), 295–313. <https://doi.org/10.1016/j.rse.2007.01.011>
- Scanlon, B. R., Zhang, Z., Save, H., Wiese, D. N., Landerer, F. W., Long, D., et al. (2016). Global evaluation of new GRACE mascon products for hydrologic applications. *Water Resources Research*, 52(12), 9412–9429. <https://doi.org/10.1002/2016WR019494>
- Schmidt, C. (2015). Alarm over a sinking delta. *Science*, 348(6237), 845 LP – 846. Retrieved from <http://science.sciencemag.org/content/348/6237/845.abstract>
- Schmitt, R. J. P., Bizzi, S., Castelletti, A., & Kondolf, G. M. (2018). Improved trade-offs of hydropower and sand connectivity by strategic dam planning in the Mekong. *Nature Sustainability*, 1(2), 96–104. <https://doi.org/10.1038/s41893-018-0022-3>
- Shin, S., & Paik, K. (2017). An improved method for single flow direction calculation in grid digital elevation models. *Hydrological Processes*, 31(8), 1650–1661. <https://doi.org/10.1002/hyp.11135>
- Shuai, P., Cardenas, M. B., Knappett, P. S. K., Bennett, P. C., & Neilson, B. T. (2017). Denitrification in the banks of fluctuating rivers: The effects of river stage amplitude, sediment hydraulic conductivity and dispersivity, and ambient groundwater flow. *Water Resources Research*, 53(9), 7951–7967. <https://doi.org/10.1002/2017WR020610>
- Smajgl, A., Toan, T. Q., Nhan, D. K., Ward, J., Trung, N. H., Tri, L. Q., et al. (2015). Responding to rising sea levels in the Mekong Delta. *Nature Climate Change*, 5(2), 167–174. <https://doi.org/10.1038/nclimate2469>

- Smajgl, Alex, Ward, J. R., Foran, T., Dore, J., & Larson, S. (2015). Visions, beliefs, and transformation : exploring cross-sector and transboundary dynamics in the wider Mekong region. *Ecology and Society*, 20(2). <https://doi.org/10.5751/ES-07421-200215>
- Solander, K. C., Reager, J. T., Thomas, B. F., David, C. H., & Famiglietti, J. S. (2016). Simulating Human Water Regulation: The Development of an Optimal Complexity, Climate-Adaptive Reservoir Management Model for an LSM. *Journal of Hydrometeorology*, 17(3), 725–744. <https://doi.org/10.1175/JHM-D-15-0056.1>
- Sridhar, V., Kang, H., & Ali, S. A. (2019). Human-Induced Alterations to Land Use and Climate and Their Responses for Hydrology and Water Management in the Mekong River Basin. *Water*, 11(6), 1307. <https://doi.org/10.3390/w11061307>
- Stone, R. (2016). Dam-building threatens Mekong fisheries. *Science*, 354(6316), 1084–1085. <https://doi.org/10.1126/science.354.6316.1084>
- Syed, T. H., Famiglietti, J. S., & Chambers, D. P. (2009). GRACE-Based Estimates of Terrestrial Freshwater Discharge from Basin to Continental Scales. *Journal of Hydrometeorology*, 10(1), 22–40. <https://doi.org/10.1175/2008JHM993.1>
- Syvitski, J. P. M., Vörösmarty, C. J., Kettner, A. J., & Green, P. (2005). Impact of humans on the flux of terrestrial sediment to the global coastal ocean. *Science*, 308(5720), 376–380. <https://doi.org/10.1126/science.1109454>
- Syvitski, J. P. M., Kettner, A. J., Overeem, I., Hutton, E. W. H., Hannon, M. T., Brakenridge, G. R., et al. (2009). Sinking deltas due to human activities. *Nature Geoscience*, 2(10), 681–686. <https://doi.org/10.1038/ngeo629>
- Taeb, A., Reager, J. T., Turmon, M., & Chandrasekaran, V. (2017). A Statistical Graphical Model of the California Reservoir System. *Water Resources Research*. <https://doi.org/10.1002/2017WR020412>
- Takata, K., Emori, S., & Watanabe, T. (2003). Development of the minimal advanced treatments of surface interaction and runoff. *Global and Planetary Change*, 38(1–2), 209–222. [https://doi.org/10.1016/S0921-8181\(03\)00030-4](https://doi.org/10.1016/S0921-8181(03)00030-4)
- Tanner, W. F. (1971). The River Profile. *The Journal of Geology*, 79(4), 482–492. <https://doi.org/10.1086/627653>
- Tapley, B. D. (2004). GRACE Measurements of Mass Variability in the Earth System. *Science*, 305(5683), 503–505. <https://doi.org/10.1126/science.1099192>
- Timpe, K., & Kaplan, D. (2017). The changing hydrology of a dammed Amazon. *Science Advances*, 3(11), e1700611. <https://doi.org/10.1126/sciadv.1700611>
- Trung, L. D., Duc, N. A., Nguyen, L. T., Thai, T. H., Khan, A., Rautenstrauch, K., & Schmidt, C. (2018). Assessing cumulative impacts of the proposed Lower Mekong Basin hydropower cascade on the Mekong River floodplains and Delta – Overview of

- integrated modeling methods and results. *Journal of Hydrology*. <https://doi.org/10.1016/j.jhydrol.2018.01.029>
- Tušer, M., Pícek, T., Sajdlová, Z., Jůza, T., Muška, M., & Frouzová, J. (2017). Seasonal and Spatial Dynamics of Gas Ebullition in a Temperate Water-Storage Reservoir. *Water Resources Research*, 53(10), 8266–8276. <https://doi.org/10.1002/2017WR020694>
- Urbazaev, M., Cremer, F., Migliavacca, M., Reichstein, M., Schmullius, C., & Thiel, C. (2018). Potential of Multi-Temporal ALOS-2 PALSAR-2 ScanSAR Data for Vegetation Height Estimation in Tropical Forests of Mexico. *Remote Sensing*, 10(8), 1277. <https://doi.org/10.3390/rs10081277>
- Veldkamp, T. I. E., Wada, Y., Aerts, J. C. J. H., Döll, P., Gosling, S. N., Liu, J., et al. (2017). Water scarcity hotspots travel downstream due to human interventions in the 20th and 21st century. *Nature Communications*, 8. <https://doi.org/10.1038/ncomms15697>
- Voisin, N., Hejazi, M. I., Leung, L. R., Liu, L., Huang, M., Li, H. Y., & Tesfa, T. (2017). Effects of spatially distributed sectoral water management on the redistribution of water resources in an integrated water model. *Water Resources Research*, 53(5), 4253–4270. <https://doi.org/10.1002/2016WR019767>
- Voisin, Nathalie., Li, H., Ward, D., Huang, M., Wigmosta, M., & Leung, L. R. (2013). On an improved sub-regional water resources management representation for integration into earth system models. *Hydrology and Earth System Sciences*, 17(9), 3605–3622. <https://doi.org/10.5194/hess-17-3605-2013>
- Vörösmarty, C. J., Sharma, K. P., Fekete, B. M., Copeland, A. H., Holden, J., Marble, J., & Lough, J. A. (1997). *The storage and aging of continental runoff in large reservoir systems of the world*. (F. A. O. of the UN, Ed.) (Vol. 26).
- Vörösmarty, C. J., Meybeck, M., Fekete, B., Sharma, K., Green, P., & Syvitski, J. P. M. (2003). Anthropogenic sediment retention: major global impact from registered river impoundments. *The Supply of Flux of Sediment along Hydrological Pathways: Anthropogenic Influences at the Global Scale*, 39(1), 169–190. [https://doi.org/10.1016/S0921-8181\(03\)00023-7](https://doi.org/10.1016/S0921-8181(03)00023-7)
- Vörösmarty, C. J., McIntyre, P. B., Gessner, M. O., Dudgeon, D., Prusevich, A., Green, P., et al. (2010). Global threats to human water security and river biodiversity. *Nature*, 467(7315), 555–561. <https://doi.org/10.1038/nature09440>
- Wada, Y., Wisser, D., & Bierkens, M. F. P. (2014). Global modeling of withdrawal, allocation and consumptive use of surface water and groundwater resources. *Earth System Dynamics*, 5(1), 15–40. <https://doi.org/10.5194/esd-5-15-2014>
- Wada, Y., de Graaf, E. M. I., & van Beek, P. H. L. (2016). High-resolution modeling of human and climate impacts on global water resources. *Journal of Advances in Modeling Earth Systems*, 8(2), 735–763. <https://doi.org/10.1002/2015MS000618>

- Wada, Y., Reager, J. T., Chao, B. F., Wang, J., Lo, M. H., Song, C., et al. (2016). Recent Changes in Land Water Storage and its Contribution to Sea Level Variations. *Surveys in Geophysics*, 38(1), 1–22. <https://doi.org/10.1007/s10712-016-9399-6>
- Wada, Y., Bierkens, M. F. P., de Roo, A., Dirmeyer, P. A., Famiglietti, J. S., Hanasaki, N., et al. (2017). Human–water interface in hydrological modelling: current status and future directions. *Hydrology and Earth System Sciences*, 21(8), 4169–4193. <https://doi.org/10.5194/hess-21-4169-2017>
- Walko, R. L., Band, L. E., Jill Baron, 2, F Kittel, T. G., Lammers, R., Lee, T. J., et al. (2000). Coupled Atmosphere–Biophysics–Hydrology Models for Environmental Modeling. *Journal of Applied Meteorology*, 39(6), 931–944. [https://doi.org/10.1175/1520-0450\(2000\)039<0931:CABHMF>2.0.CO;2](https://doi.org/10.1175/1520-0450(2000)039<0931:CABHMF>2.0.CO;2)
- Wang, S., Qian, X., Han, B. P., Luo, L. C., & Hamilton, D. P. (2012). Effects of local climate and hydrological conditions on the thermal regime of a reservoir at Tropic of Cancer, in southern China. *Water Research*, 46(8), 2591–2604. <https://doi.org/10.1016/j.watres.2012.02.014>
- Wang, W., Lu, H., Yang, D., Sothea, K., Jiao, Y., Gao, B., et al. (2016). Modelling Hydrologic Processes in the Mekong River Basin Using a Distributed Model Driven by Satellite Precipitation and Rain Gauge Observations. *PLOS ONE*, 11(3), e0152229. <https://doi.org/10.1371/journal.pone.0152229>
- Wang, W., Lu, H., Ruby Leung, L., Li, H.-Y., Zhao, J., Tian, F., et al. (2017). Dam Construction in Lancang-Mekong River Basin Could Mitigate Future Flood Risk From Warming-Induced Intensified Rainfall. *Geophysical Research Letters*, 44(20), 10,378–10,386. <https://doi.org/10.1002/2017GL075037>
- Weron, R. (2014). Electricity price forecasting: A review of the state-of-the-art with a look into the future. *International Journal of Forecasting*, 30(4), 1030–1081. <https://doi.org/10.1016/j.ijforecast.2014.08.008>
- Wild, T. B., & Loucks, D. P. (2014). Managing flow, sediment, and hydropower regimes in the Sre Pok, Se San, and Se Kong Rivers of the Mekong basin. *Water Resources Research*, 50(6), 5141–5157. <https://doi.org/10.1002/2014WR015457>
- Winemiller, K. O., McIntyre, P. B., Castello, L., Fluet-Chouinard, E., Giarrizzo, T., Nam, S., et al. (2016). Balancing hydropower and biodiversity in the Amazon, Congo, and Mekong. *Science*, 351(6269), 128–129. <https://doi.org/10.1126/science.aac7082>
- Wisser, D., Fekete, B. M., Vörösmarty, C. J., & Schumann, A. H. (2010). Reconstructing 20th century global hydrography: a contribution to the Global Terrestrial Network- Hydrology (GTN-H). *Hydrology and Earth System Sciences*, 14(1), 1–24. <https://doi.org/10.5194/hess-14-1-2010>

- Woldemichael, A. T., Hossain, F., Pielke, R., & Beltrán-Przekurat, A. (2012). Understanding the impact of dam-triggered land use/land cover change on the modification of extreme precipitation. *Water Resources Research*, 48(9). <https://doi.org/10.1029/2011WR011684>
- Wood, E. F., Roundy, J. K., Troy, T. J., van Beek, L. P. H., Bierkens, M. F. P., Blyth, E., et al. (2011). Hyperresolution global land surface modeling: Meeting a grand challenge for monitoring Earth's terrestrial water. *Water Resources Research*, 47(5). <https://doi.org/10.1029/2010WR010090>
- Xue, Z., Liu, J. P., & Ge, Q. (2011). Changes in hydrology and sediment delivery of the Mekong River in the last 50 years: Connection to damming, monsoon, and ENSO. *Earth Surface Processes and Landforms*, 36(3), 296–308. <https://doi.org/10.1002/esp.2036>
- Yamagata, Y., Hanasaki, N., Ito, A., Kinoshita, T., Murakami, D., & Zhou, Q. (2018). Estimating water–food–ecosystem trade-offs for the global negative emission scenario (IPCC-RCP2.6). *Sustainability Science*, 13(2), 301–313. <https://doi.org/10.1007/s11625-017-0522-5>
- Yamazaki, D., Oki, T., & Kanae, S. (2009). Deriving a global river network map and its sub-grid topographic characteristics from a fine-resolution flow direction map. *Hydrology and Earth System Sciences*, 13(11), 2241–2251. <https://doi.org/10.5194/hess-13-2241-2009>
- Yamazaki, D., Kanae, S., Kim, H., & Oki, T. (2011). A physically based description of floodplain inundation dynamics in a global river routing model. *Water Resources Research*, 47(4), 1–21. <https://doi.org/10.1029/2010WR009726>
- Yamazaki, D., Baugh, C. A., Bates, P. D., Kanae, S., Alsdorf, D. E., & Oki, T. (2012). Adjustment of a spaceborne DEM for use in floodplain hydrodynamic modeling. *Journal of Hydrology*, 436–437, 81–91. <https://doi.org/10.1016/j.jhydrol.2012.02.045>
- Yamazaki, D., de Almeida, G. A. M., & Bates, P. D. (2013). Improving computational efficiency in global river models by implementing the local inertial flow equation and a vector-based river network map. *Water Resources Research*, 49(11), 7221–7235. <https://doi.org/10.1002/wrcr.20552>
- Yamazaki, D., Sato, T., Kanae, S., Hirabayashi, Y., & Bates, P. D. (2014). Regional flood dynamics in a bifurcating mega delta simulated in a global river model. *Geophysical Research Letters*, 41(9), 3127–3135. <https://doi.org/10.1002/2014GL059744>
- Yamazaki, D., Trigg, M. A., & Ikeshima, D. (2015). Development of a global ~90m water body map using multi-temporal Landsat images. *Remote Sensing of Environment*, 171, 337–351. <https://doi.org/10.1016/j.rse.2015.10.014>
- Yamazaki, D., Ikeshima, D., Tawatari, R., Yamaguchi, T., O'Loughlin, F., Neal, J. C., et al. (2017). A high accuracy map of global terrain elevations. *Geophysical Research Letters*. <https://doi.org/10.1002/2017GL072874>

- Yamazaki, D., Ikeshima, D., Sosa, J., Bates, P. D., Allen, G., & Pavelsky, T. (2019). MERIT Hydro: A high-resolution global hydrography map based on latest topography datasets. *Water Resources Research*, 2019WR024873. <https://doi.org/10.1029/2019WR024873>
- Yang, G., Guo, S., Liu, P., Li, L., & Liu, Z. (2017). Multiobjective cascade reservoir operation rules and uncertainty analysis based on PA-DDS algorithm. *Journal of Water Resources Planning and Management*, 143(7), 1–13. [https://doi.org/10.1061/\(ASCE\)WR.1943-5452.0000773](https://doi.org/10.1061/(ASCE)WR.1943-5452.0000773)
- Yang, S. L., Milliman, J. D., Li, P., & Xu, K. (2011). 50,000 dams later: Erosion of the Yangtze River and its delta. *Global and Planetary Change*, 75(1–2), 14–20. <https://doi.org/10.1016/j.gloplacha.2010.09.006>
- Yeh, P. J.-F., Swenson, S. C., Famiglietti, J. S., & Rodell, M. (2006). Remote sensing of groundwater storage changes in Illinois using the Gravity Recovery and Climate Experiment (GRACE). *Water Resources Research*, 42(12). <https://doi.org/10.1029/2006WR005374>
- Zajac, Z., Revilla-Romero, B., Salamon, P., Burek, P., Hirpa, F., & Beck, H. (2017). The impact of lake and reservoir parameterization on global streamflow simulation. *Journal of Hydrology*, 548, 552–568. <https://doi.org/10.1016/j.jhydrol.2017.03.022>
- Zarfl, C., Lumsdon, A. E., Berlekamp, J., Tydecks, L., & Tockner, K. (2015). A global boom in hydropower dam construction. *Aquatic Sciences*, 77(1), 161–170. <https://doi.org/10.1007/s00027-014-0377-0>
- Zhao, F., Veldkamp, T. I. E., Frieler, K., Schewe, J., Ostberg, S., Willner, S., et al. (2017). The critical role of the routing scheme in simulating peak river discharge in global hydrological models. *Environmental Research Letters*, 12(7), 075003. <https://doi.org/10.1088/1748-9326/aa7250>
- Zhao, G., Gao, H., Naz, B. S., Kao, S. C., & Voisin, N. (2016). Integrating a reservoir regulation scheme into a spatially distributed hydrological model. *Advances in Water Resources*, 98, 16–31. <https://doi.org/10.1016/j.advwatres.2016.10.014>
- Zhao, T., Richards, K. S., Xu, H., & Meng, H. (2012). Interactions between dam-regulated river flow and riparian groundwater: A case study from the Yellow River, China. *Hydrological Processes*, 26(10), 1552–1560. <https://doi.org/10.1002/hyp.8260>
- Zhou, T., Nijssen, B., Gao, H., & Lettenmaier, D. P. (2016). The Contribution of Reservoirs to Global Land Surface Water Storage Variations. *Journal of Hydrometeorology*, 17(1), 309–325. <https://doi.org/10.1175/JHM-D-15-0002.1>
- Zhou, Y., Hejazi, M., Smith, S., Edmonds, J., Li, H., Clarke, L., et al. (2015). A comprehensive view of global potential for hydro-generated electricity. *Energy & Environmental Science*, 8(9), 2622–2633. <https://doi.org/10.1039/C5EE00888C>